Piezoresistive polymer composites for cantilever readout

Lillemose, Michael

Publication date:
2008

Document Version
Publisher's PDF, also known as Version of record

Piezoresistive polymer composites for cantilever readout

Michael Lillemose[1]

May 31st, 2008

[1]DTU Nanotech - Department of Micro and Nanotechnology, Technical University of Denmark, Building 345E, 2800 Kgs. Lyngby, Denmark.

Preface

This thesis has been written as a part of the requirements for obtaining the PhD degree at the Technical University of Denmark (DTU). The PhD was carried out at DTU Nanotech in the period from the 1st of March 2005 to the 31st of May 2008.

The PhD project has been a part of the Nanoprobes group in the Nanoscience Engineering (NSE) division and was supervised by:

Professor Anja Boisen

The work has been a part of a project called "Novel Functional Polymer Material for MEMS and NEMS Applications" (NOVOPOLY), funded under the European Union (EU) sixth framework programme priority (nanotechnology, materials and production). The project has involved collaboration between six European partners from both universities and industry. The goal of NOVOPOLY has been to develop new functional polymer materials for applications in the fields of micro- and nano-systems technology. Our task has been to investigate piezoresistive polymer composite materials for cantilever sensor readout.

Many people have contributed to this project. First of all, I would like to thank my supervisor Anja Boisen. Her positive attitude and engagement, both as a leader and a supervisor, has been very inspiring. I would also like to thank past and present members of the Nanoprobes group. The atmosphere has always been friendly and helpful and it has been a great place to work. A special thanks to my office mate the past 3 years, Stephan Keller. I have really benefitted from his experience and I have enjoyed our discussions on both scientific and non-scientific matters.

I would like to thank Lauge Gammelgaard for his invaluable help with the carbon doped SU-8 composites at the beginning of the project. It gave me a really good start to my PhD. I am grateful to Jacob Richter for letting me borrow his

four-point bending fixture setup and for helping me out whenever I had problems. I would also like to thank Morten B. Arnoldus and Kasper Reck for their help on the setup. I appreciate the help I received from Dirch Hjorth Petersen on the four-probe measurements at CAPRES A/S and Gabriela Blagoi for her help on the FTIR measurements. For the cleanroom fabrication, I am thankful for all the help I have received from the DTU DANCHIP staff.

A number of students have contributed to the work. I would like to thank Nikolaj O. Christiansen and Anders Christensen for the nice job on patterning of polyaniline in the January 2007 3 weeks course at DTU Nanotech. Also a big thanks to research assistant Martin Spieser, for the very good collaboration and for his committed work on the thin gold films.

I would also like to thank all the partners of the NOVOPOLY project for a fruitful collaboration and for the positive atmosphere at our meetings.

Finally, my deepest thanks to Karla and Sanne. Throughout the project, you have always been there with support and encouragement.

Abstract

Microcantilever based biochemical sensors can be used for detection of surface stress changes, due to the adsorption of specific molecules on one side of the cantilever. The method is fast and label-free and due to the small dimensions, it opens the possibility of fabricating point-of-care measurement devices.
Surface stress changes of a cantilever sensor can be detected by an integrated piezoresistive readout. The goal of this PhD thesis is to increase the sensitivity of polymer based cantilever sensors, by investigating new strain sensitive (piezoresistive) polymer materials, that can improve the piezoresistive readout.
A two- and four-probe electrode chip, for measuring the strain sensitivity of the materials, have been designed and fabricated with standard cleanroom technology. A thin film layer of polymer material is structured on the chips and by insertion in a four-point bending fixture, the deposited thin film can be strained, while measuring how the resistance changes. This allows the determination of the strain sensitivity of the materials.
Three qualitatively different material types have been investigated: conductive polymer composites, an intrinsically conductive polymer and thin gold films.
Conducting polymer composites consisting of SU-8 (an epoxy based photoresist) and different concentrations of carbon- and silver nanoparticles have been investigated. For the carbon nanoparticle doped SU-8 composites, a positive piezoresistive effect was measured, with the largest effect towards the lower concentrations. No significant piezoresistive effect was observed for the silver nanoparticle doped composites.
Thin film structures of the intrinsically conductive polymer, polyaniline, have been fabricated and a negative piezoresistive effect was observed.
Thin gold films were investigated, with the aim of measuring the piezoresistive effect in discontinuous gold films. Various thin film thicknesses were investigated and the piezoresistive effect was found to be close to the value of bulk gold.

Table of Contents

List of Figures

List of Tables

Chapter 1

Introduction

The adsorption of molecules on a clean surface is known to produce surface stress changes [1]. This phenomenon can be used to develop sensitive biochemical sensors, where molecules adsorbed on one side of a micron sized cantilever will generate a surface stress, causing the cantilever to bend.

1.1 Atomic force microscopy

Cantilever sensors originates from the atomic force microscope (AFM) developed by G. Binnig et al. [2]. When a micron sized cantilever with a sharp tip is scanned across a surface, the cantilever will bend because of the interaction (mechanical contact, electrostatic forces, van der Waals interaction, chemical bonding) between the tip and the surface. The deflection can be detected optically by reflecting a laser beam on the topside of the cantilever and collecting it with a photodiode (see figure 1.1). The position of the reflected laser beam will change according to the topography of the sample, hence by scanning the cantilever tip over the surface area one can get a 3D topographic image of the sample surface.
Besides optical detection, the bending of a cantilever has also been detected by piezoresistive [3], piezoelectric [4] and capacitive [5] methods.

1.2 Cantilever sensors

A cantilever sensor is basically an AFM cantilever where the tip has been removed. When molecules bind to the surface of one side of a cantilever, it will induce a change in the surface stress, $\Delta\sigma_s$, due to electrostatic, steric (entropic) and hydrophobic interactions [7, 8]. The relative contributions of the different

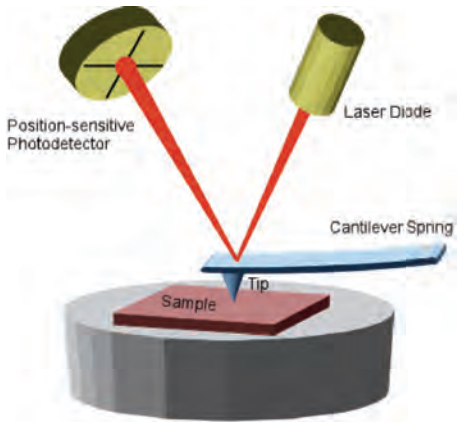

Figure 1.1: Schematics of an AFM. Illustration from [6].

terms will depend on the investigated system.
Due to the unequal interfacial energies on each side of the cantilever, a differential stress is induced, which makes the cantilever bend. This is the basic mechanism behind cantilever sensors (see figure 1.2).
It is important to stress that the cantilever is *not* bending due to the mass of the adsorbed molecules. The gravitational forces from the extra added mass are negligible compared to forces induced by the surface stress change.
If one wants to detect molecule "A", one coats one side of the cantilever with a selective layer that will only bind molecule "A", hence in this way cantilever sensors are label-free detectors [9]. Furthermore, cantilever sensors can be made fast and compact, which opens up for portable devices for point-of-care analysis.
Cantilever sensors have been used for detection of for example DNA [7], proteins [10], pesticides [11] and explosives [12].

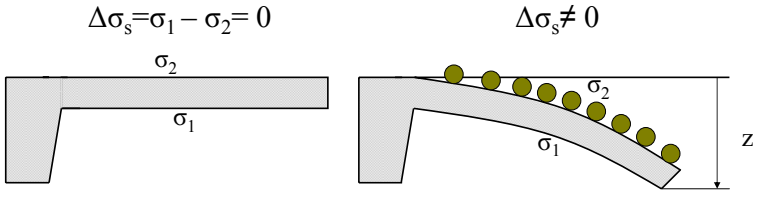

Figure 1.2: Cantilever sensing principle. When molecules are adsorbed on one side of a micron sized cantilever, a change in the surface stress $\Delta\sigma_s$ is induced, which makes the cantilever bend.

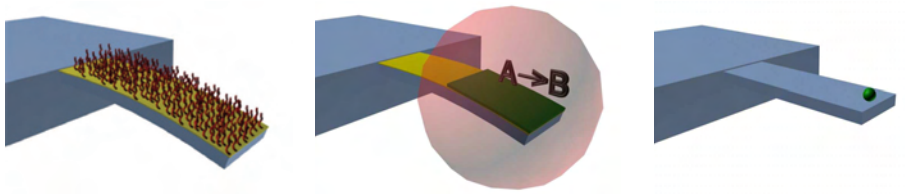

Figure 1.3: The three different modes of detection for a cantilever sensor. Illustration from [15].

1.2.1 Detection modes

A cantilever sensor can be operated in three different modes of detection, shown schematically in figure 1.3:
(A): A biochemical reaction on one side of the cantilever can be detected as a static deflection of the cantilever due to a change in the surface stress.
(B): A change in temperature can be detected as a static deflection by using a cantilever with a sandwich of materials with a difference in the coefficients of thermal expansion [13].
(C): Mass changes can be detected as a change of the resonance frequency, when the cantilever is operated in dynamic (vibrating) mode. With this method a mass resolution of less than an attogram (10^{-18} g) has been achieved [14]. Cantilevers in dynamic mode are most often operated in air and vacuum, since liquids will have a damping effect on the vibrating cantilever.
The first two modes are thus called “static” modes and the last is called “dynamic” mode.

1.2.2 Readout methods

For static mode, the bending of the cantilever is most often detected either with optical or piezoresistive readout. For dynamic mode, both optical [16], capacitive [17] and hard-contact readout [18] have been reported.
Since this report concerns polymer cantilevers operated in static mode, only the optical and piezoresistive readout will be compared.

Optical readout

Optical readout is a very sensitive and well established technique known from the AFM, however it has some drawbacks in terms of cantilever sensors:
(a): You need an optical setup and the laser beam has to be aligned with respect to

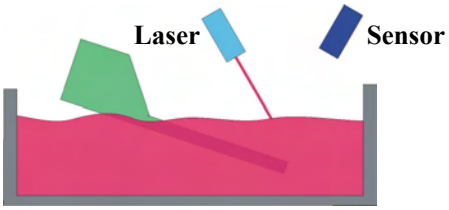

Figure 1.4: Cantilever sensor in a non-transparent liquid.

the cantilever. For an array of cantilevers this gets time consuming, since several laser needs to be aligned.
(b): When operated in a liquid environment, the laser beam has to be re-aligned every time the optical properties of the liquid is changed. Introducing an analyte might change the refractive index of the liquid, which could change the reflected light.
(c): When operated in non-transparent liquids (like blood) it is not possible to obtain a signal (see figure 1.4).
(d): Since the readout mechanism involves an optical system it is difficult to make it compact.

Piezoresistive readout

Piezoresistive materials are materials that change their electrical resistance, when subjected to a mechanical strain. If a piezoresistive material is integrated in the cantilever, a bending of the cantilever can be detected as a change in electrical resistance of the piezoresistive layer, see figure 1.5.
The piezoresistive readout has some advantages to the optical readout:
(a): There are no optics and alignment involved, since the readout signal is a simple electrical signal. This also makes it easy to scale up the cantilever sensor system and do measurements on a whole array of cantilevers.
(b): Operation in liquid is not a problem, since the properties of the liquid has no

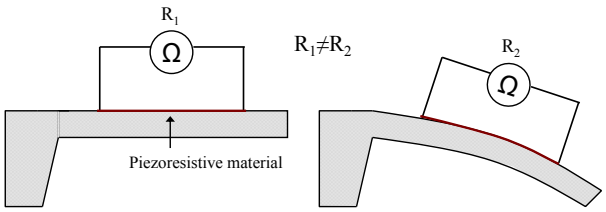

Figure 1.5: Schematics of piezoresistive readout.

influence on the electric properties of the integrated piezoresistor.
(c): As the piezoresistive readout mechanism is integrated *in* the cantilever, the whole sensor system can be made very compact.

1.3 Motivation

The goal of this PhD thesis is to improve the piezoresistive readout of cantilever based sensors.
Cantilever sensors with piezoresistive readout have been fabricated both in silicon [19, 20] and polymer based materials [21, 22]. Silicon based processing is a very well established fabrication technology, however compared to polymer based processing it is rather slow and thus more expensive.
The perfect material for the piezoresistive readout should be very soft (easy to bend) and very strain sensitive/piezoresistive (large resistance change when bent). Silicon is very strain sensitive, but at the same time it is a very hard material with a large Young's modulus. Polymers are much softer than silicon, hence depending on the strain sensitivity of the polymer material, polymer based cantilevers could be more sensitive than silicon cantilever sensors.
The aim of this PhD thesis is to look for new piezoresistive polymer based materials. Polymers can be made piezoresistive, when they are doped with electrically conducting filler particles. The piezoresistive effect of carbon nanoparticle doped polymer composites has been proven for macrosized structures [23–26]. Here the piezoresistive effect is investigated for micron sized thin films, with the aim of integrating them in a microcantilever for piezoresistive readout.
Piezoresistive composites are fabricated through doping of the polymer SU-8 with conductive nanoparticles. The strain sensitivity of the composites is tested using a specially designed microchip fabricated at the DTU Danchip cleanroom facility. The goal is to have polymer cantilevers with piezoresistive readout, that are more sensitive than silicon based cantilevers.
In this report, a good piezoresistive material is defined as one that is easy processable and has a high strain sensitivity. This work has focussed on optimizing the strain sensitivity and *not* the resolution. The resolution of a piezoresistive material is determined by the signal-to-noise ratio.

1.4 Outline

The outline of the thesis is as follows:

- Chapter two introduces some basic cantilever theory in the special case of

a cantilever subjected to a pure surface stress. Piezoresistivity and noise sources of a conductive material is described.

- In chapter three the conductive and piezoresistive behavior of conductive filled polymer composites is presented.
- Chapter four describes the design of a two- and four-probe chip, which together with a specially designed measurement setup can be used to determine the strain sensitivity of materials.
- Carbon nanoparticle composites are described in chapter five. Carbon nanoparticle doped SU-8 polymer composites of different concentrations are fabricated and characterized with respect to their electrical resistivity and strain sensitivity.
- Chapter six describes the fabrication and characterization of silver nanoparticle filled SU-8 polymer composites.
- In chapter seven the intrinsically conductive polymer polyaniline is investigated. It is described how polyaniline thin film can be structured and the fabricated thin films are characterized with respect to their electrical resistivity and strain sensitivity.
- Chapter eight describes how discontinuous metal films can be fabricated. The resistivity and strain sensitivity of gold films of various thicknesses is measured.
- Chapter nine concludes the thesis, stating the most important achievements and results.

Chapter 2

Theory

This chapter introduces the basic theory behind cantilevers with integrated piezoresistive readout.
The sensitivity of a cantilever will depend on the strain sensitivity of the integrated piezoresistor, expressed by the so-called gauge factor, K, hence it is described how conductive materials change their electrical resistance, when subjected to a mechanical strain.
Next, it is described how a cantilever with integrated piezoresistive readout can be used for detecting a surface stress generated by molecular interactions at the cantilever surface. The theory has been developed by O. Hansen [27].
Finally, two internal noise sources in resistive materials are briefly described.

2.1 Piezoresistivity

The resistance, R, of a conductive material is given by

$$R = \frac{\rho l}{wt}, \tag{2.1}$$

where ρ is the resistivity, l is the length, w is the width and t is the thickness, see figure 2.1.

A material is piezoresistive if it changes its electrical resistivity, when it is subjected to a mechanical strain. Most materials change both cross section and length, when they are strained and this will give rise to a change in the resistance. Piezoresistive materials have a resistance change that cannot solely be explained by the geometrical effects.
For an isotropic material subjected to a strain, the change in resistance is found

from equation 2.1

$$dR = \frac{\partial R}{\partial \rho}d\rho + \frac{\partial R}{\partial l}dl + \frac{\partial R}{\partial w}dw + \frac{\partial R}{\partial t}dt \tag{2.2}$$

$$= \frac{l}{wt}d\rho + \frac{\rho}{wt}dl - \frac{\rho l}{w^2 t}dw - \frac{\rho l}{wt^2}dt\,, \tag{2.3}$$

hence the fractional change in resistance is given by

$$\frac{dR}{R} = \frac{d\rho}{\rho} + \frac{dl}{l} - \frac{dw}{w} - \frac{dt}{t}\,. \tag{2.4}$$

From the theory of elasticity one have for an isotropic elastic material subjected to a uniaxial stress, ρ_x, along the length axis

$$\frac{dl}{l} = \epsilon_x,\ \frac{dw}{w} = \frac{dt}{t} = -\nu\epsilon_x\,, \tag{2.5}$$

where ϵ_x is the strain and ν is the Poisson ratio [28]. A measure of the strain sensitivity is given by the gauge factor, K, defined as

$$K = \frac{1}{\epsilon_x}\frac{dR}{R}\,. \tag{2.6}$$

By using equation 2.4 and 2.5 one gets an expression for the gauge factor

$$K = K_{\text{geo}} + K_{\text{piezo}} = (1 + 2\nu) + \frac{1}{\epsilon_x}\frac{d\rho}{\rho}\,. \tag{2.7}$$

Equation 2.7 expresses, that the gauge factor of a conductive material is a sum of two contributions. When a piezoresistive material is strained, the change in the resistance thus originates from two qualitatively different terms. K_{geo} is a purely geometrical term, which depends on the elastic properties of the material and this term exists for all conductive materials. K_{piezo} is the "piezoresistive" term. It is

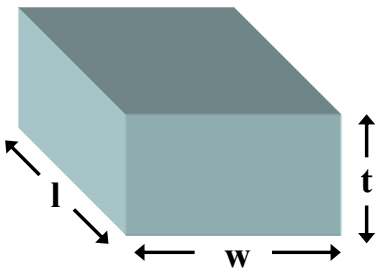

Figure 2.1: A resistor R with the dimensions $l \times w \times t$.

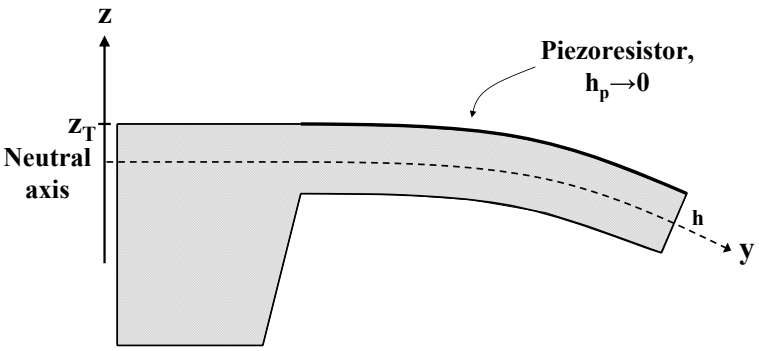

Figure 2.2: Schematics of a simple cantilever consisting of one layer with height h and an infinitely thin piezoresistor of height $h_p \rightarrow 0$ placed at the top.

a physical term stating, that for some materials the resistivity will change, when they are subjected to a mechanical strain.
When single crystalline silicon is strained, the band structure and thus the charge mobility is changed and this is the origin of the piezoresistive effect in silicon [29, 30]. The magnitude of the piezoresistive effect is highly anisotropic and will depend on the specific crystal direction. For semiconductors, such as crystalline silicon, $K_{\text{piezo}} \approx 50 K_{\text{geo}}$ [30].
In the next chapter, the piezoresistive effect in conductive particle doped polymer composites will be explained.

2.2 Piezoresistive cantilever subjected to a pure surface stress

When molecules bind to the surface of a cantilever, the molecular interactions will induce a surface stress, σ_s, causing the cantilever to bend. The bending can be divided in a stretching/compression part, ε_0, which is constant throughout the cantilever and a pure bending part, βz. β is a constant and z is the distance to the neutral axis, which is defined as the position in the cantilever, which is stress-free, when the cantilever is bent (see figure 2.2).
The strain can thus be expressed as a superposition of the two contributions:

$$\varepsilon(z) = \varepsilon_0 + \beta z \,. \tag{2.8}$$

For a multilayered cantilever consisting of i layers of thickness h_i, with built-in stress σ_i and Young's modulus E_i, the uniaxial stress can be expressed as

$$\sigma(z) = \sigma_i + E_i \varepsilon(z) = \sigma_i + E_i \varepsilon_0 + \beta E_i z \,. \tag{2.9}$$

A cantilever experiencing a static stress, requires that the total force, F, and the total moment, M, acting on the neutral axis equals zero. This can be expressed as [31]

$$F = \int_{z_B}^{z_T} \sigma(z) dz = 0 \tag{2.10}$$

and

$$M = \int_{z_B}^{z_T} z\sigma(z) dz = 0\,, \tag{2.11}$$

where z_T and z_B is the position of the top and bottom surface of the cantilever with respect to the neutral axis.
One can now find the strain $\varepsilon(z)$, as a function of the distance to the neutral axis, in a cantilever with i layers of height h_i and Young's modulus E_i, by solving equation 2.10 and 2.11 with respect to equation 2.9.
For a piezoresistive material subjected to a strain ε, the relative change in resistance is defined as

$$\frac{\Delta R}{R} = K\varepsilon\,, \tag{2.12}$$

where K is the gauge factor.
By inserting the derived expression for $\varepsilon(z)$ in equation 2.12, one can find an expression for the relative change in resistance in a multilayered cantilever with a piezoresistive layer, subjected to a surface stress. The expression can be simplified by neglecting any built-in stresses and assuming that the surface stress is only applied on the top-side of the cantilever [32]

$$\frac{\Delta R}{R} = K\Bigg(- \frac{1}{\sum_i E_i h_i} + \frac{z_T(z_T - \sum_{j=0}^{p} h_j + \frac{h_p}{2})}{\sum_i E_i h_i((z_T - \sum_{j=0}^{i} h_j + \frac{h_i}{2})^2 + \frac{1}{3}(\frac{h_i}{2})^2)}\Bigg)\sigma_s\,. \tag{2.13}$$

Expression 2.13 describes the relative change in resistance of the piezoresistive layer, when a cantilever is subjected to a surface stress. The index p describes the position of the piezoresistive layer in the cantilever. The sum $\sum_{j=0}^{p} h_j$ describes the distance from the top of the cantilever to the bottom of the piezoresistive layer. The sum $\sum_{j=0}^{i} h_j$ describes the distance from the top of the cantilever to the bottom of the i'th layer.
Expression 2.13 is rather complicated, but it can be simplified if one instead of a multilayered cantilever, considers a simple cantilever with a single layer of height h and Young's modulus E and an infinitely thin piezoresistive layer (height, $h_p \rightarrow 0$) placed at the top surface of the cantilever. Expression 2.13 can then be reduced to

$$\frac{\Delta R}{R} = -K\Big(\frac{1}{Eh} + \frac{3}{Eh}\Big)\sigma_s = -K\Big(\frac{4}{Eh}\Big)\sigma_s\,, \tag{2.14}$$

since $z_T = h/2$, $\sum_{j=0}^{p} h_j = h_p \to 0$ and $\sum_{j=0}^{i} h_j = h + h_p \to h$.
Disregarding the noise contribution one can see from equation 2.14 that the surface sensitivity of a cantilever with an integrated piezoresistor is determined by the ratio K/E. In other words, to maximize the signal from a piezoresistive cantilever you need a soft cantilever material and a piezoresistor with a high gauge factor.
Depending on the doping level and grain size, silicon has a gauge factor of 20-170 [32]. Assuming a Young's modulus of $E_{\mathrm{Si}} = 150$ GPa gives a maximum of $(K/E)|_{\mathrm{Si}} \approx 150/150\ \mathrm{GPa} = 1\ \mathrm{GPa}^{-1}$.
This thesis investigates cantilevers fabricated in the polymer SU-8, which has a Young's modulus of $4 - 5$ GPa [33]. It means, that if one can find a piezoresistive polymer material with $K \geq 4 - 5$ one can in principle fabricate an all-polymer cantilever sensor that is more sensitive than a silicon cantilever of the same dimensions.

2.3 Noise sources

The minimum obtainable surface stress resolution of a cantilever with piezoresistive readout is governed by the noise sources acting on the cantilever. External noise sources such as vibrations from the surroundings are neglected. In this section only the internal noise sources affecting the cantilever performance will be introduced.

2.3.1 Johnson noise

Johnson noise is caused by thermal motion of the charge carriers. For a resistor with resistance R the Johnson voltage noise is given by

$$V_J = \sqrt{4k_B T R \Delta f}\,, \tag{2.15}$$

where k_B is Boltzman's constant, T is the temperature and Δf is the measured bandwidth. For a constant temperature the Johnson noise can thus be minimized by lowering the resistance in the design.

2.3.2 $1/f$ noise

$1/f$ noise is a frequency dependent noise source, which has been described by Hooge *et al.* [34]. The $1/f$ noise voltage spectral density, $S_{1/f}$, is given by

$$S_{1/f} = \frac{\alpha V^2}{Nf}\,, \tag{2.16}$$

where α is a materials constant, V is the voltage, f is the frequency and N is the number of charge carriers in the resistor.
$1/f$ noise is the dominating noise source in percolative systems and is diverging when moving towards the metal-insulator transition [35, 36].

2.4 Summary

Piezoresistive materials change their electrical resistance, when they are strained. A measure of how much the resistance changes for a certain applied strain is expressed in the strain sensitivity factor or gauge factor, K.
The sensitivity of a cantilever with piezoresistive readout subjected to a pure surface stress is proportional to the ratio K/E, where K is the gauge factor of the piezoresistor and E is Young's modulus of the material. For an SU-8 polymer based cantilever to be more sensitive than a silicon cantilever a gauge factor of $K \geq 4 - 5$ is needed.

Chapter 3

Conductive polymer composites

Conductive polymer composites is a class of materials that consists of a polymer and an electrically conductive filler material such as metal nanoparticles, carbon nanotubes, carbon nanoparticles etc. [37]. This chapter describes the conductive and piezoresistive behavior of conductor filled polymer composites. Emphasis will be on carbon nanoparticle (also known as carbon black) filled polymer composites, since it has been the main focus of this work. The chapter will not go into detail with the theory behind the conductivity, but will provide more qualitative explanations of the conductive phenomena in polymer composites.

3.1 Conductivity

Consider a 3D cubic lattice with N lattice sites, where $N \to \infty$. If we now start to remove bonds between lattice sites and let p denote the fraction of bonds remaining (p=1, all bonds remaining, p=0 all bonds removed), there will be a certain critical fraction, p_c, at which the lattice is no longer infinitely connected. By applying a voltage across a finite sized lattice and assigning a conductance to each bond, numerical simulations have shown that the conductance G increases with a power law dependence:

$$G(p) \propto (p - p_c)^t \,. \tag{3.1}$$

This is an example of a classical percolation system that exhibits a critical threshold [38].

When adding conductive filler particles to an electrically insulating polymer matrix, a conductive network will start to form. As more and more filler particles are added, the system will undergo a transition from insulator to conductor. The filler concentration at which an infinitely connected path exists for the first time is called the critical concentration or *percolation threshold* υ_c, see figure 3.1. The

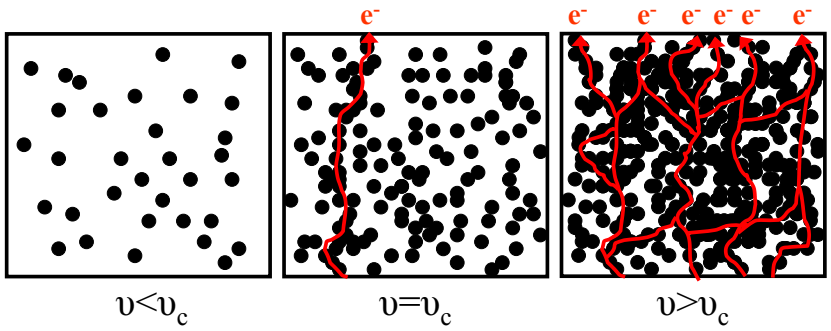

Figure 3.1: From left to right is shown a schematics of conductive filled composites below, at and above the percolation threshold υ_c. *Below* the percolation threshold there are no conductive paths through the composite. *At* the percolation threshold there is just one conductive path and *above* there are numerous paths for electron conduction through the sample.

composite resembles a percolative system however, the basic assumption of classical percolation theory is a geometrically connected network. This is not the case for carbon loaded polymer composites, where it has been shown that the dominating contribution to the conduction mechanism is electron tunneling between adjacent carbon particles through the polymer film separating them [39]. However, due to the exponentially decreasing tunneling decay distance one can discard non-nearest neighbor contributions to the conductivity, hence we have an effectively connected network that behaves like a percolation system [40]. The conductivity of a filler loaded composite can thus be described by

$$\sigma \propto (\upsilon - \upsilon_c)^t \,, \tag{3.2}$$

where υ is the filler concentration, υ_c is the filler concentration at the percolation threshold and t is the conductivity exponent. The percolative behavior is illustrated in figure 3.2.

The main mechanism of conduction in filler loaded composites is electron tunneling between adjacent particles. The tunnel current and thus the conductivity of the composite will depend on the potential barrier height between adjacent particles and the interparticle distance. These two parameters need to be known in order to theoretically describe the conductivity through equation 3.2.

The potential barrier height can be found as the difference in the polymer and filler particle work functions. For the interparticle distance one have to assume some idealized distribution function [42]. Such a distribution function will always be an approximation, since the real three dimensional structure of the composites in general is extremely complex and will depend strongly on internal variables such as the structure of the carbon black being used [43], the preparation method of the

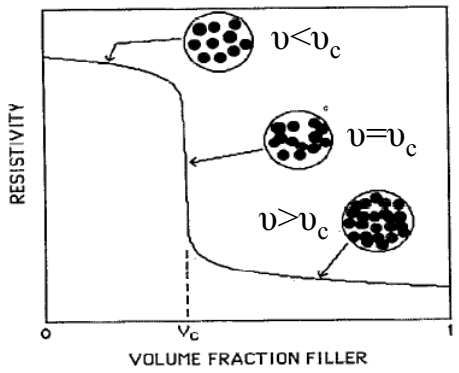

Figure 3.2: Resistivity as a function of the filler concentration for a percolative system. Illustration is reproduced from [41].

composite [23], filler-filler interactions [23] and filler-matrix interactions [44]. As it turns out there has been a large discrepancy between theoretically predicted and experimentally determined values for v_c and t. Depending on the theoretical approach, values for the critical exponent t has both been under- and overestimated compared to the measured values [40].
By dividing the carbon blacks in two classes, "low structure" and "high structure", the trends in the measured values for the percolation thresholds and conductivity exponents can be qualitatively explained. "Low structure" carbon blacks are spherical particles that form a closed-packed network with little aggregate formation, see figure 3.3 (left). This gives rise to *high* values for both v_c and t. On the other hand, "high structure" carbon blacks form highly aggregated structures that lead to *low* values for v_c and t, see figure 3.3 (right) [45].

The existence of a complicated conductive network in carbon black filled composites has been demonstrated by Carmona et al. [46–48]. They scanned the surface of a carbon black doped polymer composite using conductive atomic force microscopy (C-AFM) and showed that penetrating conductive paths exist above the percolation threshold and vanish below. Similar experiments have been carried out by Viswanathan et al. by use of electrostatic force microscopy [49].
To summarize, carbon black loaded composites are characterized by having a critical filler concentration at which the conductivity increases with a power law dependence. The percolation threshold and the exact power law dependence are difficult to predict theoretically, since they reflect the microstructure of the composite, which in general is very complicated.

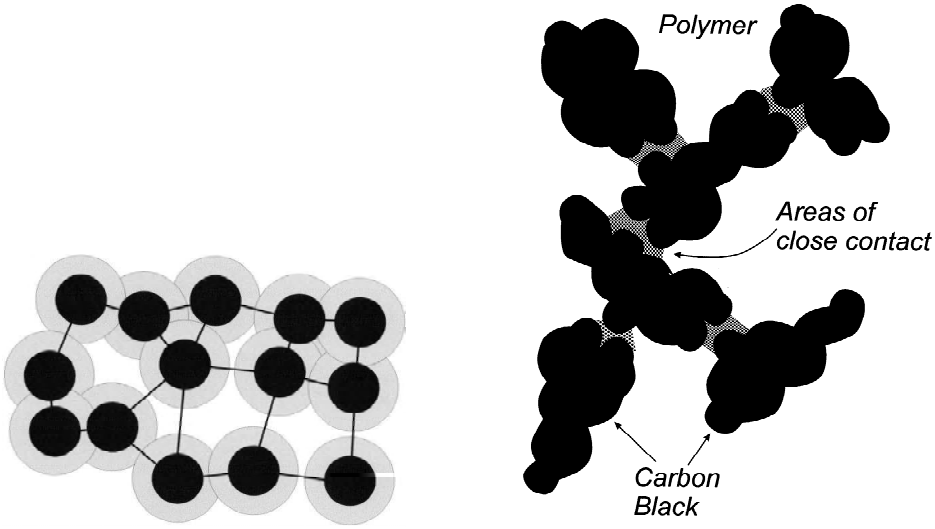

Figure 3.3: Illustration of the two types of carbon black. LEFT: Low structure carbon black has spherical particles with no aggregates. The black circles show the particles and the grey rings show the effective tunneling distance. Low structure carbon black gives high values for υ_c and t. RIGHT: High structure carbon black has a highly aggregated structure. High structure carbon blacks give low values for υ_c and t. Illustrations from [45].

3.2 Piezoresistivity

Besides the internal variables mentioned in the previous section, external variables such as temperature and mechanical stress can affect the conductivity of filler loaded composites. Applying a mechanical stress to a conductive filler loaded composite will change the interparticle distance, which effectively corresponds to a change of the filler concentration and this will change the conductivity of the composite according to equation 3.2.
For the strain sensitivity of the composites one can write the gauge factor K as a sum of three terms

$$K = K_{\text{int}} + K_{\text{geo}} + K_{\text{piezo}} \,, \tag{3.3}$$

where K_{int} is the intrinsic piezoresistive contribution from the conductive filler particles of the composite, K_{geo} is the geometrical contribution and K_{piezo} is the piezoresistive contribution.
For K_{piezo} to be nonzero, there has to be a difference in the elastic constants of the filler and polymer matrix [50]. If the elastic constants are equal, the polymer and filler particles will respond equally to an applied strain, hence the interparticle distance will not change, the concentration remains constant and K_{piezo} equals zero. However, if there is a difference in the elastic constants, an applied strain will

change the interparticle distance, which effectively corresponds to a change in the filler concentration. Due to the power law dependence expressed in equation 3.2, slight changes of the filler concentration can have an impact on the conductivity close to the percolation threshold. It means that conductive polymer composites could have a very high strain sensitivity close to the percolation threshold.
For a composite one can write the filler concentration as

$$\upsilon = \frac{V_c}{V_c + V_m} , \tag{3.4}$$

where V_c is the filler particle volume and V_m is the polymer matrix volume. Assuming an isotropic elastic material of volume V subjected to a small uniaxial strain, ϵ, the volume will change as

$$V \rightarrow V + \Delta V = V(1 + (1 - 2\nu)\epsilon) , \tag{3.5}$$

where ν is Poisson's ratio of the specific material, hence the filler concentration will depend on the applied strain, $\upsilon = \upsilon(\epsilon)$. From equation 3.4 and 3.5 one can see that, if the filler particle and polymer matrix have identical Poisson's ratio, an applied strain will not change the concentration.
From equation 3.2 one can find the resistivity

$$\rho \propto (\upsilon - \upsilon_c)^{-t} = (\upsilon(\epsilon) - \upsilon_c)^{-t} . \tag{3.6}$$

The piezoresistive contribution can now be estimated using equation 2.7

$$\frac{d\rho}{\rho} = \frac{1}{\rho}\frac{\partial \rho}{\partial \epsilon} d\epsilon = -t(\upsilon(\epsilon) - \upsilon_c)^{-t-1}\frac{\partial \upsilon}{\partial \epsilon} d\epsilon , \tag{3.7}$$

hence as we move close to the percolation threshold, $\upsilon(\varepsilon) \rightarrow \upsilon_c$, the piezoresistive contribution will diverge. It means that conductive filled polymer composites can be potentially very strain sensitive and have high gauge factors close to the percolation threshold.
Qualitatively one can explain it by realizing, that close to the percolation there are very few conductive paths. Breaking some of the paths by straining the material, will thus result in a large relative change of the resistance. This explains why conductive composite should have maximum strain sensitivity close to the percolation threshold.

3.3 Summary

In this chapter the basic theory for conductive particle filled polymer composites has been introduced. When adding conducting filler particles to an insulating

polymer matrix, the composite will undergo a transition from insulator to conductor. Above a certain critical filler concentration called the percolation threshold, the conductivity will increase with a power law dependence.
It has been explained why such polymer composites are piezoresistive and that the maximum gauge factors should be found close to the percolation threshold.

Chapter 4

Chip design and measurement setup

This chapter describes the layout of a microfabricated chip designed for measuring the resistivity of conductive thin film materials. Two different designs have been made, such that the resistivity can be measured either in two- or four-probe electrode configuration.
A four-point bending fixture setup is presented, where the microfabricated chips are inserted and subjected to a constant stress, while the resistance change of the composite thin films is measured. This allows for the determination of the gauge factors.

4.1 Chip design

For measuring the resistivity of thin film materials both two- and four-probe electrode configurations have been used. Figure 4.1 shows a schematics of the two methods.
The four-probe design is the standard method for measuring resistivities of conductive materials, where a constant current I is forced through the resistor R and the voltage drop V across is measured. A basic assumption of the four-probe method is that the current is constant through the resistor. If $R \ll R_V$, where $R_V \approx 10$ GΩ is the impedance of the voltmeter, the voltmeter draws very little current and the assumption is valid. The assumption is easily fulfilled for low-resistivity materials, however the present work investigates materials with resistivities up to $\rho \sim 10^4$ Ωm, where the requirement can be hard to fulfill, hence a two-probe electrode configuration design was also made.

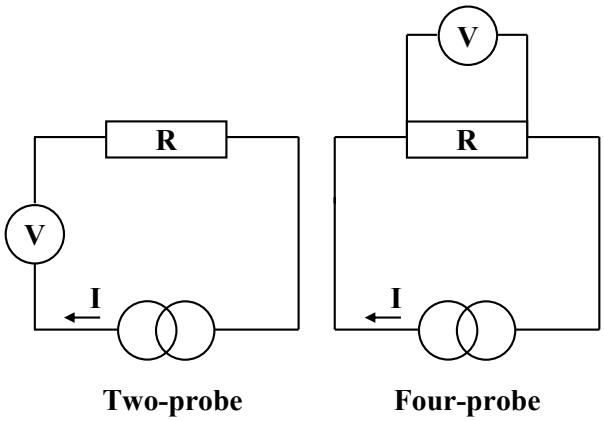

Figure 4.1: LEFT: Two-probe electrode configuration. RIGHT: Four-probe electrode configuration. A constant current I, is forced through a resistor R, and a high impedance voltmeter measures the voltage drop V across.

4.1.1 Two-probe design

Figure 4.2 shows the layout of the two-probe design. The dimensions of the chip are 40×5.3 mm^2. The left and right halves are identical, but they are not electrically connected.

The pink square is the composite thin film material, which is deposited on top of 50 μm wide electrodes that are colored in green. The width of the conductive thin film is $W = 3$ mm and the spacing between the 10 electrodes is designed such that the two-probe resistance R, can be measured for nine different resistor lengths, $L_{1-9} = 5, 10, 15, 20, 25, 50, 100, 200$ and 500 μm. Knowing the thickness t, of the composite thin film, one can calculate the resistivity as $\rho = Rwt/L$. As high-resistivity materials will be investigated, the L/W-ratios of the conductive thin films are very low, such that the size of the measured resistance will be minimized.

The drawback of the two-probe method is that one also measures the resistance of the contacts and the wires. One will either have to estimate the size of the contact resistance or justify that it can be neglected. With the above design, one can estimate the size of the contact resistance by plotting the resistance as a function of the length of the resistor, $R(L)$. The contact resistance can then be estimated as $R(L = 0)$.

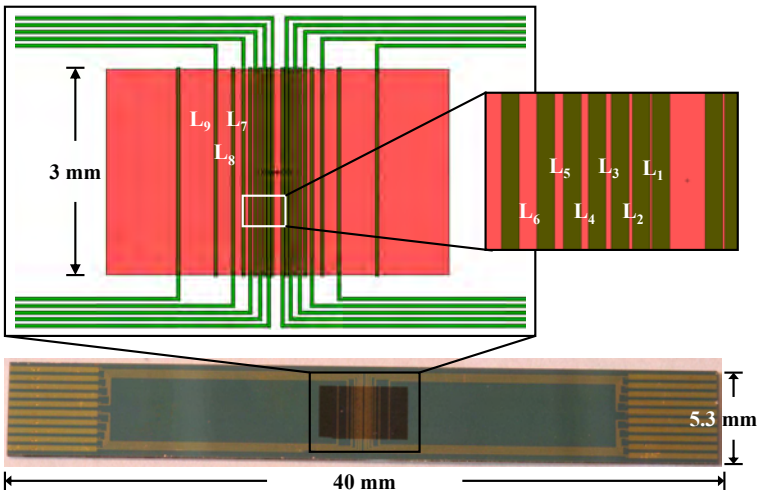

Figure 4.2: The chip design in two-probe configuration seen from above. The dimensions of the chip are 40×5.3 mm^2. The pink square is the conductive thin film material and the green color is 50 μm wide electrodes. The closeups show the electrode configuration. The spacing between the electrodes is L_{1-9} = 5, 10, 15, 20, 25, 50, 100, 200 and 500 μm.

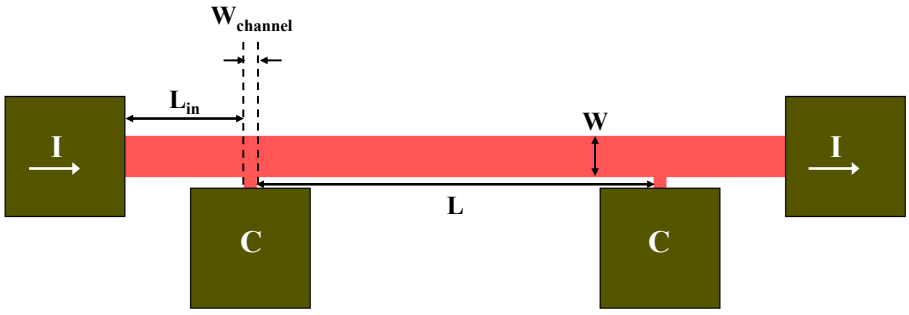

Figure 4.3: Resistor of length L and width W in the for four-probe design. The dark green squares are contact pads, which have been enlarged to insure good electrical connection to the electrodes.

4.1.2 Four-probe design

Figure 4.3 shows a schematic of a resistor of length L and width W in the four-probe configuration. A constant current, I, is forced through the resistor, colored in pink, and the dark green pads show, where the resistor connects to the metallic electrodes.
The potential drop in the resistor is measured with a high impedance voltmeter connected to the points, C. The small piece of wire L_{in} is included in order to secure that the current has obtained a homogeneous flow, when it reaches the resistor. For $L_{\text{in}} > 2W$ one can assume that this condition is fulfilled [51]. In the design $L_{\text{in}} = 3W$ was chosen.
The width of the channels, W_{channel}, connecting the resistor and the electrode pads is chosen as small as possible. Large channel widths will result in a smaller resistance in the actual resistor, because the current will travel in a larger area than expected. By keeping $W_{\text{channel}} \ll W$ this error can be minimized.
The L/W-ratio of the resistor design has been modeled with the COMSOL finite element method (FEM) package in conductive media DC application mode by solving the equation [52]

$$-\nabla \cdot (\sigma \nabla V) = 0 \,, \tag{4.1}$$

where σ is the conductivity and V is the voltage drop. Figure 4.4 (left) shows a model of the resistor in four-probe configuration. For the boundary conditions, a constant current flow is applied on the left hand surface of the resistor. The right hand surface of the resistor and the two channels are kept at $V_0 = 0$. All other surfaces are electrically insulating. High resistivity pads are placed at the end of the channels to simulate the effect of a high impedance voltmeter.
For a given resistor geometry one can define $\Delta V = V - V_0$, where V is the voltage drop in a resistor with channels connected (figure 4.4, left) and V_0 is the voltage drop in an identical resistor, but with *no* channels connected. For different L/W-ratios $\Delta V = V - V_0$, has been calculated. Figure 4.4 (right) shows $\Delta V/V_0$ as a function of L/W. One can see that $\Delta V/V_0 \approx 0$ for $L/W \geq 6$.
Two different designs for the resistor was made and the parameters are summa-

Table 4.1: Four-probe design parameters

	W [μm]	W_{channel} [μm]	Pads [μm^2]
Design 1	50	15	150×150
Design 2	100	25	300×300

rized in table 4.1. In both designs, resistors were made with L/W ratios of either 6, 8, 10, 15, 25, 50 or 100.
Figure 4.5 shows the layout of the complete chip. Three resistors, R1-R3, similar

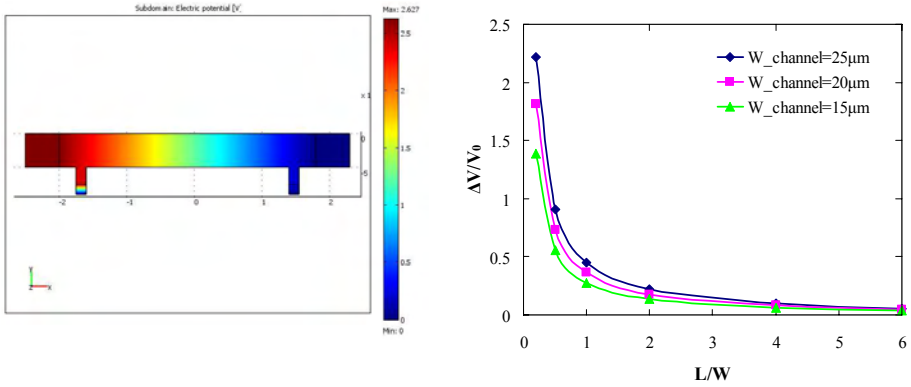

Figure 4.4: LEFT: The resistor design modeled by FEM. A constant current is passed through the resistor and the voltage drop between the two channels is calculated. The figure shows the calculated electric potential. RIGHT: $\Delta V/V_0$ as a function of L/W. For $L/W \geq 6$ $\Delta V/V_0 \approx 0$ and this requirement has been fulfilled in the resistor design.

to the one in figure 4.3 are connected in series on each half of the chip. A constant DC current is passed through electrodes 2-9 and electrode 3-4, 5-6 and 7-8 measures the voltage drop across resistor R1, R2 and R3, respectively. The electrodes are 100 μm wide.

4.2 Measurement setup

Both the two- and four-probe configuration chips are designed to fit in an existing experimental setup developed by PhD Jacob Richter and MSc Morten B. Arnouldus for measuring gauge factors of silicon and strained silicon germanium [53–55].

4.2.1 Four-point bending fixture

To induce a stress in the conductive thin film material, the designed chips can be inserted in a four-point bending fixture shown schematically in figure 4.6. Two inner knives are acting on the chip with the forces $-F/2$ and two outer knives are acting with equally large opposite forces, $F/2$. Between the two inner knives the chip is subjected to a pure bending and the moment is constant with a value of $M = -Fa/2$, where a is the distance between the neighboring inner and outer knives.

The only non-zero stress component is σ_{xx}, hence the stress is uniaxial and varies

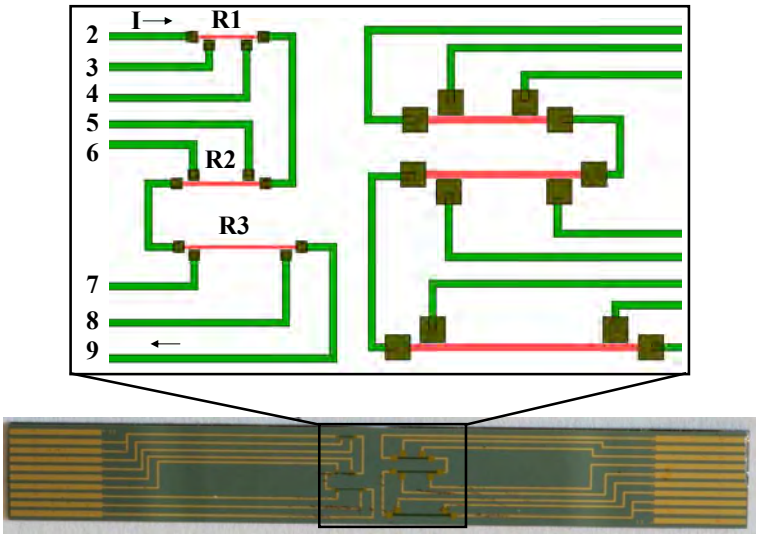

Figure 4.5: The chip design in four-probe configuration. The chip measures 40 × 5.3 mm^2. The close up shows the resistor layout. There are three resistors R1-R3 connected in series on each side of the chip. A current is passed through electrode 2-9 and electrode 3-4, 5-6 and 7-8 measures the voltage drop across R1, R2 and R3, respectively. Electrode 0 is connected to ground and electrode 1-2 are short circuited, hence they are not visible in the inset.

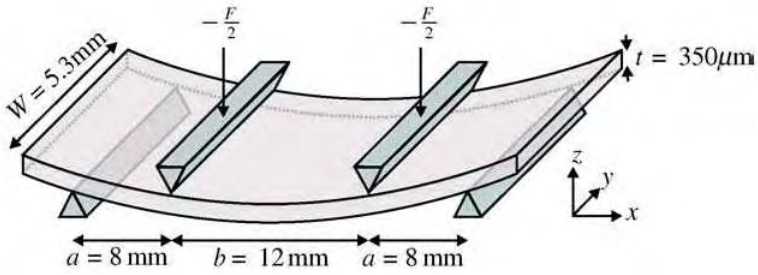

Figure 4.6: Sketch of the four-point bending fixture with a chip inserted. At the surface between the two inner knives the stress is constant and uniaxial. Figure taken from [54].

linearly with z. If $\sigma_{\max}$ denotes the stress at the surface of the chip, one can express σ_{xx} as

$$\sigma_{xx} = -\sigma_{\max}\frac{z}{t/2} = -\sigma_{\max}\frac{2z}{t}\,, \tag{4.2}$$

where t is the thickness of the chip [28]. By using equation 4.2, the moment between the inner knives can be calculated as

$$M = \int_{-t/2}^{t/2}\sigma_{xx}Wzdz = -W\frac{2\sigma_{\max}}{t}\int_{-t/2}^{t/2}z^2dz = -\frac{1}{6}W\sigma_{\max}t^2\,, \tag{4.3}$$

where W is the width of the chip. Equating the two expressions for the moment

$$-\frac{1}{6}W\sigma_{max}t^2 = -\frac{1}{2}Fa\,, \tag{4.4}$$

yields an expression for σ_{max}

$$\sigma_{max} = \frac{3Fa}{Wt^2}\,. \tag{4.5}$$

Expression 4.5 states that the maximum uniaxial stress, $\sigma_{\max}$ at the surface of the chip between the two inner knives of the four-point bending fixture is constant and is determined by the thickness of the chip, t, the width of the chip, W, the force loaded, F, and the distance between the inner and outer knives, a. All of these parameters are known, hence when inserting the chips in the four-point bending fixture, a well-known stress can be applied to the resistive material on the chip. The applied stress is converted to a strain, ε, through Hooke's law, $\sigma_{\max} = \varepsilon_{\max}E$, where E is Young's modulus (of silicon in this case).

For polymer composites the resistive material is spin coated on top of the surface, so in principle the neutral axis of the chip is shifted however, for thin films one can assume that $\sigma_{\text{film}} \approx \sigma_{\max}$.

The four-point bending fixture has been realized in two different versions. In the first version shown in figure 4.7 (left) the chip is clamped between two bricks and a force is exerted by suspending a weight of known mass on the bricks. The stress can be calculated from 4.5 by knowing the loaded mass, m. It is a very simple setup, which does not need a calibration of a force sensor, however, the weights have to be loaded manually, which means that the measurement procedure cannot be automated.

In the second version shown in figure 4.7 (right) the force is exerted by a microstepper pressing the two bricks together. The movement of the microstepper is controlled by an actuator, hence the measurement procedure can be automated. The stress is measured by a calibrated force sensor. Both setup versions also provide temperature control.

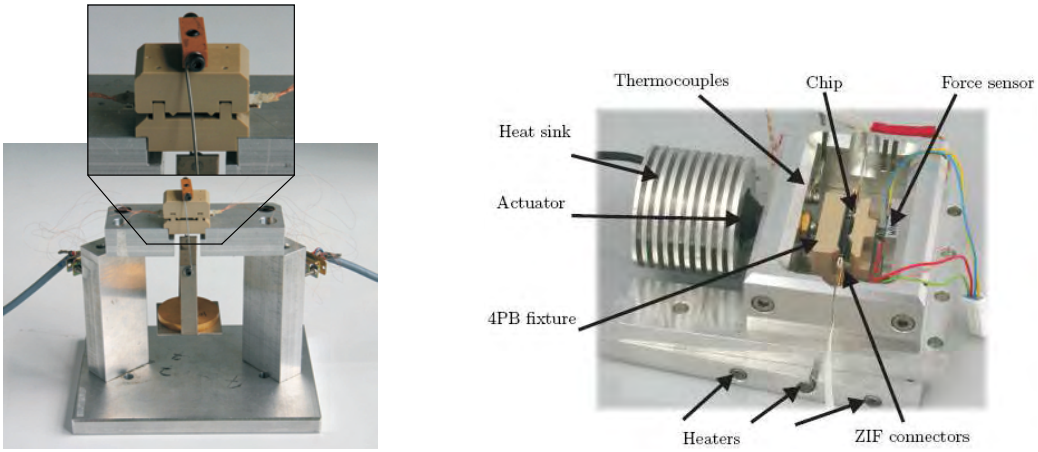

Figure 4.7: LEFT: The chip is inserted between two bricks and a force is exerted by suspending a weight of known mass on the bricks. The inset shows a closeup of the four-point bending fixture. Both inner- and outer knives are visible. Picture taken from [53]. RIGHT: Picture of the four-point bending fixture with the microstepper. Picture from [55].

The stresses exerted by the four-point bending fixture are much larger than the stresses one would expect in a cantilever sensor (4pp~MPa, cantilever ~mN/m), however, the idea is to use the four-point bending fixture for narrowing down the field of promising materials for the piezoresistive readout and then move on to fabricate cantilevers with the selected materials.

4.2.2 Electrical connection

For the electrical connection it is important that it is easy to use and that the bending of the chip is not hindered in any way. These requirements are fulfilled by the Zero Insertion Force (ZIF) chip connection. Figure 4.8 shows the simple plug-and-play connection.
ZIF connectors are normally used to establish electrical connection to a Flat Flex Cable (FFC). By copying the dimensions of a FFC onto the chip, the ZIF can be used for electrical connection.
The weight of the ZIF connector is $W_{ZIF} \approx 0.14$ g, hence the stress contribution originating from the gravitational force of the ZIF connector is negligible compared with stresses from the weight loads suspended on the bricks.
The design requirements can be summarized as follows:

- The end of the chip is designed to fit the ZIF connector, hence it has 10

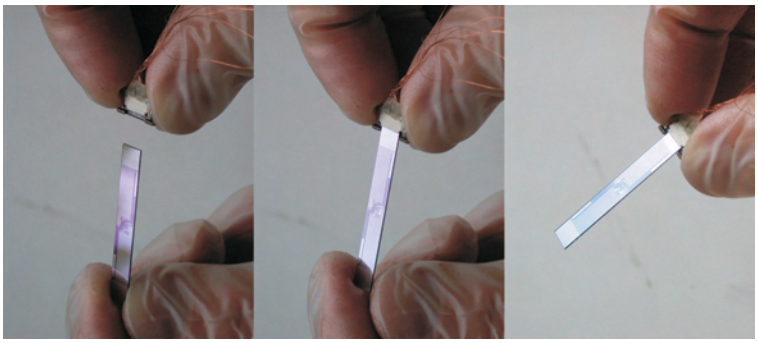

Figure 4.8: From left to right it is shown how the chip is easily connected to ZIF connector. Picture from [53].

electrical connection pads with a width of 0.3 mm and a pitch of 0.2 mm.

- To fit in the ZIF connector, the thickness of the chip must be $t = 350\ \mu$m, hence only double side polished wafers have been used in the fabrication of the chips.
- The width of the chip is fixed to 5.3 mm.

The complete measurement setup is shown schematically in figure 4.9. The chip is connected to a Keithley 2700 Multimeter (and a Keithley 2400 Sourcemeter in the case of four-probe measurements) through the ZIF connector and the FFC. Data is collected with a LabVIEW program.

4.3 Summary

A two- and a four-probe chip design for measuring the resistivity of piezoresistive thin film materials has been presented. The chips are designed such that they fit in an already existing four-point bending fixture setup. Using the setup, a constant stress can be applied to the piezoresistive material, while measuring the change in resistance. This allows the determination of the gauge factors of the piezoresistive materials.

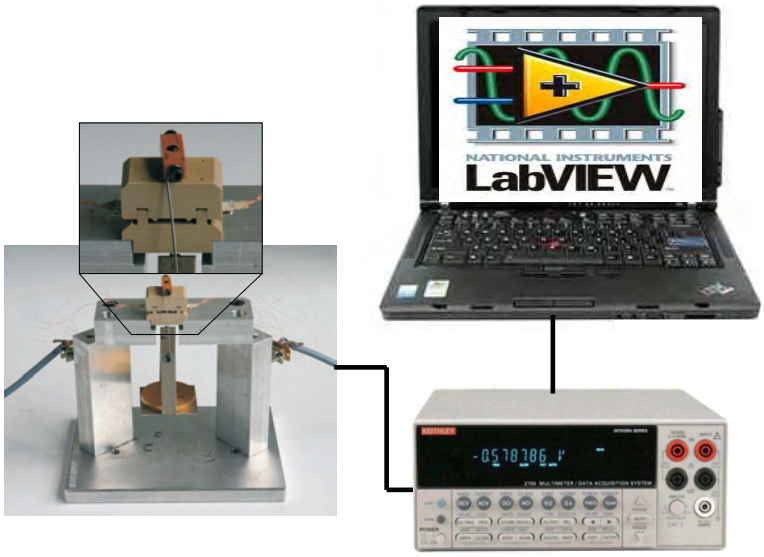

Figure 4.9: Schematics of the measurement setup.

Chapter 5

Carbon black SU-8 composites

This chapter explains how piezoresistive polymer composites have been fabricated by adding carbon black particles to an insulating polymer matrix. Three different types of carbon black have been used and the polymer chosen is the photoresist SU-8, since the composites have to be structured by UV lithography and since SU-8 also was chosen as one of the base materials within the NOVOPOLY project.
The chapter describes how composites of different carbon black concentrations are mixed through ultrasonication and structured by UV-lithography. The composites are characterized with respect to their resistivity and the gauge factors.
The piezoresistive behavior of carbon black filled polymer composites have been used for sensing organic vapors, such as ethanol and acetone [56–58].
Throughout the chapter, both "carbon black" and the abbreviation "CB" will be used.

5.1 Composite fabrication

As there are no commercially available carbon black filled photoresists, it was decided to fabricate the composite ourselves. This also had the advantage, that composites at arbitrary carbon concentrations could be fabricated.

5.1.1 SU-8 polymer

SU-8 is a negative toned epoxy based photoresist originally developed at IBM, consisting of SU-8 monomers, organic solvent and a photo acid generator (PAG) [59]. The PAG is sensitive to ultra-violet (UV) light (350-400 nm), hence upon UV-exposure the PAG generates an acid, which opens the epoxy rings and the

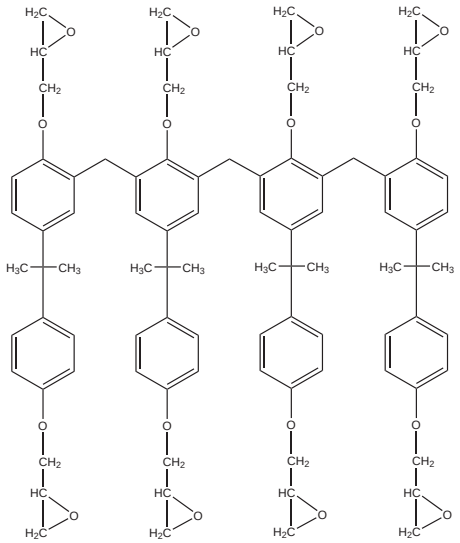

Figure 5.1: Chemical structure of the SU-8 monomer. The "8" refers to the eight epoxy groups of the SU-8 monomer.

crosslinking starts. Due to its good mechanical and thermal properties, SU-8 has been used for a number of applications such as microfluidic chambers and optical components including lasers, lenses and waveguides [60–63]. SU-8 is biocompatible [64] and has excellent chemical resistance to solvents, acids and bases.

5.1.2 Carbon black

Table 5.1: Carbon black particles

Particle	Mean size [nm]	Surface area [m^2/g]	Oil absorption number [mL/100 g]
Printex XE2	30	600	370
CD 975U	21	242	169
CD 7051U	56	43	121

Carbon black is a form of amorphous carbon, with an extremely high surface area to volume ratio, which is usually produced by the incomplete combustion of petroleum. Carbon black has been chosen as the conductive filler material, since it is very inexpensive compared to other common conductive fillers such as carbon nanotubes or metallic nanoparticles.
Three types of carbon blacks with different characteristics have been used for the

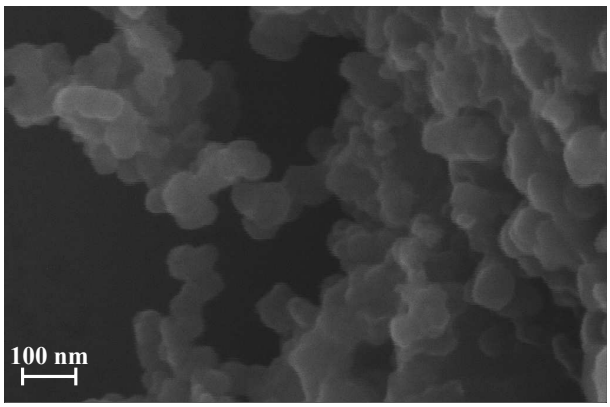

Figure 5.2: SEM picture of CD975U carbon black particles in SU-8 polymer.

fabrication of composites: Printex XE2 from Degussa and CD975U and CD7051U from Columbian Chemical Company. Printex XE2 is a high structure carbon black, while the latter two are lower structure carbon blacks. The main characteristics of the particles are summarized in table 5.1 as supplied by the manufacturers.

5.1.3 Mixing

To fabricate a uniform composite, the carbon black particles need to be homogeneously dispersed in the polymer matrix. There are several techniques to do this including shear mixing [23], ball milling [26, 44], dissolver disc [65] and ultrasonic mixing [66]. Depending on the type of polymer, mixing at temperatures above the glass transition temperature of the polymer is also used [39]. Shear mixers, ball millers and dissolver disc mixers require larger sample volumes, but since only small sample volumes (~6 mL) are used, ultra sound mixing was chosen. Ultrasound has previously been used for successful mixing of carbon nanoparticle doped SU-8 [67]

Carbon black doped composites were prepared by carefully weighing the carbon black particles on an electronic scale with 0.1 mg precision and adding them to the SU-8. As the composite is to be spin coated on a silicon wafer, SU-8 2002 from MicroChem has been used, since it has a high solvent content (~29% SU-8 and ~71% cyclopentanone) [68]. Typical quantities are 6 mL of SU-8 and 50 – 500 mg of carbon black.

The concentration of carbon black, C_{CB}, is calculated in wt% as

$$C_{\mathrm{CB}} = \frac{M_{\mathrm{CB}}}{M_{\mathrm{SU\text{-}8}} + M_{\mathrm{CB}}}\% \,, \tag{5.1}$$

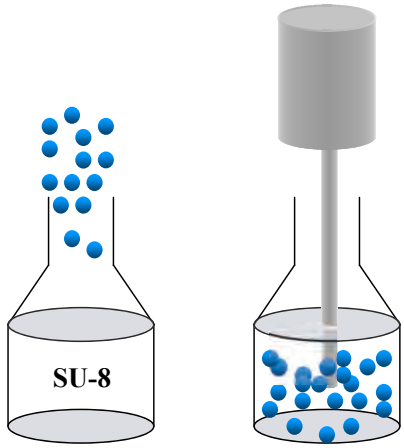

Figure 5.3: Schematics of the mixing procedure. The tip of the ultrasonic mixer is placed directly in the composite.

where it is assumed that all the solvent evaporates during thermal baking of the composite. The composite is placed in a 15 mL non-transparent plastic bottle to block outside light and ultrasonically mixed at 20 kHz for 10 minutes using a BioLogics Model 150 V/T ultrasonic homogenizer with a μ-tip. As the tip is placed directly in the composite during mixing heat is generated, so the bottle is immersed in ice water to cool it down and prevent evaporation of solvent. If no cooling is provided, the solvent quickly evaporates and spin coating becomes impossible.

To check the homogeneity of the composites, a series of experiments were carried out, where the duration of the ultrasound mixing was varied. Figure 5.4 shows optical pictures of thin films of an 8% XE2/SU-8 composite for different mixing times. The black dots are 5-25 μm sized clusters were the carbon black has not been properly wetted by the SU-8. As the mixing time is increased, the amount of clusters goes down however, clusters are also seen for the longer mixing times.

It turned out that generation of heat was a major problem for the heavily doped carbon black composites. Even though cooling was provided, the composites heated up and the solvent evaporated, making the composites too viscous for spin coating. In the end, a mixing time of 10 minutes was chosen in order to have the same mixing time for all composites. Table 5.2 summarizes the carbon concentrations of the fabricated composites.

Figure 5.5 shows SEM images of $\sim$ 2 μm thick 10% and 25% CD975U/SU-8 composite thin films. One can clearly see how the carbon black particles form an aggregated structure. It is important to note, that even under the best mixing conditions some aggregation will occur, since carbon particles tend to cluster [39].

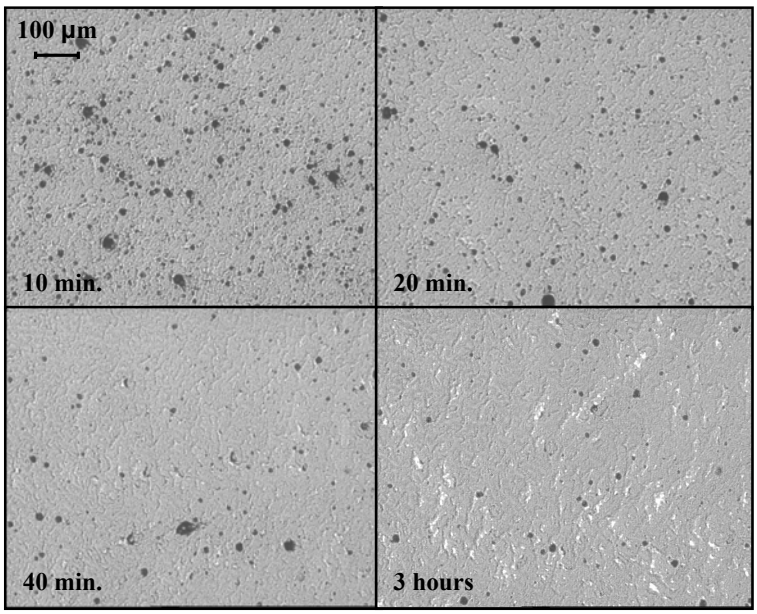

Figure 5.4: Optical pictures of thin composite films of 8% XE2/SU-8 2002 composites mixed at different times. The amount of clusters goes down as the mixing time is increased; however, clusters are also present for the long mixing times.

Table 5.2: Carbon black/SU-8 composite concentrations

Particle	Concentration [%]
Printex XE2	0.9, 1.4, 2.2, 3.2, 3.8, 5.0, 6.5, 8.7, 11.1
CD 975U	5.1, 10.7, 15.0, 19.9, 25.3
CD 7051U	4.8, 10.6, 20.0, 25.0

Carbon black particles are negatively charged, so they have a repulsive Coulomb interaction. They also have an attractive van der Waals term, so if the thermal energy is sufficient to overcome the electrostatic barrier, the pair of particles can be trapped in an energy minimum and become irreversibly aggregated [23].
One way to control the aggregate formation is to add ions to the composite. The added charges will affect the interactions between the particles. This will modify the aggregate formation, which in the end determines the electrical properties of the composites [23, 69].
It is important to note, that from looking at the microstructure of the composites, it is very difficult to deduce the electrical properties. Are the composites conductive/piezoresistive? From SEM pictures, such as the ones in figure 5.5, you can get an idea about the structure of the composite, but to know the exact electrical properties, you will have to measure them experimentally.

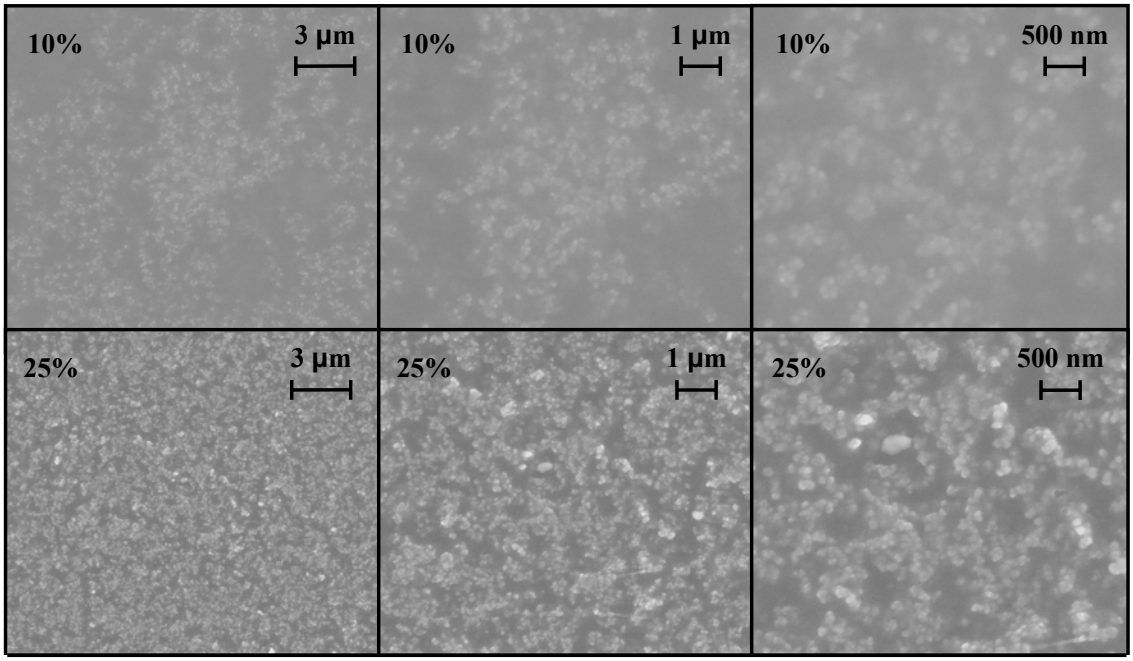

Figure 5.5: SEM images of ~2 μm thick 10% and 25% CD975U/SU-8 composite thin films. The aggregated structure of the composites is clearly visible. The images were obtained with a FEI Nova 600 NanoSEM in low vacuum mode to prevent charging effects.

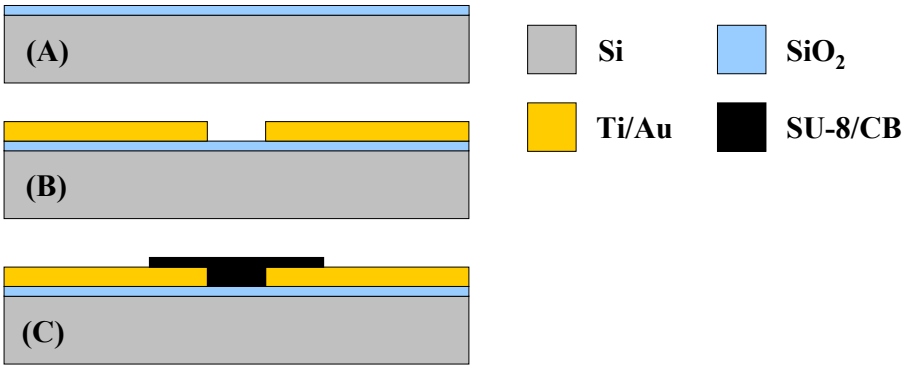

Figure 5.6: Schematics of the chip process recipe (not to scale).

5.2 Chip fabrication

The process sequence of the chip is shown in figure 5.6. The chips were fabricated at the DTU Danchip cleanroom facility through the following steps:
(A) 1500 Å thick SiO_2 layer is thermally grown on top of a 4" Si wafer for electrical insulation. (B) 50/3000 Å Ti/Au is e-beam evaporated on top of a patterned layer of AZ 5214E photoresist and electrodes are defined by a lift-off process. (C) 1.5-2.0 μm thick SU-8/CB composite is spin coated and UV-structured. Finally the chips are diced out from the wafer. For the process parameters see appendix A.

5.2.1 Spin coating

The composites are spin coated at 4000 rpm for 40 s at low acceleration on a manual spinner. Figure 5.7 shows the average measured thickness as a function of the CB concentration. As the amount of carbon is increased, the composite gets more viscous and this is also reflected in the increased thickness. The error bars indicate ± one standard deviation from the average and it can be seen that it increases with the CB concentration, so for higher carbon loadings, the surface gets more rough.

5.2.2 UV exposure and development

As shown in figure 5.8, UV lithography still works for the spin coated CB/SU-8 polymer composites, even though some of them are completely non-transparent and carbon black is known to block UV light [70]. Off course there must be an

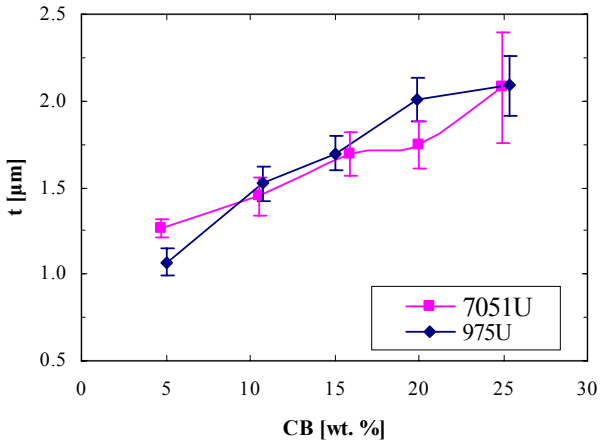

Figure 5.7: The graph shows the average thickness of spin coated thin films of CB and SU-8 as a function of the thickness. The error bars indicate ± the standard deviation, σ, from the average. The thickness was measured with a Dektak 8 profilometer.

upper limit, where the CB concentration is too high for UV-lithography to be possible, but for the film thicknesses used (~2 μm), composites of up to 25% CB loading have been UV-structured without problems. As the resolution is not critical in the design, a large exposure dose of ~ 1.5 J/cm^2) was chosen to be sure to completely crosslink the composite. For the non-transparent composites, the gold alignment marks were not visible, so it was necessary to remove some of the composite material with a cleanroom tissue and acetone, in order to be able to do the alignment.

After UV exposure the CB/SU-8 composite is developed in PGMEA (propylene glycol methyl ether acetate) to remove non-crosslinked SU-8 and finally rinsed in isopropanol. Figure 5.9 (left) shows a UV structured composite after development. The crosslinked structures are seen as yellow squares, but the wafer is also completely covered by a residual layer of carbon sticking to the wafer, where the non-crosslinked SU-8 has been removed. This is off course not wanted, so the carbon was removed by dipping the wafers shortly (2-3 s) in an ultrasound water bath. This is off course a rather harsh treatment and for he highly doped composites it in some cases damaged the crosslinked structures.

Another way to remove the residual carbon layer is to give the wafers a plasma ashing treatment. A plasma asher creates a reactive plasma, which combines with the material (commonly used to remove photoresist) to produce ash, which is then removed. Figure 5.9 shows a wafer before and after the plasma asher treatment. An O_2/N_2 plasma of 150/50 ml/min at 150 W was used for a period of 7×1 minute and one can clearly see that the residual carbon layer has been removed. Since the

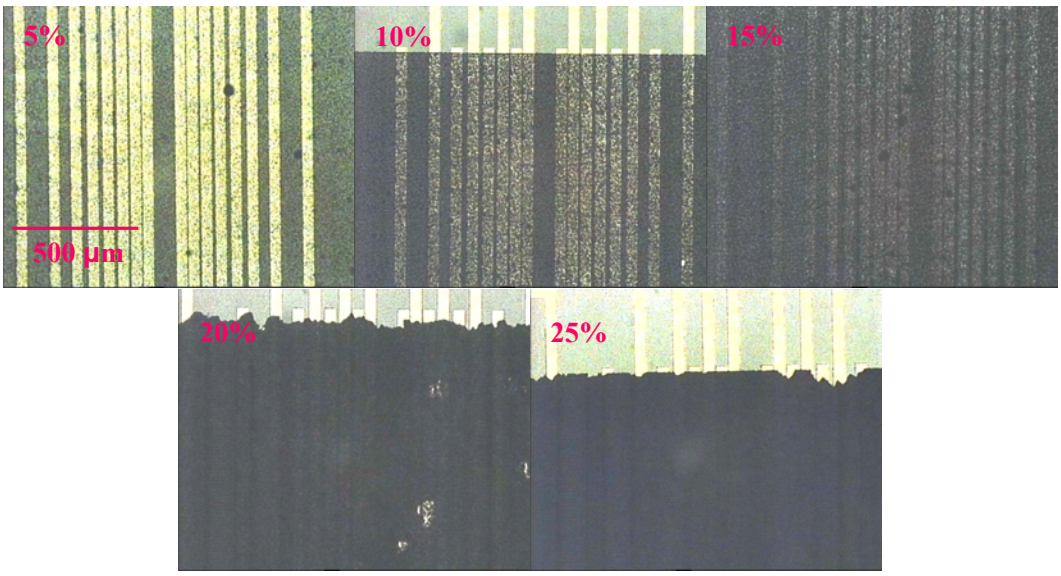

Figure 5.8: Optical pictures of composite thin films of SU-8 2002 and CD7051U at five different carbon loadings. The composites are spin coated and UV-structured on top of a 4" Si wafer. Gold electrodes are seen underneath.

whole wafer is exposed to the plasma, one have to optimize the recipe, such that the residual carbon layer is removed, without damaging the UV-exposed structures.
Yet another possibility, which was not tried, is to use a surfactant (soap) to remove the carbon particles.

5.3 Measurements

The fabricated chips have been investigated using the four-point bending fixture described in chapter 4. Electrical resistances were measured with the two-probe electrode configuration and used to calculate the electrical resistivities of the three types of carbon black particles at different carbon concentrations. This can be used to locate the percolation threshold, υ_c, at which the composites should have the maximum strain sensitivity.
Gauge factors have been measured for the different composites using the four-point bending fixture.
When approaching the glass transition temperature of the polymer ($T_{g_{SU\text{-}8}}$ = 200°C) you would see a drastic increase in the resistivity due to the difference in the thermal expansion coefficients of polymer and filler [71]. However, the electrical properties of carbon black filled polymers have been shown to be stable at ambient

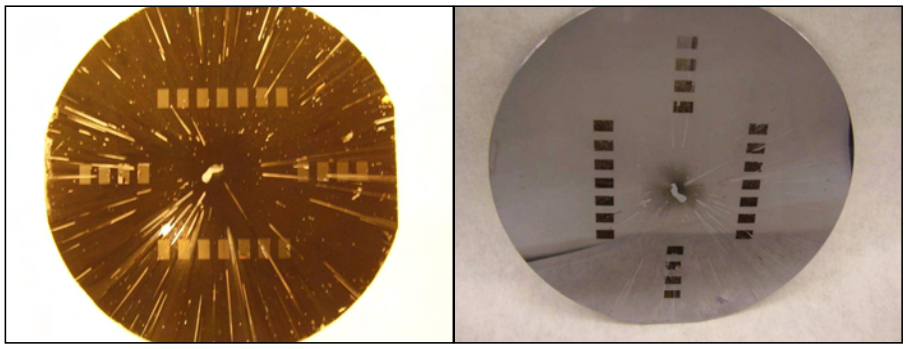

Figure 5.9: LEFT: A 4" inch silicon wafer with UV-structured SU-8/CB composite (12% XE2) after development in PGMEA. The yellow squares are the crosslinked structures, but a residual layer of CB is sticking to the wafer, where the non-crosslinked SU-8 has been removed. RIGHT: The same wafer after plasma ashing, where the residual CB has been removed.

temperatures, hence all measurements were carried out at room temperature [25].

5.3.1 Resistivity

The resistivity has been calculated for the different fabricated composites as

$$\rho = \frac{Rwt}{L}, \tag{5.2}$$

where R is the measured two-probe resistance and w is the width, L is the length and t is the thickness of the composite as measured with a stylus profiler. Figure 5.10 shows a semi-log plot of the resistivity, ρ, of the polymer composites as a function of the carbon black concentration. As the amount of carbon is increased, the resistivity drops $4-6$ orders of magnitude and a transition from insulator to conductor is observed. The highest doped composites have resistivities of $\rho \sim 1.0 \cdot 10^{-2}$ Ωm, which is in the semiconductor region and the lowest doped composites have resistivities of $\rho \sim 1.0 \cdot 10^{5}$ Ωm. As a reference, amorphous carbon has a resistivity of $\rho_{\text{carbon}} = 3.5 \cdot 10^{-5}$ Ωm.

The percolation threshold can be determined as the concentration, at which the resistivity has a drastic increase. An exact determination of the percolation threshold would involve a best fit to equation 3.2 however, in this work an estimation of the percolation threshold is good enough. For XE2, the percolation threshold can be estimated from figure 5.11 and one finds $\upsilon_c = 1-2\%$. This value is quite low, however XE2 is a high structure carbon black with an oil absorption number (OAN) of 380 ml/100 g. High structure carbon blacks form elongated aggregates and are known to give low values for the percolation threshold [45, 72].

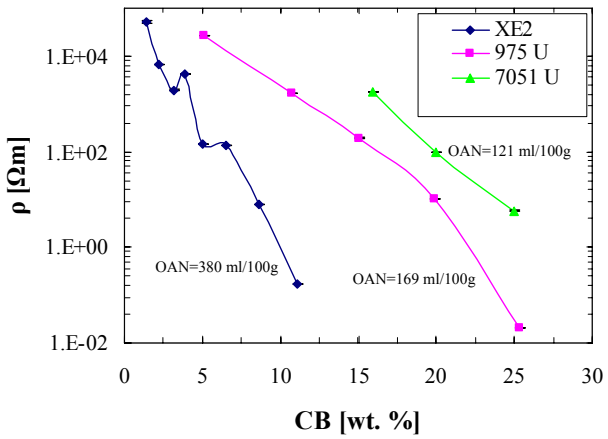

Figure 5.10: The resistivity, ρ, as a function of nanoparticle content. A clear insulator to conductor phase transition is observed.

For CD975U and CD7051U the resistivities for the lower nanoparticle concentrations were too high to be measured with the present setup, hence we cannot positively say that the percolation threshold was reached. However, figure 5.10 suggests that CD975U and CD7051U should have higher percolation thresholds than XE2, because a higher concentration of nanoparticles is needed to reach a resistivity equivalent to XE2. This is also what one could expect, since CD975U and CD7051U is a lower structure carbon black, with OAN values of 169 ml/100 g and 121 ml/100 g, respectively. Lower structure carbon blacks do not form highly aggregated structures, hence a larger amount of carbon nanoparticles is needed to make the composite conductive.

5.3.2 Piezoresistivity

The basic behavior of the polymer composites was tested in a measurement series, where 160 MPa tensile and compressive stress was applied alternately to an 8.7% XE2 composite. The stress corresponds to a strain of $\varepsilon = 0.11\%$. Figure 5.12 shows the measured two-probe resistance, R, as a function of time. The figure has nine time intervals of 120 s corresponding to periods of: stress released, non-zero tensile stress, stress released, non-zero compressive stress, stress released and so on.

From the figure it is clear, that the behavior is as expected, (a): Onset of tensile (compressive) stress, (b): Interparticle distance is increased (decreased) and R increases (decreases), (c): Tensile (compressive) stress is released and (d): Interparticle distance is decreased (increased) and R returns to its initial value.

As can be seen from figure 5.12, the baseline R_0 drifts, but the *height* of the

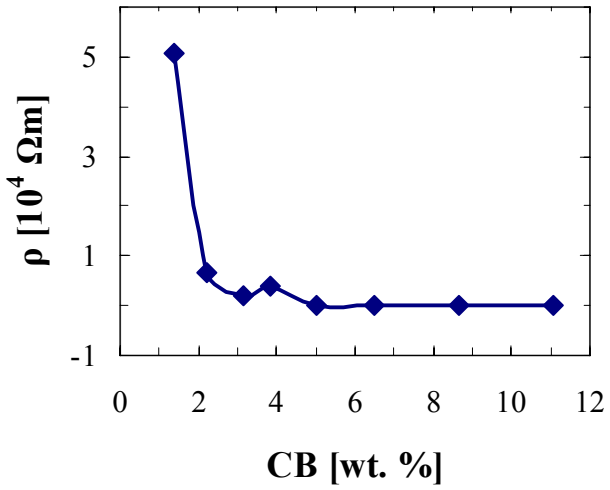

Figure 5.11: The resistivity ρ, as a function of the XE2 concentration. The percolation threshold is determined to be $\upsilon_c = 1 - 2\%$.

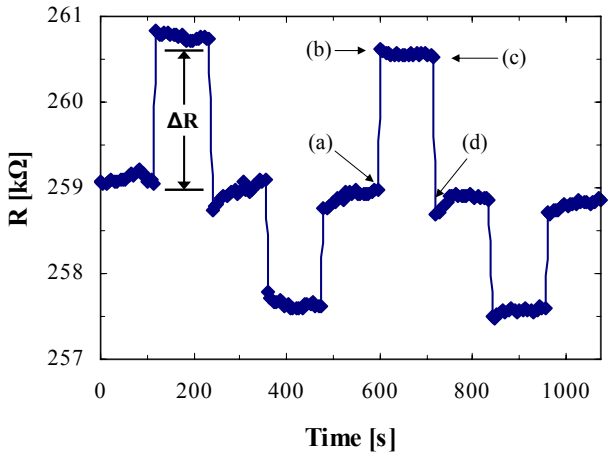

Figure 5.12: An 8.7% XE2/SU-8 composite, where tensile and compressive stress is applied alternately (200 μm resistor). (a) Tensile stress applied, (b) interparticle distance is increased and R increases, (c) tensile stress released and (d) interparticle distance is decreased and R returns to initial value. The peaks correspond to time intervals of nonzero tensile stress and the valleys to periods of nonzero compressive stress.

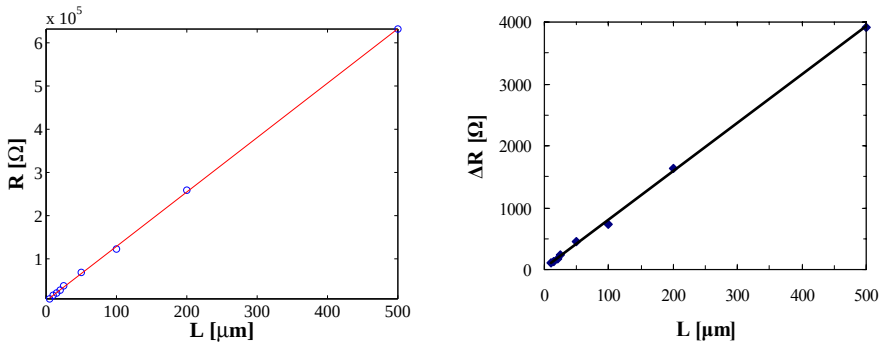

Figure 5.13: R vs. L (left) and ΔR vs. L (right) plots for the data series in figure 5.12.

peaks is stable, which means that the piezoresistive effect is reversible. A reversible piezoresistive effect has previously been reported for macro-sized structures [25, 73, 74]. It is thus verified, that a similar behavior is found for micro structures.

For an ideal system with no contact resistance and no resistance of the measurement setup, one would have that $R \to 0$ for $L \to 0$, where R is the measured two-probe resistance and L is the length of the resistor. By plotting the resistance as a function of the length, the contact resistance can be estimated as $R_{\text{contact}} \approx R|_{L\to 0}$, which is the crossing of the R-axis. Figure 5.13 (left) shows an R vs. L plot for the measurement series in figure 5.12. A straight line is fitted and $R_{\text{contact}} = 2900\ \Omega$.

More importantly, the contact resistance was found for all the nine time intervals in figure 5.12 and it showed that the R_{contact} was constant throughout the whole tensile/compressive strain cycle. It means, that the observed change in resistance, ΔR, when a stress is applied in figure 5.12, is *not* just a change in the contact resistance, but it is a piezoresistive contribution from the polymer composite.

This can be further verified by plotting ΔR as function of the length, shown in figure 5.13 (right). A straight line is observed, hence ΔR scales linearly with the length of the resistor. If ΔR was just a change in the contact resistance one should not expect a straight line.

As $\Delta R/R = K\varepsilon$, the gauge factors can be calculated to $K = 5 - 6$. Assuming $\nu_{\text{SU-8}} = 0.22$ as Poisson's ratio for SU-8 and using equation 2.7 one gets $K_{\text{geo}} = 1.5$, hence the geometrical gauge factor cannot alone explain the observed change in resistance, so it can be concluded that $K_{\text{piezo}} > 0$.

Piezoresistive behavior of carbon loaded composites has previously been reported for macroscopic samples [75–77].

5.3.3 Contact resistance

To estimate the contact resistance, R vs. length plots were made for all the fabricated composites.
For the highly doped composites the contact resistances were found to be small and constant with respect to the applied stresses, hence they can be neglected when calculating the gauge factors.
For the lower doped composites with high resistivities, the measured resistances were often too large to be measured with the Keithley 2700 Multimeter, which has a range of $0 - 100$ MΩ. In many cases, only the resistances for the shortest resistors, $L_{1-3} = 5, 10, 15$ μm, could be measured. This gives not enough data points to make a reasonable R vs. L plot to estimate the contact resistance.

The problem can be illustrated by plotting R vs. L for a 2.2% XE2 composite shown in figure 5.14. For $L > 15$ μm, the resistance exceeds 100 MΩ and cannot be measured with the setup. Although figure 5.14 only has 3 data points, the behavior does not seem to be linear. It is believed this is connected to the coherence length of the composite (the diameter of the largest, but finite cluster). For lower doped composites the coherence length is small, hence when L becomes comparable to the coherence length of the composite one would expect a dramatic increase in the resistance.
In the following, it will be assumed that the contact resistance is small and stays constant when a strain is applied, hence it will be neglected, when calculating gauge factors. There are some arguments that support the assumption of a low contact resistance:

- The polymer composite is spin coated on top of the gold electrodes and afterwards cured at 90°C. The polymer composite is highly crosslinked and thus firmly attached to the gold electrodes. This should minimize the contact

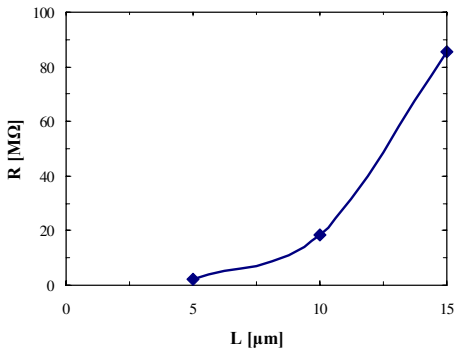

Figure 5.14: R vs. length for a 2.2% XE2 composite. For $L > 15$ μm, $R > 100$ MΩ, hence it is out of the range of the Keithley 2700 Multimeter.

resistance.

- The contact interface between polymer composite and gold electrodes, $A_{\text{contact}} = 0.3\ \text{mm}^2$, which is large compared to the dimensions of the resistors.

- The polymer composite is deposited on top of the electrodes and since the applied strain is parallel to the length axis of the chip, there are no forces orthogonal to the contact interface, which could affect the contact resistance by pressing the polymer/electrode interface together or tearing it apart. together.

For carbon filled polymers, negligible contact resistances have previously been reported [78–80].

5.3.4 Gauge factors

The gold electrodes of the chip are also subjected to the applied strain. Gold has a gauge factor of $K_{\text{Au}} = 3$, hence the electrodes will also give a contribution to the resistance change. The maximum piezoresistive contribution was estimated to $\Delta R_{\max_{\text{electrodes}}} \leq 0.3\ \Omega$, which is much smaller than the measured resistance changes from the composites. In the following, the piezoresistive contribution from the gold electrodes is thus neglected.
Gauge factors have been measured for composites of the three different types of carbon blacks at different filler concentrations. The gauge factors were determined in two different ways:

1. A tensile stress of 160 MPa, corresponding to a strain of $\varepsilon = 1.1 \cdot 10^{-3}$, was applied in a cyclic manner, hence 2 minutes of stress released, 2 minutes of non-zero stress, 2 minutes of stress released and so on. Three complete cycles were made for a total of 14 minutes. Figure 5.15 (left) shows the measured resistance, R, as a function of time for a 6.5% XE2 composite. As $\Delta R/R_0 = K\varepsilon$, where K is the gauge factor and ε is the applied strain, the gauge factor can be calculated from the values of the graph: ΔR is the height of the peaks and R_0 is the baseline.
   For the three peaks a gauge factor of $K = 11$ is found. The spike observed at the start of each stress cycle is due to the fact, that a weight load is manually placed on top of the four point bending probe. Even though the weight is loaded very gently, the stress goes momentarily up, however, the resistance rapidly stabilizes.

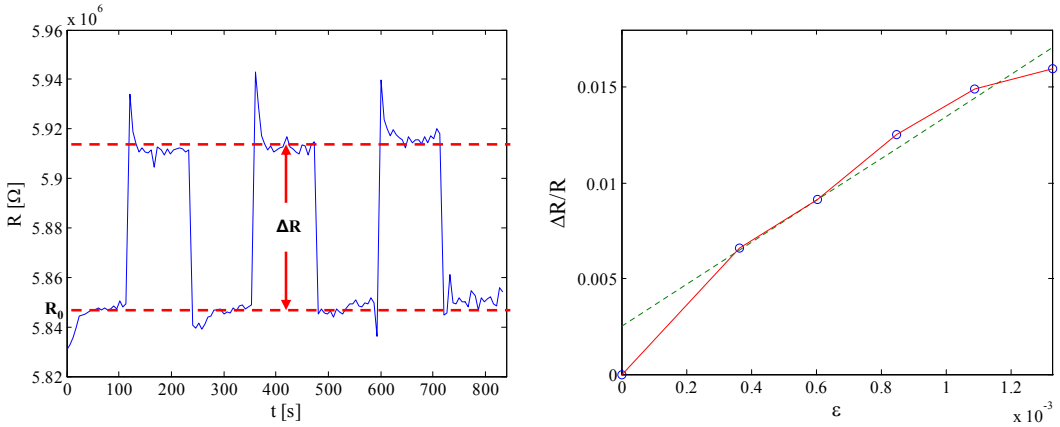

Figure 5.15: LEFT: R as a function of time for a 6.5% XE2 composite, where a tensile stress of 160 MPa corresponding to a strain of $\varepsilon = 1.1 \cdot 10^{-3}$, is applied in a cyclic manner. R_0 and ΔR is found from the graph and for the three peaks gauge factors of $K = 11$ is found.
RIGHT: $\Delta R/R$, as a function of the strain, ε. A linear fit (the dotted line) is made in the interval $\varepsilon \geq 0.37 \cdot 10^{-3}$ and from the slope one gets $K = 11$ for the gauge factor.

2. A tensile stress is stepped from zero to 200 MPa in five equidistant steps over a period of 10 minutes. If $\Delta R/R$ is plotted as a function of the strain, ε, the gauge factor can be found as the slope of the graph.
   Figure 5.15 (right) shows a plot for a 6.5% XE2 composite. A linear behavior is not observed in the whole strain range. Using a simple model involving electron tunneling between homogeneously dispersed spherical filler particles, Zhang et al. have also measured and theoretically explained the non-linear behavior of the $\Delta R/R$ vs. ε curve [81,82]. They have used carbon black and copper- and aluminum powder as filler material and polyethylene, polystyrene and epoxy resin as insulating matrices.
   To estimate the gauge factor, it was decided to make a linear fit (the dotted line) in the interval $\varepsilon \geq 0.37 \cdot 10^{-3}$, since the strain applied in method (1) lies in this interval. A gauge factor of $K = 11$ is found. There is good agreement between the gauge factors measured with method (1) and (2).

Gauge factors have been measured for the three different types of carbon black, XE2, CD975U and CD7051U at different carbon concentrations. Figure 5.16 shows the measured gauge factors, K, as a function of the resistivity, ρ, for the different composites. The graph represents measurements for several chips and the error bars indicate the range of the measured values. Depending on the type of carbon black and the concentration, piezoresistive responses with gauge factors

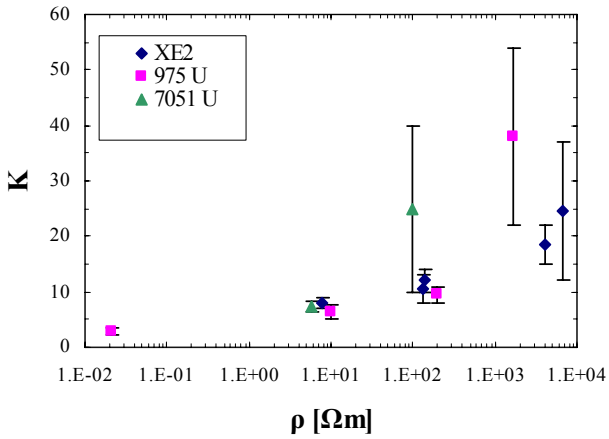

Figure 5.16: The gauge factor, K, as a function of the resistivity, ρ. The gauge factors increase as the resistivity is increased, however the spread in the measured values also increase (indicated by the error bars). The data presented represents measurements for several chips and at different electrode spacings.

of $K \approx 3 - 50$ have been observed.
It can be seen, that a lower resistivity gives smaller, but more reliable gauge factors. Larger gauge factors are found at higher resistivities and they are also associated with a much larger spread in the measured values. This behavior has previously been reported for carbon black loaded polymer composites [50].

5.3.5 Fluctuations

One can illustrate the trends observed in figure 5.16 by plotting the resistance as a function of time. Figure 5.17 shows R vs. t for an 8.7% (left axis) and a 3.8% (right axis) XE2 composite, which have resistivities of $\rho_{8.7\%} = 8.0\ \Omega$m and $\rho_{3.8\%} = 4100\ \Omega$m, respectively. The measurement series are similar to the one in figure 5.15 (left).
For the 8.7% composite the three peaks give gauge factors of $K_{8.7\%} = 5.4, 6.1$ and 6.5, respectively. For the 3.8% XE2 composite it is $K_{3.8\%} = 14.6, 16.7$ and 18.9, respectively. The 3.8% composite thus has larger gauge factors, $K_{3.8\%} \approx 3K_{8.7\%}$, however the 3.8% composite has fluctuations of $\simeq$1%, whereas it is less than 0.1% for the 8.7% composite. Furthermore, the resistivity is much larger, $\rho_{3.8\%} \approx 500\rho_{8.7\%}$.
To monitor the fluctuating behavior of the composites, a series of drift measurements were carried out, where the resistance of the fabricated XE2 and CD975U composites was measured once every minute during one hour, with no stress applied. Figure 5.18 and 5.19 plots $\Delta R/R$ as a function of time for such a measure-

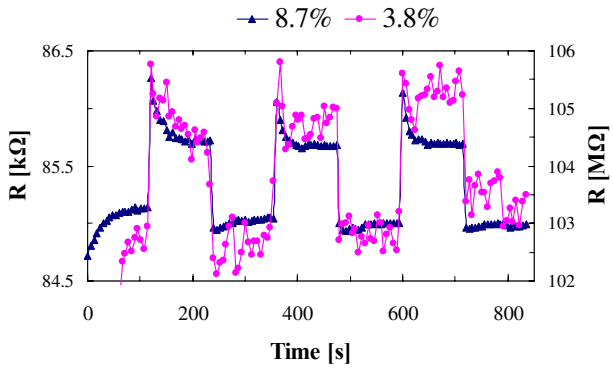

Figure 5.17: R vs. t for three tensile stress cycles of 180 MPa. The measured values are for a 3.8% (left axis) and an 8.7% (right axis) XE2 composite. Gauge factors of $K_{3.8\%} = 14 - 19$ and $K_{8.7\%} = 5 - 6$ are found, however, the 3.8% composite has a higher resistivity and the fluctuations are more than ten times larger than for the 8.7% XE2 composite.

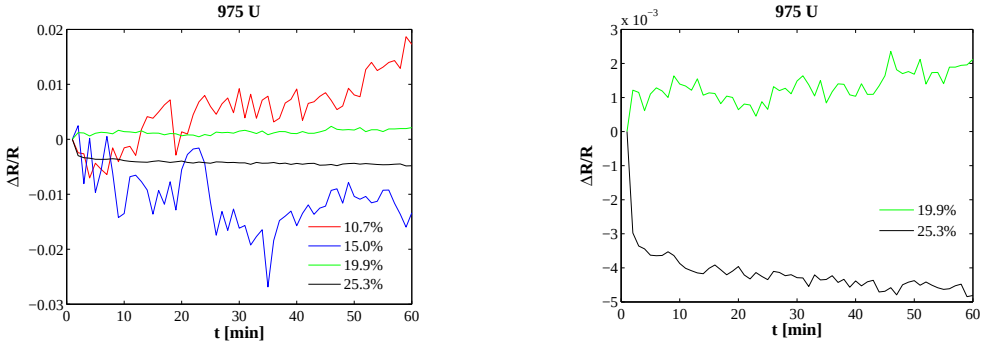

Figure 5.18: $\Delta R/R$ vs. t for a 1 hour drift measurement of the CD975U composites. The right graph shows a zoom in on the two highest doped composites.

ment series. The graphs clearly shows, that the fluctuations increase as the amount of carbon is decreased. The fluctuating behavior can be summarized by plotting the standard deviation of the resistivity as a function of the resistivity, $\sigma(\rho)$. The results shown in figure 5.20 yields a straight line in a log-log plot, hence as the resistivity increases, the fluctuations increase with a power law dependence.

A behavior similar to figure 5.20 has previously been reported and explained as 1/f-noise [35]. The conduction in the polymer composites has two channels. When adjacent particles touch, they can be described as in contact, while separated particles are "connected" through tunneling. As the composite gets more sparse the tunneling conduction starts to dominate, hence the electrical noise is controlled by the more noisy "tunneling network". This explains why the fluctuations increase as you move towards the percolation threshold from above.

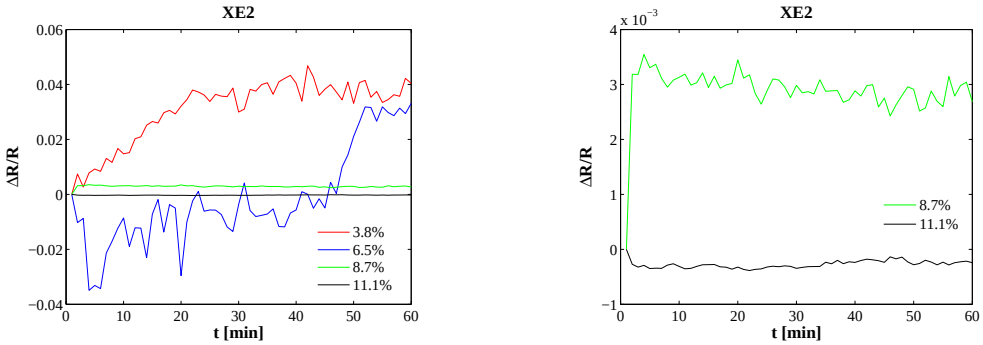

Figure 5.19: $\Delta R/R$ vs. t for a 1 hour drift measurement of the XE2 composites. The right graph shows a zoom in on the two highest doped composites.

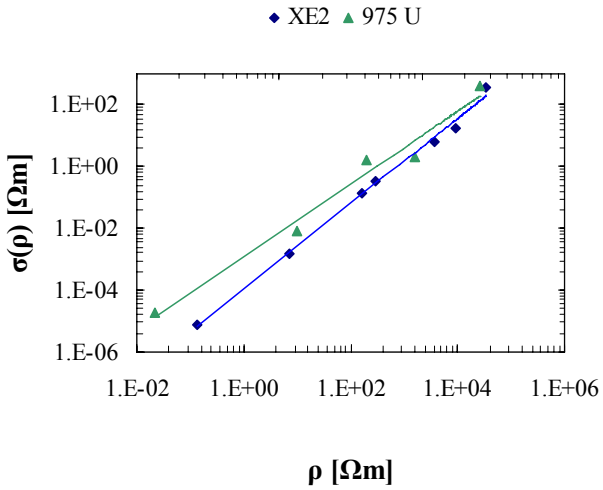

Figure 5.20: The standard deviation of the resistivity, $\sigma(\rho)$, as a function of the resistivity for the XE2 and 975 U composites. The graph shows a straight line in a log-log plot indicating a power low dependence.

5.4 Summary

Piezoresistive composites have been fabricated by adding carbon black nanoparticles to the electrically insulating negative photoresist polymer SU-8. The composites were mixed using an ultrasonic homogenizer. Three different types of carbon black have been used.
Chips with spin coated thin layers of composite material have been fabricated in a cleanroom. Although the composites in some cases are completely non-transparent, they are still possible to structure by standard UV lithography.
The electrical resistivity has been measured for the composites. As the amount of carbon black is increased an insulator to conductor transition is observed spanning $4-6$ orders of magnitude. The percolation threshold was estimated for the three different carbon blacks and the location of the percolation threshold seemed to be correlated with the structure of the carbon black particles, such that higher structure carbon blacks give lower percolation thresholds.
A reversible piezoresistive effect has been proved for the composites. Gauge factors of $K \approx 3-50$ have been observed and with the largest values close to the percolation threshold. Frazier et al. have reported similar results for graphite filled polyimide thin film membranes for use as pressure sensors in microdevices. They have measured maximum gauge factors of $K = 16.8$ and they also observe that the gauge factors increase as you move towards the percolation threshold [26].
It is found, that the resistivity and the strain sensitivity is correlated, such that a higher resistivity gives larger gauge factors. The high resistivity composites are more noisy than the low resistivity composites and in general the results are more consistent for composites with a lower resistivity.
For the lower resistivity composites, a stable and reversible piezoresistive effect with gauge factors of $K = 6-10$ has been observed. These composites are valid candidates for the piezoresistive readout of cantilever sensors.
Whether the high resistivity composites, with gauge factors up to $K \approx 50$, can be used for the piezoresistive readout in cantilever sensors, will depend on the ability to remove the noise from the signal. This has to be investigated in a thorough noise analysis.

Chapter 6

Silver nanoparticle SU-8 composites

As an alternative to carbon black doped polymer composites, this chapter investigates silver nanoparticle doped SU-8 composites. Since the composites are commercially available, mixing of the composites is avoided.
Silver nanoparticle doped thin film composites at different filler concentrations have been structured and the conductive and piezoresistive properties have been characterized. Finally, a batch of silver doped SU-8 cantilevers have been fabricated.

6.1 Processing

Silver nanoparticle doped SU-8 is commercially available from Gersteltec, Lausanne, Switzerland [83]. The product consists of SU-8, the solvent γ-butyrolactone (GBL) and silver nanoparticles. The size distribution of the silver nanoparticles is shown in table 6.1 as supplied by the manufacturer [84]. Figure 6.1 shows an SEM image of one of the structured composites and one can see $300 - 600$ nm sized silver particles. The percolation threshold for the silver composites is $\upsilon_c \approx 6\%$ by volume, hence composites were purchased at 4, 6, 8 and 12% to cover the whole range from below, at to above the percolation threshold [85].

Chips with two- and four-probe electrode configuration have been fabricated.

Table 6.1: Silver nanoparticle size distribution

Size distribution at	Result [μm]
10%	0.2
50%	1.5
90%	2.5

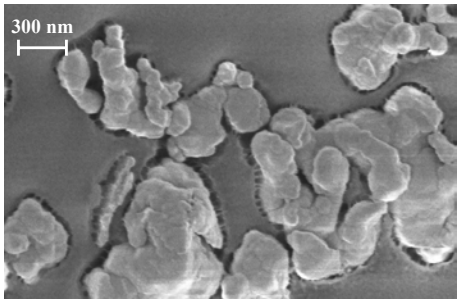

Figure 6.1: SEM picture of silver nanoparticles in SU-8.

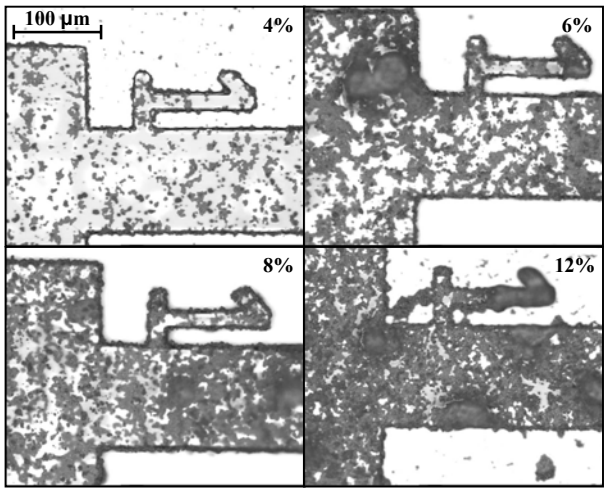

Figure 6.2: Optical micrographs of thin film UV-structured silver/SU-8 composites. As the amount of silver is increased the density of silver clusters increases.

The process sequence is similar to the one in figure 5.6 for the SU-8/carbon black composites, but the baking times have been extended and the exposure doses optimized for the silver/SU-8 composites. For the process parameters see appendix B.

In the case of the four-point electrode chips, the resolution is critical, hence the exposure dose was optimized for the different silver concentrations. The exposure dose was set to 495 mJ/cm^2 for the 4, 6 and 8% composite and 675 mJ/cm^2 for the 12% composite. Figure 6.2 shows an optical picture of thin films of UV-structured composites for the four different silver concentrations. One clearly sees how the aggregate density increases with the silver loading.

No spin coating standardization data is available for the purchased composites. Instead, it is suggested from the supplier to control the thickness of the composites by scraping them on a quartz wafer and do the UV exposure from the backside.

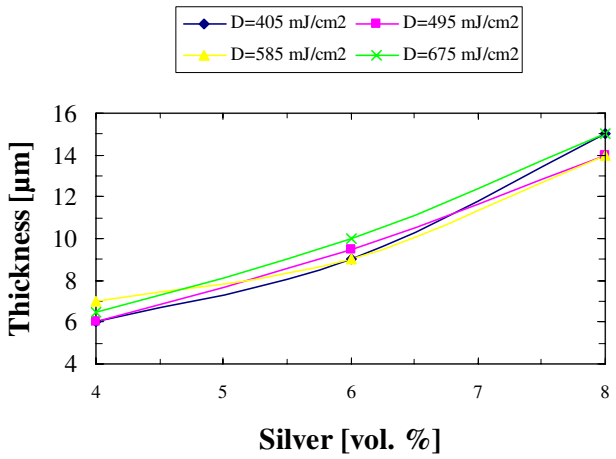

Figure 6.3: Thickness of silver/SU-8 composites measured with a Dektak 8 profilometer.

By adjusting the exposure dose one can then control the crosslinked thickness. Quartz wafers are not compatible with the process sequence, but as the thickness is not critical in the design, no optimization of layer thickness was carried out. Figure 6.3 shows the averaged measured thickness of the composites for different exposure doses. The spin speed was set at 4500 rpm for 40 s at low acceleration and the thickness are between 6 and 15 μm depending on the silver concentration. The data for the 12% composite is not included in the graph, since the structures were very rough, with thicknesses between 10 and 30 μm.

6.2 Measurements

Measurements have been carried out for both the chips in two- and four-probe electrode configuration

6.2.1 Two-probe measurements - resistivity

Two-probe resistances have been measured for the composites and the resistivities have been calculated according to equation 5.2. The minimum and maximum measured values for each composite are summarized in table 6.2 along with the values from the supplier.

As can be seen from table 6.2, there is a huge difference between ρ_{min} and ρ_{max}. The results can be explained by plotting the resistance R, as a function of the length L, see figure 6.4. For the 4% and 6% composites, the resistance increases 4 orders of magnitude, when L goes from 50 to 100 μm. For the 8% composite,

Table 6.2: Silver/SU-8 resistivities

	ρ_{min} [Ωm]	ρ_{max} [Ωm]	$\rho_{supplier}$ [Ωm] [85]
4%	0.09	6400	50
6%	0.12	9800	$\sim 1.0 \cdot 10^{-3}$
8%	0.3	8000	$\sim 1.0 \cdot 10^{-3}$
12%	0.02	0.8	$\sim 1.0 \cdot 10^{-4}$

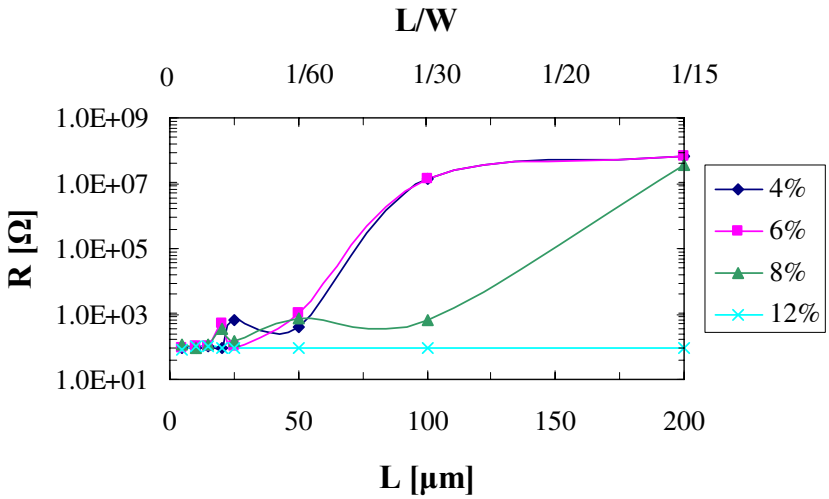

Figure 6.4: Semi-log plot of the resistance, R, as a function of the length of the resistor, L. For the 4%, 6% and 8% composite, the resistance was too high to be measured for $L = 500\,\mu$m. The corresponding L/W-ratios of the resistors are also shown.

the resistance increases 4 orders of magnitude, when L goes from 100 to 200 μm. For the 12% composite no exponential increase is seen.

Figure 6.4 gives information about the correlation length (the diameter of the largest, but finite clusters) of the four different composites. When the length of the resistor L, becomes larger than the correlation length of the composite, one would expect a drastic increase in the resistance. The correlation length can thus be estimated from figure 6.4 as the point, where the resistance has a sharp increase. For the 4 and 6% composite it is between 50 and 100 μm, for the 8% composite between 100 and 200 μm and for the 12% composite it is above 500 μm.
Figure 6.5 shows SEM images of the four composites. For the 4% composite isolated clusters are present, but as the amount of silver is tripled to 12% the silver aggregates are really close.

To verify that it actually is silver that is imaged, an X-ray image was taken. Figure 6.6 (left) shows and SEM image of a 4% silver composite and figure 6.6

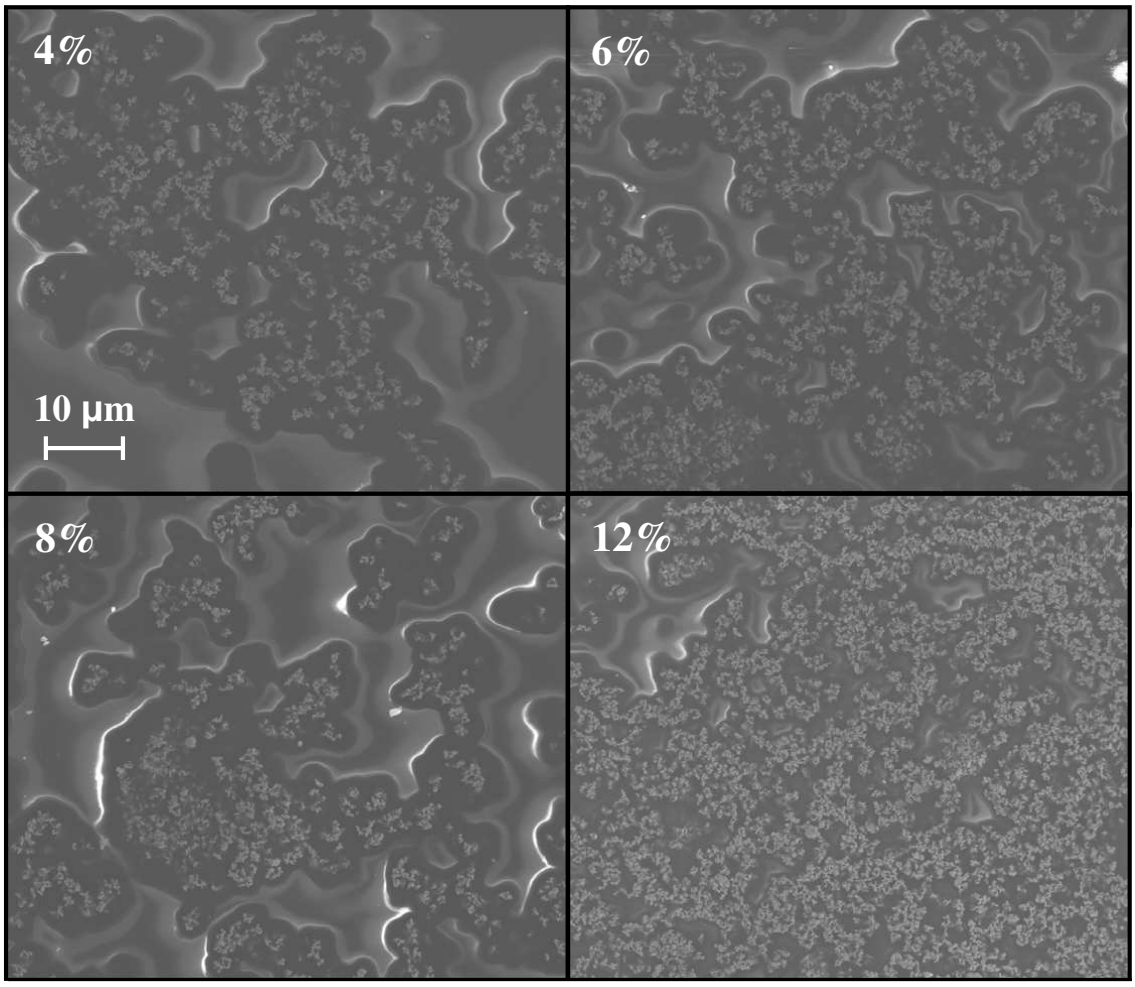

Figure 6.5: SEM images of the silver composites. The bright spots show the silver aggregates.

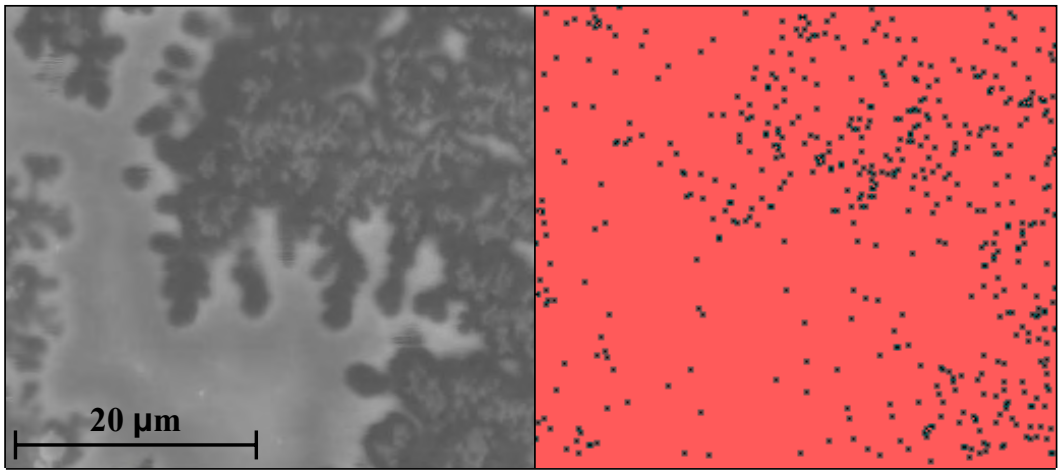

Figure 6.6: LEFT: SEM micrograph of a 4% silver composite.
RIGHT: Corresponding X-ray signal from silver. The black dots represent the number of the collected X-ray photons. The intensity is clearly largest from the areas with silver aggregates.

(right) shows the intensity of the collected X-ray photons from the same sample. The intensity of the X-ray photons is clearly largest from the silver aggregates.

For a 12% composite thin film, the sheet resistance R_s was also measured using a microscopic four-point probe from CAPRES A/S [86], see figure 6.7 for a schematics of the four-point probe principle. The probe has four cantilevers that are 1 μm thick, 6 μm wide, 30 μm long and have a pitch of 20 μm. The sheet resistance was measured on a 5×5 grid, measuring 50×50 μm^2. The resistivity was found by multiplying the measured sheet resistance by the film thickness, $\rho = R_s t$. Values were measured to ρ=6.3·10^{-4} – 1.8·10^{-3} Ωm, which is of the same order of magnitude as the values provided by the manufacturer.

One should note, that within the 50×50 μm^2 square, the resistivity varies a factor of 30. Some of it can be attributed to differences in the film thickness, but it is also clear when looking at figure 6.5, that it matters where you place your probe. If you place the probe directly in a silver cluster, the measured resistivity will off course be lower, than if you place it in outside a cluster.

For the other composites, the resistivity was too high to be measured with the microscopic four-point probe, since it can only measure resistivities below $1.0 \cdot 10^{-2}$ Ωm.

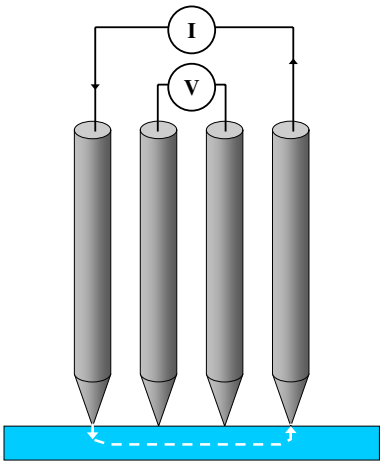

Figure 6.7: Schematics of the four-point probe principle. Four electrodes are touching the sample. A current is driven through the two outer electrodes and the voltage drop is measured across the two inner electrodes. The four-point probe can be moved to scan a larger sample area.

6.2.2 Two-probe measurements - piezoresistivity

To measure the piezoresistivity of the composites a series of measurements were carried out, where a stress was applied in a cyclic manner, hence 2 minutes stress released, 2 minutes of non-zero stress, 2 minutes stress released etc. Three complete cycles were made for a total 14 minutes with a tensile strain of ε=1.1·10^{-3}. Figure 6.8 shows the measured resistance, R, as a function of time for a 6% composite, for the resistor lengths, L=5 μm (left R-axis) and L=25 μm (right R-axis). From the figure one can find ΔR as the height of the peaks and one can see that $\Delta R = 0.25 - 0.3\ \Omega$. This is the inherent piezoresistive contribution one would expect from the gold electrodes, hence there does not seem to be a piezoresistive contribution from the composite itself. Furthermore, *if* the composite has a piezoresistive contribution, one would expect from the relation, $\Delta R = \varepsilon K R$, that $\Delta R_{25\mu m} = 5\Delta R_{5\mu m}$ since the length of the resistor is five times larger. Looking at figure 6.8 one can see that $\Delta R_{25\mu m} \approx \Delta R_{5\mu m}$, hence the piezoresistive contribution from the composite must be small or non-existing.
The 4, 8 and 12% composites show a similar behavior. The resistance change is identical for all the four composites, $\Delta R \approx 0.3\ \Omega$, hence there does not seem to be a piezoresistive contribution from the composites.

The purchased composites are mainly sold as conductive resists at higher loadings (30-40%), where the microstructure of the composites is not important as long as the composite is a good conductor. For a composite to have piezoresistive behavior, you need well dispersed filler particles, such that a complex conduc-

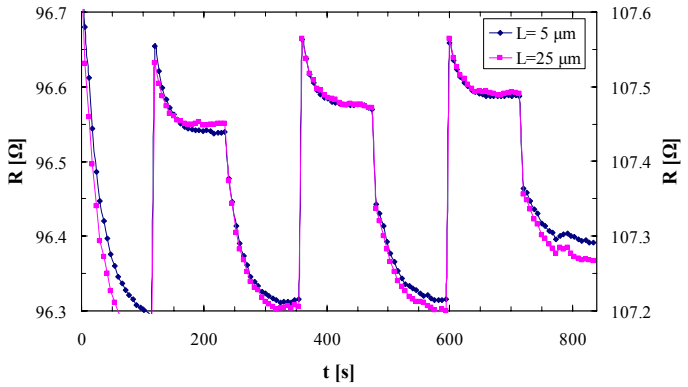

Figure 6.8: R vs. t for a 6% composite at the lengths $L = 5\ \mu$m and $L = 25\ \mu$m. One can see that $\Delta R_{25\mu m} = \Delta R_{5\mu m}$.

tive network of filler particles can be formed. A possible explanation of why no piezoresistive effect is observed in the composites, could be that the mixing was insufficient for the complex conductive network to be formed.

6.2.3 Four-probe measurements

Measurements were also carried out using the four-probe electrode configuration from chapter 4, where a constant current, I, is driven through the resistor and the voltage drop, V, across is measured. Unfortunately, it was not possible for any of the composites to drive a current through the resistors and perform a measurement. Although the currents were in the nA range, the resistances were too high to drive the currents through the resistors.
From the design requirements of the four-point probe, the resistors have L/W-ratios of $6-50$. For the two-point probe configuration, the L/W-ratios are between $1.7 \cdot 10^{-3} - 0.17$, which is $1-4$ orders of magnitude lower. It means, that due to the high L/W-ratio of the resistor design in the four-point probe configuration, the probability that a silver aggregate is connecting the two ends of the resistor and conducting the current all the way through is very low.
Figure 6.9 shows SEM images of a 6% silver resistor, where the cluster formation is visible. If the resistor is long and narrow, the probability that there exists a conductive path through the resistor is very low.
Two tricks were tried to improve the conductivity of the samples:
(1) The composites were given a hardbake at 120°C for 90 minutes. This should evaporate solvent of the SU-8 and could thereby increase the conductivity by an order of magnitude [85], however it did not improve the measurements.
(2) It was suspected, that the connection between the resistor and the connector

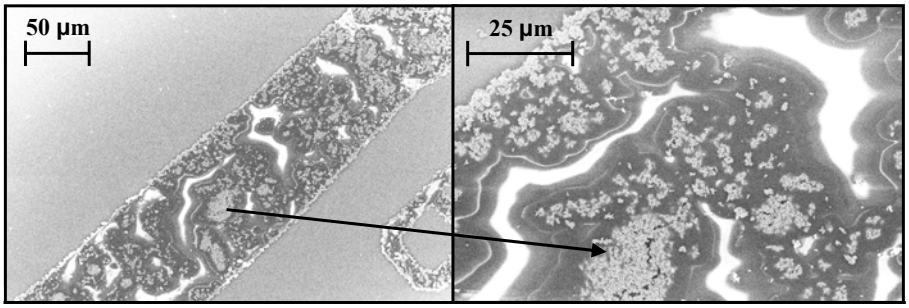

Figure 6.9: SEM micrograph of 6% composite. Silver aggregates are visible and there is no silver path through the resistor.

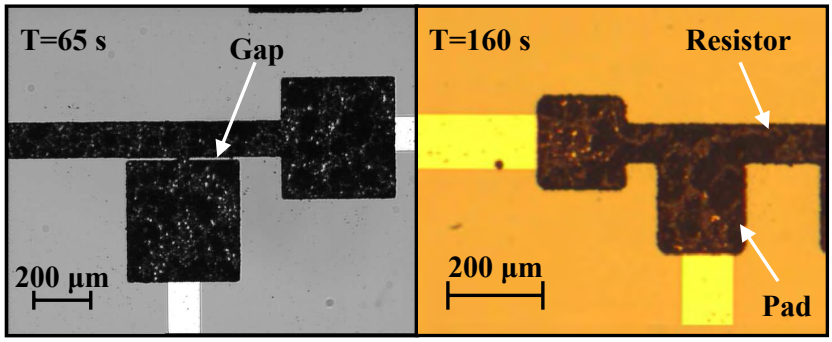

Figure 6.10: UV exposed structures of a 12% composite. LEFT: Optimized exposure dose - gap is present. RIGHT: Over-exposed structure. The gap has been closed.

pads was too bad, so the samples were over-exposed to completely crosslink the gap between the resistor and the connection pads. In figure 6.10, one can see that the gap has been eliminated in the over-exposed case, but it did not improve the measurements.

6.3 Silver SU-8 cantilevers

It is not easy to fabricate thin and straight SU-8 cantilevers. When the cantilevers become very thin ($\sim 2\ \mu$m), they will start to bend after being released from the wafer, due to internal stresses in the polymer [87].
A batch of cantilevers has been fabricated using the silver/SU-8 composite to investigate, whether the silver nanoparticles could lower the internal stress in the SU-8 and thereby produce more straight cantilevers.
A conductive polymer cantilever could also be of interest for conductive AFM

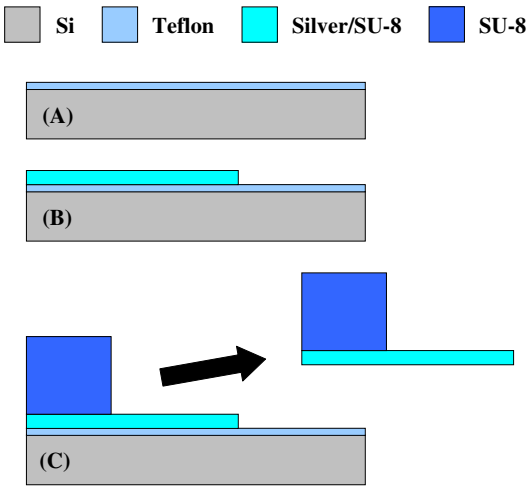

Figure 6.11: Process recipe for silver doped SU-8 cantilevers.

measurements.

6.3.1 Fabrication

A batch of cantilevers was fabricated using the 4% silver doped SU-8. The cantilevers were fabricated from the process sequence shown in figure 6.11:
(A): A teflon (C_4F_8) passivation layer is deposited in an advanced silicon etch (ASE). **(B):** 4% silver doped SU-8 is spin coated and the cantilever layer is defined by UV-lithography (thickness of 5-7 μm). **(C):** Support structure is defined and cantilevers are dry-released using a pair of tweezers. For process parameters, see appendix C.

The cantilevers were released using a dry-release method developed by PhD Stephan Keller [87]. Due to the low adhesion between teflon and SU-8, the cantilevers can be released by picking them off the wafer with a pair a tweezers. The dry-release method has been shown to work well for pure SU-8, however as can be seen from figure 6.12 the silver doped cantilevers broke in some cases during the dry-release. This could either be due to improved adhesion between silver doped SU-8 and teflon or because the SU-8 becomes more brittle, when the silver nanoparticles are added. The release yield was around 40%.
Figure 6.13 shows SEM images of cantilever arrays after the release. It is clear from the SEM images that there is a big difference in the status of the cantilevers after the dry-release; some cantilevers are broken, some are bending and some cantilevers are straight.
From the fabricated cantilevers it is hard to say something conclusive about the

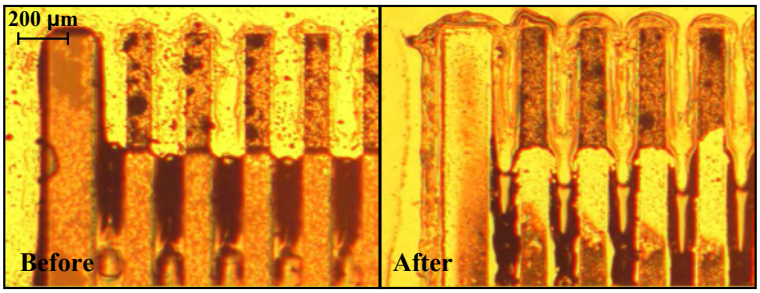

Figure 6.12: Optical image of a cantilever array (seen from above). LEFT: Cantilevers before the dry-release. RIGHT: Cantilevers after dry-release. It can be seen that the cantilevers are broken off at the support.

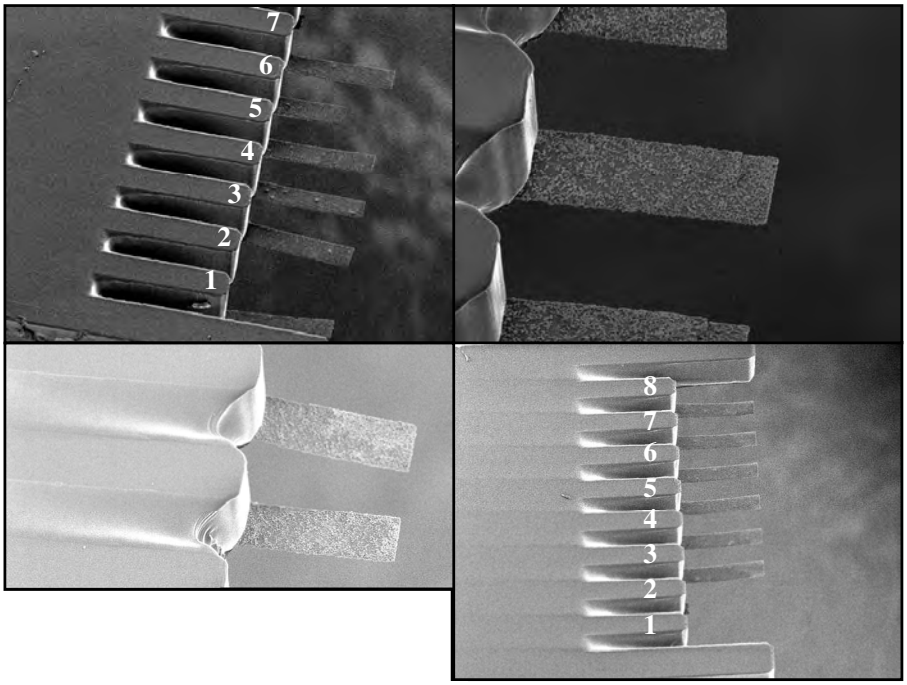

Figure 6.13: SEM images of 5-7 μm thick silver nanoparticle doped SU-8 cantilevers. UPPER-LEFT: Array of eight 500 μm long and 100 μm wide cantilevers. Cantilevers 2,6 and 8 are broken or partially broken during dry-release, cantilevers 1 and 3 are bending and cantilevers 4,5 and 7 are straight. UPPER-RIGHT: Silver aggregates are visible on the cantilever surface. LOWER-LEFT: Two 300 μm long and 100 μm wide cantilevers. The top cantilever is bending, while the lower cantilever is straight. LOWER-RIGHT: Array of eight 500 μm long and 100 μm wide cantilevers. Cantilevers 1 and 2 are broken off during the release and cantilevers 3-8 are bending slightly upwards.

effect of the silver nanoparticles on the internal stress of SU-8. A more thorough analysis is needed, where the bending of silver doped SU-8 cantilevers with different concentrations, is compared with the bending of pure SU-8 cantilevers.

6.4 Summary

Silver nanoparticle doped SU-8 composites with four different concentrations, (4, 6, 8 and 12%) have been investigated. Thin composite structures have been fabricated by UV lithography.
The resistivities of the fabricated thin films have been measured with both a two- and a four-probe technique. The resistivities are found to be highly dependent on the dimensions of the measured structures, due to aggregates in the composites. With a microscopic four-point probe from CAPRES A/S, the resistivity of a 12% composite film was measured and found to vary a factor of 30 within a 50×50 μm^2 square.
The silver composites were not found to have a significant piezoresistive effect. This might be due to an insufficient mixing of the composites, that does not create a complex conductive network.
A batch of 4% silver doped SU-8 cantilevers has been fabricated. The cantilevers were fabricated on a teflon coated silicon wafer, hence they can be dry-released by picking them off the wafer with a pair of tweezers. Whether or not the silver nanoparticles have an effect on the internal stress of the SU-8 cantilevers needs further investigation.

Chapter 7

Conductive polymers

To avoid the difficulties regarding mixing of conductive filler particles in a polymer matrix, this chapter investigates the intrinsically conductive polymer *polyaniline*. The idea is to find a polymeric materials that is piezoresistive by nature, such that no conductive filler particles need to be added.
Intrinsically conductive polymers have been used for many versatile purposes including microactuators [88], sensing of ammonia [89], sensing of ethanol, propanol and acetone [90], all-polymer micropumps [91], light-emitting-diodes (LEDs) [92] and all-polymer thin film transistors [93].
The chapter gives a general introduction to the basic characteristics of conductive polymers, with focus on polyaniline. It is described how polyaniline can be patterned and the structured polyaniline thin films are characterized with respect to the resistivity and piezoresistivity using both two- and four-probe chips.

7.1 Polyaniline

The Nobel prize in chemistry was in year 2000 given to Alan J. Heeger, Alan G. MacDiarmid and Hideki Shirakawa "for the discovery and development of conductive polymers" [94–96]. Intrinsically conductive polymers or "synthetic metals" is a class of materials, that have the electrical properties of metals or semiconductors, but have the mechanical properties and processing advantages of polymers.
In saturated polymers all of the electrons of the carbon atoms are used for covalent bonds, hence they are insulators. Conductive polymers are *conjugated* polymers, where the chemical bonding leads to one unpaired electron (the π-electron) per atom along the backbone. If the p_z orbitals of successive atoms along the backbone of the π-bonded system overlap, it will lead to electronic delocalization that

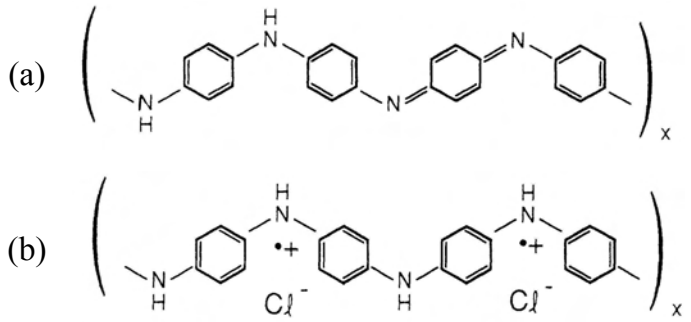

Figure 7.1: The chemical structure of different oxidation states of polyanine: (a) emeraldine base and (b) emeraldine salt. The insulating emeraldine base is doped with a protonic acid (HCl in this case) and the conductive emeraldine salt is formed. Charge neutrality is maintained by the counterion, Cl^-. Figure taken from [98].

provides a "highway" for charge mobility along the backbone of the polymer [94]. The energy difference between the highest occupied state in the π-band and the lowest unoccupied state in the π^*-band, is the π-π^* energy gap. The size of the energy gap can be controlled through chemical or electrochemical doping, which means that the conductivity of the polymers can be tailored.

There exists several conductive polymers, but in the present work polyaniline has been chosen since it is inexpensive, the polymerization is straightforward and proceeds with a high crosslinking yield and polyaniline has excellent stability.

Figure 7.1 shows the chemical structure of two different oxidation states of polyaniline - emeraldine base and emeraldine salt. Polyaniline is made conductive, when the emeraldine base is doped with a protonic acid and converted to emeraldine salt. The protonation introduces charge carriers into the electronic structure and combined with the delocalized electrons along the backbone, it makes polyaniline conductive. Through interchain hopping, the conductivity is extended into three dimensions [94]. The conductivity of polyaniline can be reversibly changed from insulator to conductor by adjusting the level of doping [95].

The present work has used polyaniline in the form of Panipol T manufactured by Panipol Oy, Finland [97]. Panipol T is green colored liquid, that consists of polyaniline salt (<15%) dissolved in toluene (>85%). The polyaniline salt has been made by doping the emeraldine base with dodecylbenzene sulfonic acid (DBSA).

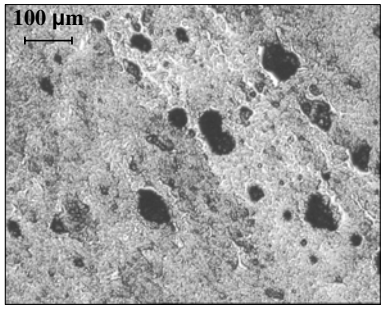

Figure 7.2: Optical image of a Panipol/SU-8 composite. Aggregates of up to 100 μm in diameter are observed.

7.2 Processing

Initially, it was tried to mix Panipol T and SU-8, as an easy why to obtain a conductive and UV sensitive composite. Panipol/SU-8 composites were mixed together in the relationship 0.5:3, 1:3 and 2:3. Even for the lowest Panipol T concentration, the composite was very viscous and had aggregates of up to 100 μm in diameter, see figure 7.2. It is believed, that due to the acidic nature of Panipol T, the crosslinking of SU-8 is kick-started, which then obscures the UV structuring, hence this approach was abandoned.

Polyaniline can be "patterned" by deep UV (254 nm) [99, 100]. When exposed to deep UV radiation, polyaniline is locally oxidized and (nearby) reduced (electron-hole pair creation and separation into free carriers) [94]. This can increase the sheet resistance by up to 11 orders of magnitude, hence you have an extremely high conductivity contrast between exposed and non-exposed areas [101]. Deep UV is not possible at the DTU Danchip cleanroom facility, so another method for structuring polyaniline was searched.

Conductive polymers can be structured in several ways including nanoimprinting [102], using oxygen plasma together with an etch mask [103], standard lift-off process [104] and using the hydrophilic nature of polyaniline and spin coat it on substrates previously patterned with hydrophilic and hydrophobic regions [105].

Figure 7.3 shows the two methods used for structuring polyaniline in this work: Plasma ashing with an etch mask and standard lift-off process. These two methods were chosen, since they are fast and compatible with standard cleanroom equipment.

Using the two methods, chips in both two- and four-probe electrode design were fabricated. The minimum feature size for the two designs is 5 and 15 μm, repsectively and this resolution was achievable with both patterning methods.

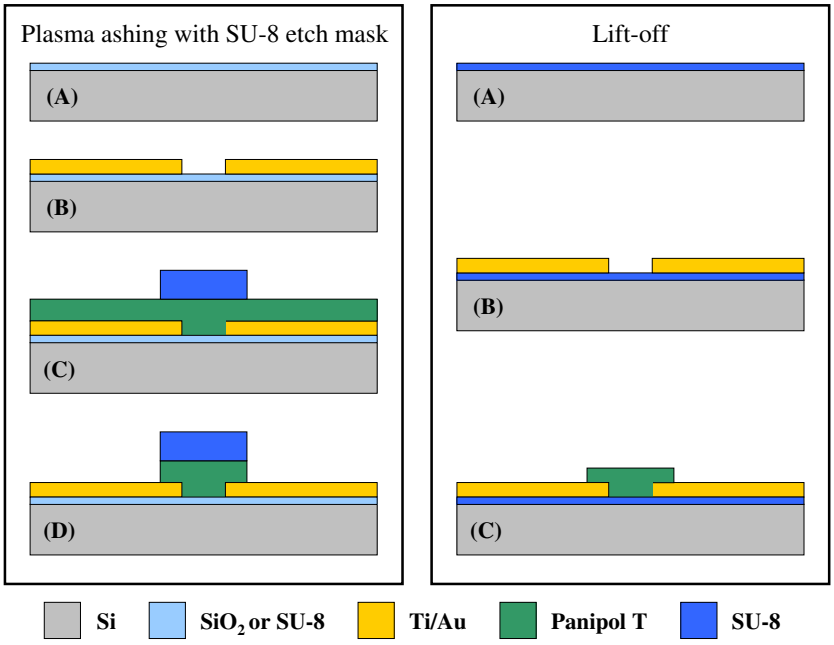

Figure 7.3: Schematics of the two different process sequences used for structuring polyaniline (not to scale). In both cases, the chips are released by dicing them out from the wafer. For process parameters, see appendix D.

7.2.1 Plasma ashing with SU-8 etch mask

The process sequence for plasma ashing with SU-8 as an etch mask is shown in figure 7.3 (left):
(A): 1500 Å thick SiO_2 layer is thermally grown or 1.5 μm SU-8 is spin coated on top of a 4" Si wafer for electrical insulation. (B): 50/2000 Å Ti/Au is e-beam evaporated on top of a patterned layer of AZ 5214E photoresist and electrodes are defined by a lift-off process. (C): Polyaniline is spin coated and baked and a 2 μm thick layer of SU-8 is UV-patterned on top. (D): Residual polyaniline is removed with an O_2/N_2 plasma using SU-8 as an etch mask.
When Panipol T was spin coated on SiO_2, a large acceleration was needed to have a nicely covered wafer.
The SU-8 etch mask is patterned on top of a polyaniline thin film and the residual polyaniline is removed by an $O_2 2/N_2$ plasma treatment. The etching with SU-8 as an etch mask, relies on the fact that crosslinked SU-8 is much more resistant to the plasma treatment than the polyaniline thin film, so polyaniline is removed and SU-8 stays. Another way to remove the residual polyaniline could be to use toluene, which is the solvent of polyaniline, but this has yet to be investigated.
In some cases, the SU-8 etch mask structures had cracks after the development

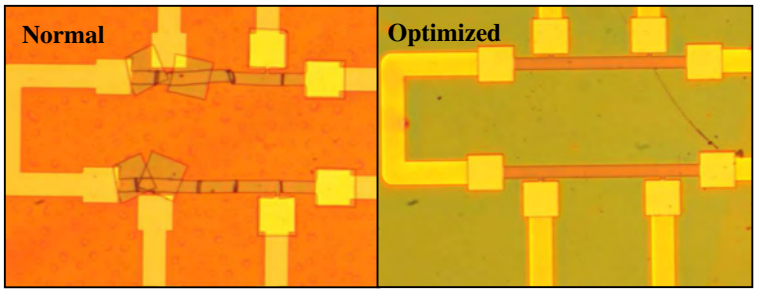

Figure 7.4: LEFT: Normal SU-8 recipe with cracks. RIGHT: Optimized SU-8 process without cracks.

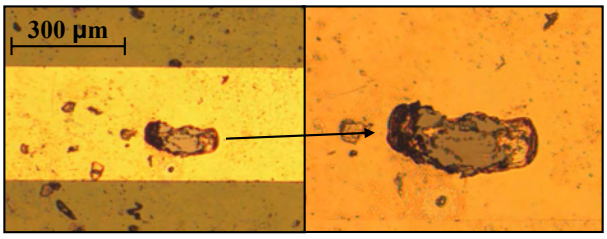

Figure 7.5: Optical image of a hole in the gold electrodes created by the ZIF-socket.

in PGMEA, hence the plasma treatment could not be used, see figure 7.4. This problem was resolved by using an optimized SU-8 process with longer baking times at lower temperatures, developed by S. Keller [87]. Figure 7.4 (right) shows the result for the optimized process with no cracks.

Both SiO_2 and SU-8 have been used as electrical insulation layer. When inserted in the ZIF-socket, it turned out, that the SU-8 substrate was sometimes too soft. As shown in figure 7.5, the contacts of the ZIF-socket in some cases penetrated the gold electrodes of the chip and went into the insulating SU-8 substrate, such that there was no electrical connection. This problem did not occur for all the batches.

In general, two-probe chips have been fabricated with SU-8 as an etch mask and SU-8 as the insulating layer and four-probe chips have been fabricated with SU-8 as an etch mask and SiO_2 as the insulating layer.

The last step in figure 7.3 (left) was carried out in a plasma asher. It was found that the etch rate was very unreproducible. In some cases a residual Panipol layer was wiped off the individual chips with a cleanroom tissue with acetone, just before measuring.

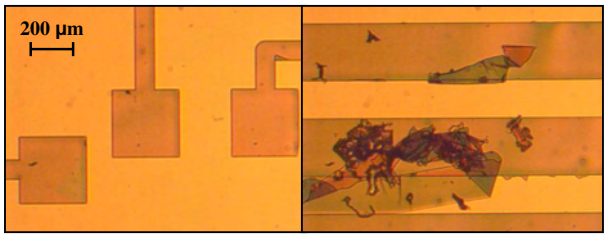

Figure 7.6: Optical images of polyaniline structures on an SU-8 substrate defined by lift-off in acetone. On the right hand side picture one can see how polyaniline is lifted off in pieces, showing that the polyaniline thin film was crosslinked.

7.2.2 Lift-off

The lift-off process is shown in figure 7.3 (right):
(A) A 1.5 μm thick layer of SU-8 is spin coated on top of a 4" wafer for electrical insulation. (B) 50/2000 Å Ti/Au is e-beam evaporated on top of a patterned layer of AZ 5214E photoresist and electrodes are defined by a lift-off process. (C) 300 nm thick layer of polyaniline is spin coated and baked on top of a patterned layer of AZ 5214E photoresist and defined by a lift-off process.
The lift-off was first attempted with SiO_2 as the electrical insulating substrate, but the polyaniline had low adhesion to SiO_2 and was removed during lift-off in acetone. Instead, SU-8 was used as the insulating substrate and it proved to have a good adhesion to polyaniline and the lift-off worked fine. From figure 7.6 (right) one can see that the polyaniline film is lifted off in pieces, which shows that the polyaniline film is crosslinked.

7.3 Measurements

To verify the composition of the spin coated polyaniline thin films, they were characterized by Fourier Transform Infrared Spectroscopy (FTIR). In FTIR, infrared radiation is passed through a sample. Some of the infrared radiation is absorbed by the sample and some of it is passed through (transmitted). The obtained spectrum gives a molecular fingerprint of the sample. The FTIR measurements were carried out at the Danish Polymer Centre DTU.
Figure 7.7 shows an FTIR spectrum of a thin film of Panipol T, spin coated on a silicon wafer. The main peaks have been identified as: 1561 and 1497 cm^{-1} (C=C stretching deformation of quinoid and benzenoid rings), 1300 cm^{-1} (C−N stretching of secondary aromatic amine), 1100 cm^{-1} (aromatic C−H in-plane bending) and 1031 cm^{-1} (absorption of a $-SO_3H$ group). The spectrum is similar to previ-

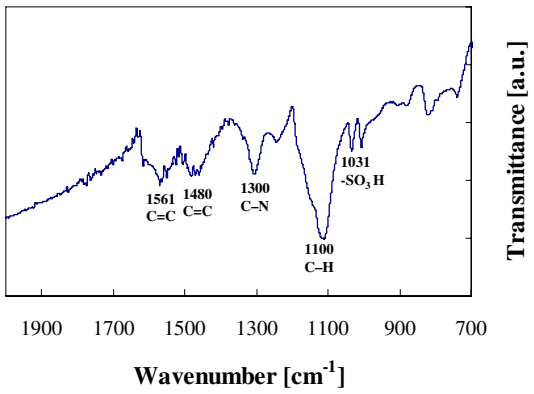

Figure 7.7: FTIR spectrum of a spin coated film of Panipol T. The spectrum shows the transmittance as a function of the inverse of the wavelength.

ously reported spectra on polyaniline [106, 107].

In the following, measurements of the fabricated chips in both two- and four-probe electrode configuration are described. All the measurements have been carried out at room temperature.

7.3.1 Two-probe measurements

Below is shown measurements for two chips from two different batches, batch 1 and 2. The process recipes are identical, except for the plasma asher time, which was doubled in batch 2.

Batch 1

Initially the contact resistance was estimated by plotting R as a function of the length L, see figure 7.8. The graph yields a straight line and the contact resistance is found as the crossing of the R-axis, which gives $R_{\text{contact}} = 88\ \Omega$. The contact resistance was found to be constant during straining of the chip.

For measuring the strain sensitivity of the polyaniline thin films, a measurement series was carried out, where a tensile strain of $\varepsilon = 1.1 \cdot 10^{-3}$ was applied to a 200 nm polyaniline thin film in a cyclic fashion, i.e. 120 s stress released, 120 s non-zero stress, 120 s stress released and so on. Two complete cycles were made. Figure 7.9 shows the measured two-probe resistance, R, as a function of time (the contact resistance has been subtracted from the R-values).

From the graph it is clear that the resistance *decreases*, when the tensile stress is applied. From the relation $\Delta R/R = K\varepsilon$, the gauge factors can be calculated with the values from figure 7.9. The gauge factors are found to $K_1 = -4.7$ and

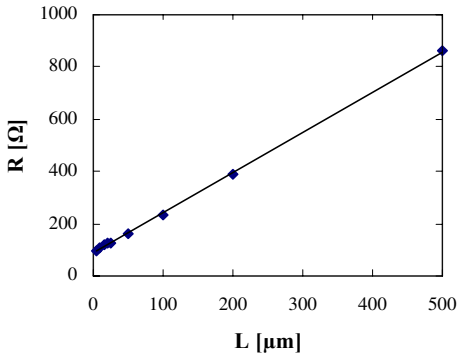

Figure 7.8: The resistance, R, as a function of the length, L, of the polyaniline thin film. The contact resistance can be found as the crossing of the R-axis.

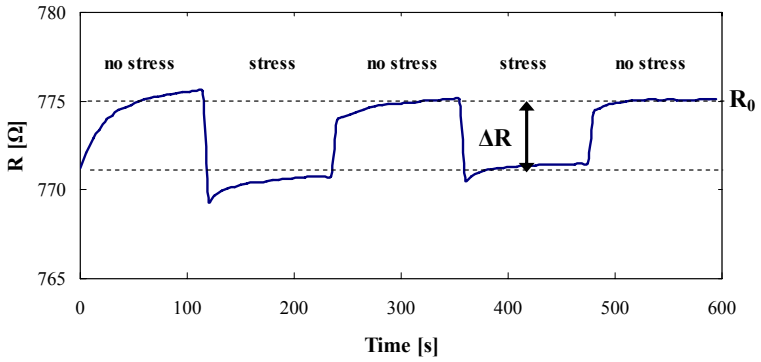

Figure 7.9: The two-probe resistance, R, as a function of time for a 200 nm polyaniline thin film. The length of the polyaniline film is L =500 μm.

$K_2 = -4.0$, for the 1st and 2nd cycle respectively, hence polyaniline has a *negative* gauge factor.

Batch 2

The contact resistance is again estimated by plotting R vs. L. Figure 7.10 shows a straight line and the contact resistance is found to $R_{\text{contact}} = 256\ \Omega$. The value was constant during straining of the chip.

Figure 7.11 plots R vs. t, for a measurement series similar to figure 7.9, but the cycle period was increased to 200 s and five cycles were made for a total of 36 minutes.

From figure 7.11 it is clear that the resistance decreases, when the tensile strain is applied, hence the strain response is again negative. For the five different cy-

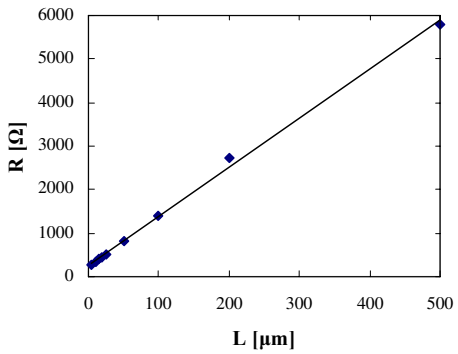

Figure 7.10: The resistance, R, as a function of the length, L, of the polyaniline thin film. The contact resistance can be found as the crossing of the R-axis.

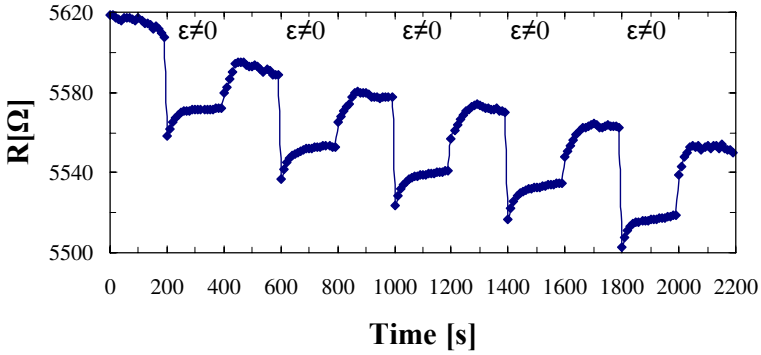

Figure 7.11: The two-probe resistance, R, as a function of time for a 200 nm polyaniline thin film. Tensile strain is applied in cyclic manner: 200 s no stress, 200 s non-zero stress, 200 s no stress and so on. The non-zero stress/strain periods are indicated.

cles gauge factors are found to be $K_{1-5} = -7.4, -6.7, -6.5, -6.4$ and -7.5, hence polyaniline has a negative gauge factor.
Some drift is seen in the measurement series in figure 7.11, but since the it is linear and as the gauge factor are calculated using mean values, the drift cancels out.

For the two series (figure 7.9 and 7.11), the resistivity was calculated for the nine different electrode spacings, L_{1-9}, using equation 5.2. Values were found to $\rho_1 = 0.85 - 1.2 \cdot 10^{-3}$ Ωm and $\rho_2 = 5.4 - 7.4 \cdot 10^{-3}$ Ωm, which agrees with the values supplied by the manufacturer [108]. The difference in the resistivities of the two batches may be due to uncertainties in the film thickness. Further experiments would include a more careful investigation of the polyaniline film thickness.

Figure 7.12 shows R vs. t for a measurement series similar to figure 5.12, where

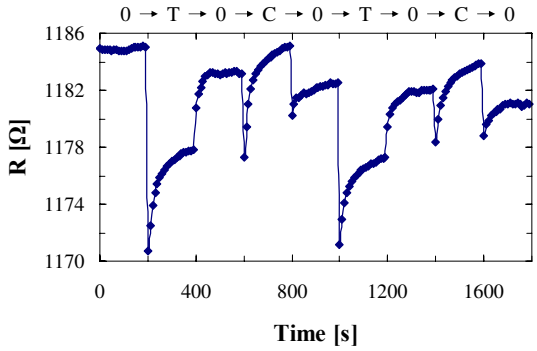

Figure 7.12: The two-probe resistance, R, as a function of time for a polyaniline thin film. 160 MPa tensile/compressive stress is applied alternately: 200 s no stres

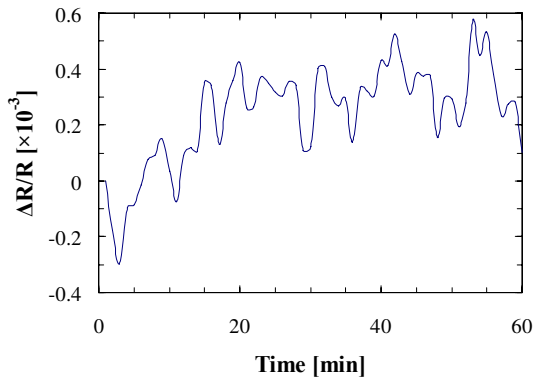

Figure 7.13: $\Delta R/R$ vs. t for a 1 hour drift measurement of a polyaniline thin film.

a tensile and compressive stress of 160 MPa is applied alternately to a chip from batch 1. The figure has 9 time intervals of 200 s: "0'" indicates periods of stress released, "T" indicates periods of non-zero tensile stress and "C" indicates periods of non-zero compressive stress.

As polyaniline has a negative gauge factor, one should expect R to *decrease* for 0→T and C→0 and *increase* for T→0 and 0→C. From the graph one can see that the behavior generally is as expected, except for the 0→C transition. When the compressive stress is applied, the resistance has a sharp initial drop, before it increases again. This behavior was observed in several measurements and is not yet understood.

The drift of a polyaniline thin film was measured in a series, where the two-probe resistance was measured once every minute for a total of 1 hour with no stress applied. Figure 7.13 shows $\Delta R/R$ as a function of time and by looking at figure 5.18 and 5.19, one can see that the fluctuations of the polyaniline thin film is of the same order as the highest doped carbon nanoparticle SU-8 composites.

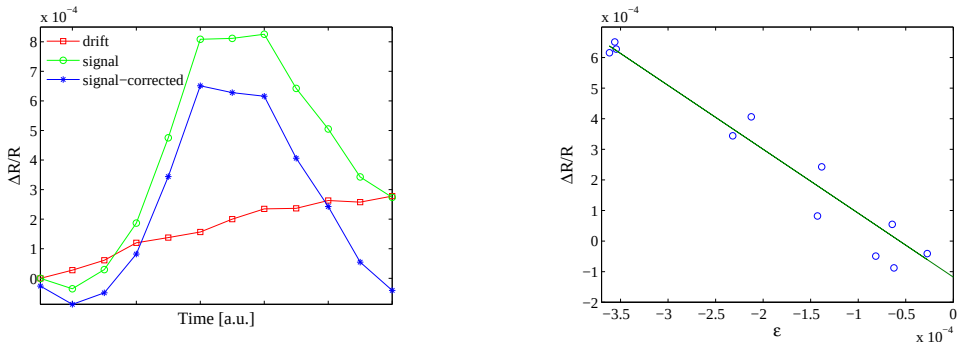

Figure 7.14: A 200 nm polyaniline film subjected to a compressive stress stepped from zero to 55 MPa and back to zero again. LEFT: $\Delta R/R$ as a function of time. The measured signal is shown along with the drift and the drift-corrected signal. The time-axis corresponds to 10 minutes. RIGHT: $\Delta R/R$ as a function of strain, ε. A straight line is fitted to the data and the gauge factor is found as the slope of the graph. A negative gauge factor of $K = -2.1$ is found.

7.3.2 Four-probe measurements

To eliminate the contact resistance, measurements were carried out with the four-probe electrode design explained in section 4.1.2. A constant current of $I = 100$ μA is passed through a 200 nm thick polyaniline film and the voltage drop across is measured, while a *compressive* stress is applied. In a period of 10 minutes, the stress is stepped from zero to 55 MPa and back to zero again in a total of 12 steps, using the microstepper described in section 4.2.1.
Figure 7.14 (left) shows $\Delta R/R$ as a function of time. When the stress is applied the relative resistance change goes up and it returns to its initial value, when the stress is released. As some drift was observed, the figure also shows the drift and the drift-corrected signal.
Figure 7.14 (right) shows $\Delta R/R$ as a function of the strain, ε. As the stress is compressive, $\varepsilon < 0$. A straight line is fitted to the data and as $\Delta R/R = K\varepsilon$ the gauge factor is found from the slope of the graph to $K = -2.1$.

In another series, a compressive stress is applied to a 200 nm thick polyaniline film. The stress is stepped from zero to 43 MPa and back to zero again. Three complete cycles are carried out over a period of 30 minutes. Figure 7.15 shows $\Delta R/R$ as a function of the strain, ε. For each of the three cycles a linear relationship is found. The gauge factors are found to $K_{1-3} = -2.1, -1.9$ and -1.8, hence the piezoresistive effect of polyaniline is negative and stable in time.

Several measurements series were carried out and gauge factors were found in the range $K = -2.9$ - -1.5 and resistivities were measured in the range $\rho =$

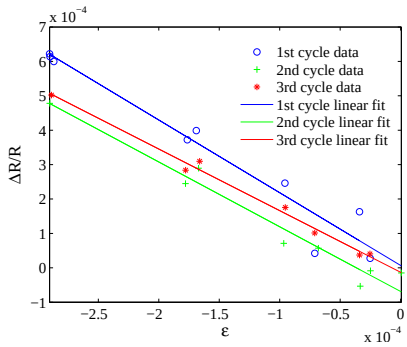

Figure 7.15: A 200 nm polyaniline film subjected to a compressive stress stepped from zero to 43 MPa and back to zero again. Three complete cycles are made. The figure shows $\Delta R/R$ as a function of ε. Gauge factors are calculated to $K_{1-3} = -2.1, -1.9$ and -1.8, respectively.

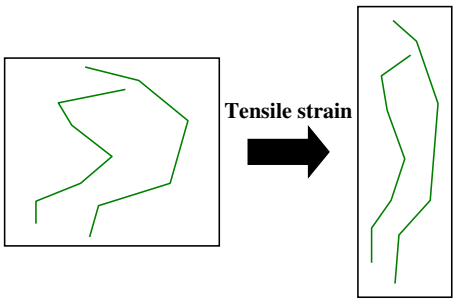

Figure 7.16: The illustration shows how two polyaniline chains are moved closer together, when a tensile strain is applied to the sample.

$0.24 - 0.3 \cdot 10^{-3}$ Ωm.

For both the two- and four-probe measurements, the gauge factors were found to be negative. It has previously been shown, that the conductivity of polyaniline increases up to four times, when subjected to large tensile strains (~400%), due to alignment of the polymer chains [98]. The effect of tensile straining, is to locally order the polymer chains, which increases interchain conduction and this increases the conductivity [109]. The same mechanism could explain the negative gauge factors of polyaniline. Although the polyaniline films are strained much less ($\sim 0.4 - 1‰$) the effect could be the same; when subjected to a tensile/compressive strain, the polymer chains are moved slightly closer together/further away, interchain conduction increases/decreases and this gives rise to a negative gauge factor (see figure 7.16).

The measured resistivities and gauge factors showed some differences. The measured values for the resistivity, were found to lie within a factor of 3-30. For the

gauge factors, the same qualitative behavior has been found in all the measurements; polyaniline has a negative gauge factor, but the size of the gauge factors was not constant.
Possible explanations to the observed differences could be uncertainties in the film thickness or differences in plasma asher time. Moreover, the four-probe chips have SiO_2 as substrate and the two-probe chips have SU-8. Furthermore, the four-probe chips were fabricated using a different bottle of Panipol T, than for the two-probe chips and it is possible, that there are some differences in the composition from bottle to bottle. The exact explanation of the differences has to be investigated in further measurements.

7.4 Summary

The intrinsically conductive polymer, polyaniline, has been investigated. Polyaniline thin films have been structured either by plasma ashing using an SU-8 etch mask or with a lift-off process. Two- and four-probe chips have been fabricated.
Resistivities have been measured to $\rho \sim 10^{-3}$ Ωm, which is in accordance with the values supplied by the manufacturer.
Gauge factors were measured and polyaniline was found to have a negative gauge factor and values were measured in the range $K = -7.5$ - -1.5. A possible explanation of the origin of the negative gauge factor of polyaniline was presented.

Chapter 8

Thin metal films

For very thin evaporated metal films, a percolative structure with metal islands will be formed [110]. As already shown by Neugebauer and Webb, the conduction in such a discontinuous metal film is dominated by electron tunneling between adjacent metal islands [111]. The tunnel current is exponentially decreasing with the distance between metal islands, d, hence a slight displacement of the islands by an external mechanical strain, will cause a large change in the tunnel current. Discontinuous metal films can thus be very strain sensitive and have large gauge factors.
This chapter describes the deposition of thin metal films and the characterization of their structure. Both the resistivity and the strain sensitivity has been measured for the deposited metal films.
The work presented in this chapter was carried out in collaboration with research assistant Martin Spieser.

8.1 Introduction

The conductivity of a metal film can be divided in four regions depending on the thickness, t, of the film [112]:
(a) *Thick films:* For t much greater than the electron mean free path, the film has essentially bulk properties.
(b): *Thin continuous films:* For a thickness of the order of one half to five times the electron mean free path, the conductivity becomes increasingly affected by surface- and grain boundary scattering, which reduces the conductivity.
(c) *Nearly discontinuous films:* For nearly discontinuous films, the conductivity is further limited by the dimension of the "bridges" connecting the metal islands.
(d) *Discontinuous films:* For a film consisting of small metal islands, the con-

ductivity is governed by electron tunneling between neighboring islands. Gauge factors will increase as the island size decreases and island separation increases. For discontinuous gold films, gauge factors exceeding the bulk values have been reported by several authors [112–115].
For Ag, Cu, Al and Au the electron mean free path at room temperature is 52, 39, 15 and 38 nm, respectively [116].
Whether or not island formation will take place during deposition of a metal film on a substrate will, besides chamber pressure and temperature and roughness of the substrate, depend on the interfacial energies of the involved materials. Assuming no kinetic constraints, the criterion for island formation is defined as

$$\gamma_{m/ox} > \gamma_{v/ox} - \gamma_{v/m} , \tag{8.1}$$

where $\gamma_{m/ox}$ is the metal-oxide interfacial free energy and $\gamma_{v/ox}$ and $\gamma_{v/m}$ is the surface free energy of the clean oxide and metal in vacuum, repscetively [117]. If criterion 8.1 is fulfilled, the metal does not wet the oxide/vacuum interface, but instead islands are formed with regions of clean oxide surface between.
By defining the adhesion energy as

$$E_{adh} = \gamma_{v/m} + \gamma_{v/ox} - \gamma_{m/ox} , \tag{8.2}$$

the criterion for island formation becomes

$$E_{adh} < 2\gamma_{v/m} . \tag{8.3}$$

As an example, gold on silicon dioxide has $E_{adh} = 227 - 246$ mJ/m^2. As $\gamma_{v/Au} = 1125$ mJ/m^2, criterion 8.3 is fulfilled, hence gold is expected to form islands when deposited on silicon dioxide [117].
The strain sensitivity of the discontinuous metal films comes from the exponentially decreasing tunnel current. Another way to exploit this effect, is to turn a scanning tunnel microscope (STM) into a strain sensor [118,119]. Electrodes with a spacing in the sub-nanometer range are defined and as they are displaced by an external strain, the tunnel current will change. However, even with e-beam lithography it is not trivial to fabricate electrodes with the required spacing/resolution, hence this method has not been investigated in this work.

8.2 Processing

For the fabrication of discontinuous metal films, two alternative methods were investigated:(a): E-beam evaporation of thin metal films and (b): E-beam evaporation of an alloy, followed by a selective chemical etch (figure 8.1) [120].

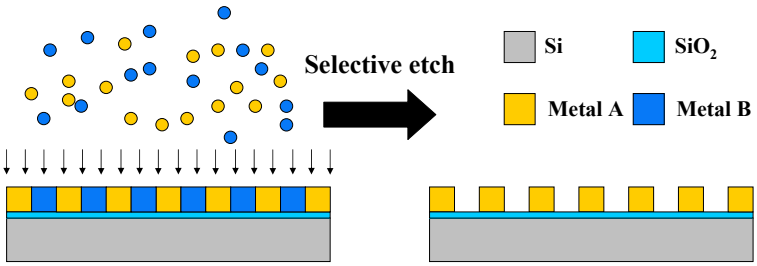

Figure 8.1: Schematics of selective etch to form a discontinuous metal film. LEFT: Deposition of an alloy consisting of metal A and B by e-beam evaporation. RIGHT: Selective etch of metal B resulting in a discontinuous metal film.

Initially, both methods were used to deposit thin films to find the best one. In both cases, the metals were e-beam evaporated at $2 \cdot 10^{-6}$ mbar with maximum substrate temperatures of 120°C, using an Alcatel SCM 600 E-beam metal deposition system.

8.2.1 Alloy deposition

It is not possible to simultaneously deposit metals from two different targets with the Alcatel e-beam evaporator, hence a special alloy target had to be made by melting two metals together. Several conditions have to be fulfilled, when choosing metals: (1) It should be possible to selectively etch one of the metals, (2) The metals should have comparable vapor pressures to insure uniformity of the deposited alloy and (3) As the alloy target was custom made, the metals should not be too expensive.
These requirements are met by an Al/Ag alloy. They have comparable vapor pressures, Al can be etched by NaOH and they are both affordable.
Figure 8.2 shows AFM and SEM images of a ~14 nm thick Al/Ag alloy thin film deposited on silicon. The bright spots of around 50 nm in diameter seen in the SEM image are probably Ag, since silver is around four times heavier than aluminum and heavier atoms gives higher brightness for backscattered electrons. The spots are also seen in the AFM image. The images suggest, that the uniformity of the deposited alloy is not good enough and that a subsequent NaOH etch would leave large isolated silver clusters on the wafer.
It is definitely possible to fabricate porous metal films using the above described method, however some optimization is needed. As the initial tests were not convincing and the method was time consuming (the special alloy target had to be inserted before every deposition by the assistance of a cleanroom technician,

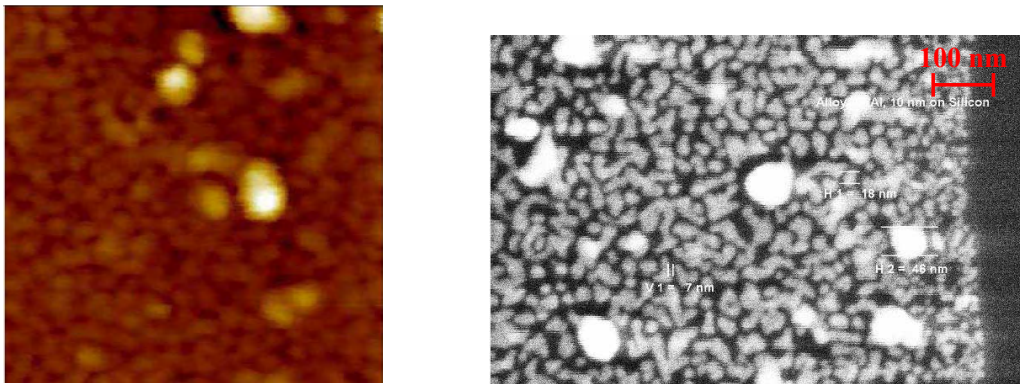

Figure 8.2: Images of a ~14 nm thick Al/Ag alloy film. LEFT: 500×500 nm^2 AFM image. RIGHT: SEM image. Bright silver spots of roughly 50 nm in diameter are observed.

whereas regular metals are always available) focus was put on depositing thin "mono" metal films by e-beam evaporation.

8.2.2 Thin gold film deposition

Test structures of e-beam evaporated gold films have been fabricated and their structure characterized. The thickness of the films were measured with an AFM. Figure 8.3 shows AFM and SEM images of a 6.5 and a 9.5 nm thick gold film deposited on silicon.
The SEM image of the 6.5 nm thick gold film (figure 8.3, top-right) shows round structures of ~10 nm in diameter with ~10 nm spacings. The round structures are also recognized in the AFM picture (figure 8.3, top-left), hence it suggests that we have a discontinuous metal film with island formation.
For the 9.5 nm thick gold film a meander structure is observed. In the SEM image (figure 8.3, bottom-right) a feature size of ~20 nm with ~5 nm trenches is observed. The structures are also found in the AFM picture (figure 8.3, bottom-left), hence the film resembles a nearly discontinuous film.
When depositing metal with the e-beam evaporator, a deposition rate and a target thickness is specified. For the 6.5 and 9.5 nm films, the rate was 1 Å/s (the lowest rate possible) and the target thickness 2 and 5 nm, respectively. The measured film thickness is thus greater than the target value however, if we have a discontinuous or nearly discontinuous metal film, this is also what one would expect; for a specific deposited metal volume, the metal is collected in 3D structures, that are thicker than a continuous film with the same metal volume.
Off course, there will also be an uncertainty in both the deposited and the mea-

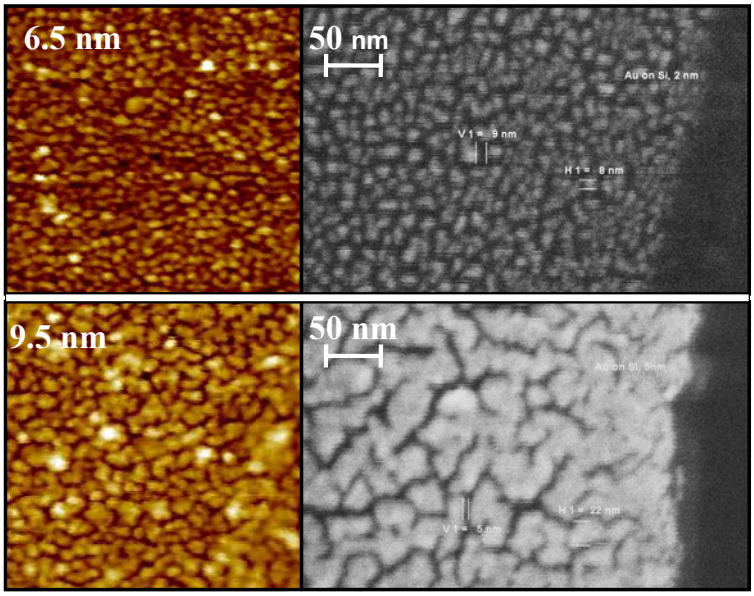

Figure 8.3: **TOP**: 6.5 nm Au on silicon. LEFT: AFM image (500 ×500 nm^2). RIGHT: SEM image. Metal islands of ~10 nm in diameter with ~10 spacings are observed.
BOTTOM: 9.5 nm Au on silicon. LEFT: 500 ×500 nm^2 AFM image. RIGHT: SEM image. A meander structure is observed. For improved resolution, the AFM images were taken with an SSS-NCH super sharp AFM tip from NanoWorld, with a cone angle less than 10° and a tip curvature radius of 2 nm [121].

sured thickness. However, looking at the AFM and SEM images it is believed, that the discrepancy between the target and measured thickness is due to island formation.

8.2.3 Chip fabrication

For measuring the resistivity and testing the strain sensitivity of the thin gold films, chips in the four-probe electrode design were fabricated. The fabrication process shown in figure 8.4 (left) is as follows: (A) 1500 Å SiO_2 is thermally grown on top of a 4" silicon wafer for electrical insulation, (B) Thin gold film is e-beam evaporated on top of a patterned layer of AZ 5214E photoresist and the resistor is defined by a lift-off process and (C) 50/200 nm thick Ti/Au layer is e-beam evaporated on top of a patterned layer of AZ 5214E photoresist and electrodes are defined by a lift-off process. For process parameters see appendix E.
When depositing a thin film on top of a thick film by e-beam evaporation, there

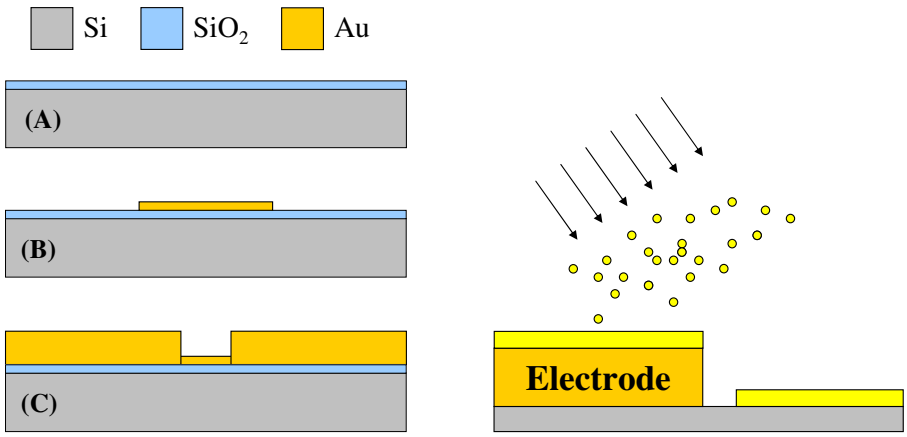

Figure 8.4: LEFT: Process sequence for the four-point probe thin films chips. RIGHT: The "shadowing" effect. The thick electrodes cast a shadow, hence when depositing a thin film on top, there is a risk that no electrical contact is established.

is a risk that you do not have electrical connection, if the angle of deposition is slightly tilted, due to the "shadowing" effect, shown schematically in figure 8.4 (right). For this reason, the thin gold film was deposited first and the thicker electrodes were deposited afterwards on top of the thin gold film.
For the thinnest deposited gold films, the alignment marks were hard to see. This was solved by initially depositing a thicker gold layer, using a silicon shadow wafer that covered the entire wafer, except the alignment marks (see figure 8.5).

Four-probe chips were fabricated and the thickness of the deposited gold was varied. Table 8.1 summarizes the target and measured thickness values and it is clear that the discrepancy between the two grows as you move towards thinner films.

Table 8.1: Gold film thickness - target and measured values.

Target [nm]	0.4	1.0	3.0	6.0	12.0	25.0
Measured [nm]	4.4	6.1	8.2	9.1	13.4	26.7

8.3 Measurements

With the fabricated four-probe chips, the resistivity and gauge factors have been measured for the thin metal films. All measurements were carried out at room

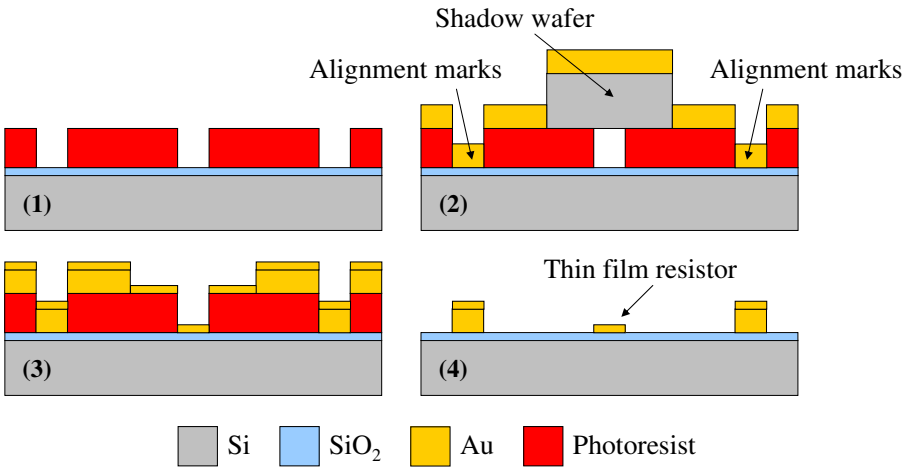

Figure 8.5: (1): Structured photoresist layer. (2): Thick gold layer is e-beam deposited using the shadow mask. (3): The shadow mask is removed and the thin gold film is e-beam deposited. (4): Lift-off in acetone.

temperature, where changes to the resistivity due to temperature changes are assumed to be small, compared to the measured signals.

8.3.1 Resistivity

The resistivity was measured with the four-probe chips by passing an $I = 500\,\mu$A current through the resistors and measuring the voltage drop V across. Through Ohm's law and equation 5.2, the resistivity can be calculated.
Figure 8.6 shows the measured resistivity, ρ, as a function of the film thickness, t. As expected, the resistivity increases, when the thickness of the film is decreased. The resistivity increases a factor of 3, when the thickness is decreased from 26.7 nm to 9.1 nm. The dashed line indicates the measured resistivity for a 250 nm thick (i.e. bulk) gold film and one can see, that the resistivity tends towards bulk resistivity, as the film thickness is increased.
For the 4.4, 6.1 and 8.2 nm thick gold films no measurements could be made. The resistance was too high for a current to be driven through. The high resistance could suggest, that these film had metal islands.

8.3.2 Piezoresistivity

The strain sensitivity was measured with the four-point bending fixture of chapter 4. The gold films were subjected to a compressive strain, which was stepped from zero to $\varepsilon \sim -5 \cdot 10^{-4}$ and back to zero again.

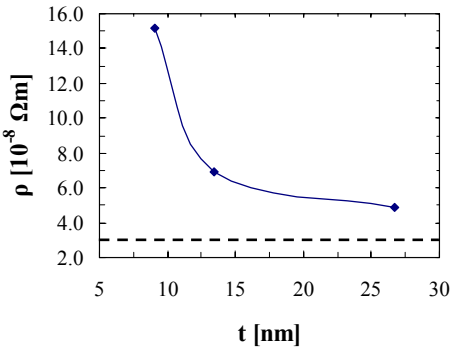

Figure 8.6: The resistivity, ρ, as a function of the gold film thickness, t.

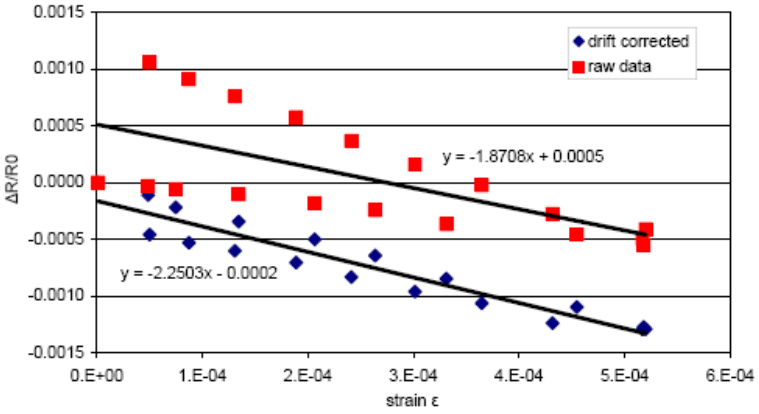

Figure 8.7: $\Delta R/R$ vs. ε for a 9.1 nm thick gold film. The graph shows both the raw and the drift corrected data. A straight line is fitted to the data points and a gauge factor of $K = 2.3$ is found.

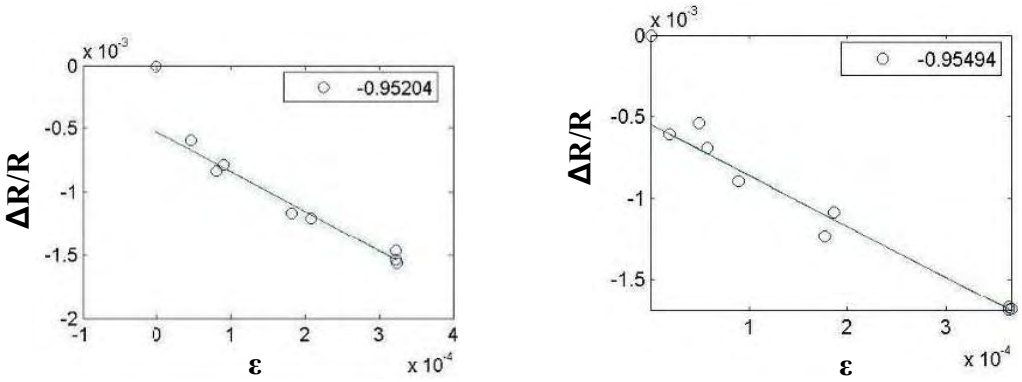

Figure 8.8: $\Delta R/R$ vs. ε. Note that the strain values are actually negative. LEFT: 13.4 nm thick gold film. $K = 3.1$. RIGHT: 26.7 nm thick gold film. $K = 3.1$.

Figure 8.7 shows $\Delta R/R$ as a function of the strain, ε, for the 9.1 nm thick gold film. As can be seen from the graph, there was some drift in the raw data. In the drift corrected data, the drift has been subtracted and the graph yields a straight line and the gauge factor K is found as the slope of the linear fit. As the applied stress is compressive, the strain is actually *negative*, hence the gauge is positive with a value of $K = 2.3$.

Figure 8.8 shows similar plots for the 13.4 and 26.7 nm thick gold films. Again, the drift has been subtracted and a linear relationship is found. The gauge factors are found as the slopes of the graphs, yielding $K = 3.1$ and $K = 3.1$ for the 13.4 and 26.7 nm film, respectively.

Measurements were carried out for several chips and table 8.2 summarizes the maximum measured gauge factors. The measured gauge factor for 250 nm (bulk) gold is also shown and one can see that the gauge factors have essentially the same value for all the different thicknesses.

A possible explanation to the measured values could be, that none of the metal films were discontinuous. Neuman and Sutton have shown, that it is only in the case of discontinuous films, that the gauge factors will differ significantly from the bulk values [112].

For the very thin films with islands, it was not possible to perform measurements, since the resistance was too high. The resistors in the four-probe design are long and narrow, hence if you have a high resistivity material, the resistances will be very large, making it very difficult to drive current through them.

Table 8.2: Maximum measured gauge factors of different gold films.

t [nm]	9.1	13.4	26.7	250
K	3.3	3.1	3.1	3.0

8.4 Summary

Thin gold films of varying thickness been fabricated by e-beam evaporation. The structure of the deposited thin films have been investigated by AFM and SEM and metal island formation was observed below a certain thickness. The resistivity was measured for the gold films using a four-probe electrode design and the resistivity was found to increases as the film thickness was decreased. Gauge factors were measured for the thickest of the thin gold films and the values were found to be essentially similar to the value for bulk gold. For the very thin gold films, the resistances were so high that neither the resistivity or the gauge factors could be measured.
The noise was not taken into consideration in these investigations. Although discontinuous metal films might offer large gauge factors, it is accompanied by an extremely high 1/f noise [34].

Chapter 9

Conclusions

The goal of this PhD thesis has been to investigate new piezoresistive polymer materials, with the aim of fabricating SU-8 polymer based cantilever sensors with piezoresistive readout, that are more sensitive than silicon based cantilevers.
Disregarding the noise, the sensitivity of a cantilever is proportional to the ratio K/E, where K is the gauge factor and E is Young's modulus. For an SU-8 based polymer cantilever, a gauge factor of $K \geq 4-5$ is needed to compete in sensitivity with silicon cantilever sensors.
Using a specially designed chip and a four-point bending fixture, gauge factors of four qualitatively different materials have been measured and candidates with $K \geq 4-5$ have been found.

Carbon nanoparticle doped SU-8 polymer composites have been fabricated, using three different types of carbon nanoparticles: XE2, CD975U and CD7051U. When the amount of carbon was increased, a clear insulator to conductor transition was observed, in agreement with percolation theory. The location of the percolation threshold seemed to be correlated with the structure of the carbon nanoparticles, such that higher structure gives lower percolation threshold.
For the low resistivity composites, stable and reversible gauge factors of $K \approx 5-10$ were measured, which makes them a valid material for the piezoresistive readout of polymer cantilever sensors. The high resistivity composites had gauge factors up to $K \approx 50$, but the measurements were much more noisy, than the low resistivity measurements. Whether or not the high resistivity composites can be used for the piezoresistive readout, relies on the ability to remove the noise.
Carbon doped SU-8 composites have been found, with stable gauge factors, that in principle should allow for the fabrication of polymer based cantilevers, that are more sensitive than silicon cantilevers. The next step, is to fabricate polymer cantilevers with carbon doped piezoresistive readout, characterize the signal-to-noise

ratio and compare it with silicon cantilevers.

Silver nanoparticle doped SU-8 composites are commercially available. Composites with 4, 6, 8 and 12% silver nanoparticles have been purchased. The resistivity of the composites showed to be highly dependent on the dimensions of the composite resistor, which suggests that the composites have clusters. This was also verified by optical- and SEM images and by a microscopic four-point probe measurement.
No significant piezoresistive effect was observed in the silver composites. This was attributed to insufficient mixing, which does not allow the formation of a complex conductive network. The investigated silver nanoparticle doped composites are thus not suited as a material for the piezoresistive readout of cantilevers.
A batch of silver doped SU-8 cantilevers were fabricated, which shows the possibility of fabricating conductive cantilevers. The silver nanoparticles might have an effect on the internal stress of the cantilevers, but it has to be investigated further.

The intrinsically conductive polymer, polyaniline, has been investigated. Two different methods for structuring polyaniline thin films (lift off and plasma ashing with an SU-8 etch mask), were explored. The polyaniline films had resistivities of the order of $\rho \sim 10^{-3}$ Ωm, which agrees with the values supplied from the manufacturer.
Polyaniline was found to have a negative gauge factor and values were measured in the range $K = -7.5 - -1.5$. The origin of the negative piezoresistive effect of polyaniline was explained by alignment of the polymer chains, which enhances intrachain conduction.
Some of the measured polyaniline thin films had gauge factors, which in principle should allow for the fabrication of polymer cantilevers, that are more sensitive than silicon cantilevers. As $K_{\text{piezo}_{\text{polyaniline}}} < 0$ and $K_{\text{geo}_{\text{polyaniline}}} > 0$, the two contributions work in opposite directions and this lowers the gauge factor of polyaniline. The next step would be to fabricate SU-8 cantilevers with polyaniline for the piezoresistive readout and do a signal-to-noise characterization.

As discontinuous metal films potentially can have very large gauge factors, the piezoresistive effect of thin gold films has been investigated. Gold films of varying thicknesses have been deposited by e-beam evaporation and characterized by AFM and SEM. For deposited film thicknesses below 10 nm, discontinuous and nearly discontinuous gold films were observed. Resistivities were measured for a 9.1, 13.1 and 26.7 nm thick gold film. All the measured resistivities were found to be larger than the bulk gold resistivity, with the highest resistivities for the thinnest films.

Gauge factors of the gold films were measured to $K \approx 3$, which is essentially the value for bulk gold. For the $t < 9.1$ nm thick gold films with metal islands, no measurements could be made, since the resistance in the films were too high to drive a current through them.
Even though discontinuous metal films can have very large gauge factors, they are also known to have a huge 1/f noise. Whether the large gauge factors are corrupted by the 1/f noise has to be investigated. (Furthermore, deposition of discontinuous gold films is not straightforward.)

In conclusion, carbon doped SU-8 polymer composites proved to be the most promising candidates for the piezoresistive readout of polymer based cantilever sensors. The composites are UV-structurable and have a stable and reversible piezoresistive effect. A drawback is that carbon doped SU-8 composites are not commercially available. Fabrication of the composites is time consuming and the reproducibility of the mixing procedure needs to be investigated.

Bibliography

[1] W. Haiss. Surface stress of clean and adsorbate-covered solids. *Reports on Progress in Physics*, 64(5):591–648, 2001.

[2] G. Binnig, C. F. Quate, and C. Gerber. Atomic force microscope. *Physical Review Letters*, 56(9):930–933, 1986.

[3] P. A. Rasmussen, J. Thaysen, S. Bouwstra, and A. Boisen. Modular design of afm probe with sputtered silicon tip. *Sensors and Actuators a-Physical*, 92(1-3):96–101, 2001.

[4] P. F. Indermuhle, G. Schurmann, G. A. Racine, and N. F. deRooij. Atomic force microscopy using cantilevers with integrated tips and piezoelectric layers for actuation and detection. *Journal of Micromechanics and Microengineering*, 7(3):218–220, 1997.

[5] D. R. Baselt, B. Fruhberger, E. Klaassen, S. Cemalovic, C. L. Britton, S. V. Patel, T. E. Mlsna, D. McCorkle, and B. Warmack. Design and performance of a microcantilever-based hydrogen sensor. *Sensors and Actuators B-Chemical*, 88(2):120–131, 2003.

[6] http://www3.physik.uni-greifswald.de/method/afm/AFM_laser.gif.

[7] J. Fritz, M. K. Baller, H. P. Lang, H. Rothuizen, P. Vettiger, E. Meyer, H. J. Guntherodt, C. Gerber, and J. K. Gimzewski. Translating biomolecular recognition into nanomechanics. *Science*, 288(5464):316–318, 2000.

[8] G. H. Wu, H. F. Ji, K. Hansen, T. Thundat, R. Datar, R. Cote, M. F. Hagan, A. K. Chakraborty, and A. Majumdar. Origin of nanomechanical cantilever motion generated from biomolecular interactions. *Proceedings of the National Academy of Sciences of the United States of America*, 98(4):1560–1564, 2001.

[9] N. V. Lavrik, M. J. Sepaniak, and P. G. Datskos. Cantilever transducers as a platform for chemical and biological sensors. *Review of Scientific Instruments*, 75(7):2229–2253, 2004. Times Cited: 111.

[10] Y. Arntz, J. D. Seelig, H. P. Lang, J. Zhang, P. Hunziker, J. P. Ramseyer, E. Meyer, M. Hegner, and C. Gerber. Label-free protein assay based on a nanomechanical cantilever array. *Nanotechnology*, 14(1):86–90, 2003. Times Cited: 76.

[11] M. Alvarez, A. Calle, J. Tamayo, L. M. Lechuga, A. Abad, and A. Montoya. Development of nanomechanical biosensors for detection of the pesticide ddt. *Biosensors & Bioelectronics*, 18(5-6):649–653, 2003. Times Cited: 42.

[12] L. A. Pinnaduwage, T. Thundat, A. Gehl, S. D. Wilson, D. L. Hedden, and R. T. Lareau. Desorption characteristics, of uncoated silicon microcantilever surfaces for explosive and common nonexplosive vapors. *Ultramicroscopy*, 100(3-4):211–216, 2004. Times Cited: 5.

[13] R. Berger, C. Gerber, J. K. Gimzewski, E. Meyer, and H. J. Guntherodt. Thermal analysis using a micromechanical calorimeter. *Applied Physics Letters*, 69(1):40–42, 1996.

[14] M. Li, H. X. Tang, and M. L. Roukes. Ultra-sensitive nems-based cantilevers for sensing, scanned probe and very high-frequency applications. *Nature Nanotechnology*, 2(2):114–120, 2007.

[15] E. Forsén. Nano-cantilevers fully integrated with cmos for ultrasenitive mass detection. *PhD thesis*, DTU Nanotech, Technical University of Denmark (DTU), 2005.

[16] R. Sandberg, A. Boisen, and W. Svendsen. Characterization system for resonant micro- and nanocantilevers. *Review of Scientific Instruments*, 76(12), 2005.

[17] E. Forsén, G. Abadal, S. Ghatnekar-Nilsson, J. Teva, J. Verd, R. Sandberg, W. Svendsen, F. Perez-Murano, J. Esteve, E. Figueras, F. Campabadal, L. Montelius, N. Barniol, and A. Boisen. Ultrasensitive mass sensor fully integrated with complementary metal-oxide-semiconductor circuitry. *Applied Physics Letters*, 87(4), 2005.

[18] S. Dohn, O. Hansen, and A. Boisen. Cantilever based mass sensor with hard contact readout. *Applied Physics Letters*, 88(26), 2006.

[19] A. Boisen, J. Thaysen, H. Jensenius, and O. Hansen. Environmental sensors based on micromachined cantilevers with integrated read-out. *Ultramicroscopy*, 82(1-4):11–16, 2000.

[20] P. A. Rasmussen, J. Thaysen, O. Hansen, S. C. Eriksen, and A. Boisen. Optimised cantilever biosensor with piezoresistive read-out. *Ultramicroscopy*, 97(1-4):371–376, 2003.

[21] A. Johansson, M. Calleja, P. A. Rasmussen, and A. Boisen. Su-8 cantilever sensor system with integrated readout. *Sensors and Actuators a-Physical*, 123-24:111–115, 2005.

[22] A. Johansson, G. Blagoi, and A. Boisen. Polymeric cantilever-based biosensors with integrated readout. *Applied Physics Letters*, 89(17), 2006.

[23] L. Flandin, T. Prasse, R. Schueler, K. Schulte, W. Bauhofer, and J. Y. Cavaille. Anomalous percolation transition in carbon-black-epoxy composite materials. *Physical Review B*, 59(22):14349–14355, 1999.

[24] L. Flandin, Y. Brechet, and J. Y. Cavaille. Electrically conductive polymer nanocomposites as deformation sensors. *Composites Science and Technology*, 61(6):895–901, 2001.

[25] M. Knite, V. Teteris, A. Kiploka, and J. Kaupuzs. Polyisoprene-carbon black nanocomposites as tensile strain and pressure sensor materials. *Sensors and Actuators a-Physical*, 110(1-3):142–149, 2004.

[26] A. B. Frazier and M. G. Allen. Piezoresistive graphite polyimide thin-films for micromachining applications. *Journal of Applied Physics*, 73(9):4428–4433, 1993.

[27] O. Hansen. Cantilever bending due to surface stress. *Internal note*, DTU Nanotech, Technical University of Denmark, 2001.

[28] S. D. Senturia. Microsystems design. *Kluwer Academic Publishers*, 2001.

[29] C. S. Smith. Piezoresistance effect in germanium and silicon. *Physical Review*, 94(1):42–49, 1954.

[30] Y. Kanda. Piezoresistance effect of silicon. *Sensors and Actuators a-Physical*, 28(2):83–91, 1991.

[31] J. Thaysen, A. D. Yalcinkaya, P. Vettiger, and A. Menon. Polymer-based stress sensor with integrated readout. *Journal of Physics D-Applied Physics*, 35(21):2698–2703, 2002. Times Cited: 25.

[32] J. Thaysen. Cantilever for bio-chemical sensing integrated in a microliquid handling system. *PhD thesis*, DTU Nanotech, Technical University of Denmark, 2001.

[33] http://memscyclopedia.org/su8.html.

[34] F. N. Hooge, T. G. M. Kleinpenning, and L. K. J. Vandamme. Experimental studies on 1-f noise. *Reports on Progress in Physics*, 44(5):479–532, 1981.

[35] C. Chiteme, D. S. McLachlan, and I. Balberg. 1/f or flicker noise in cellular percolation systems. *Physical Review B*, 67(2), 2003.

[36] A. J. Breeze, S. A. Carter, G. B. Alers, and M. B. Heaney. 1/f noise through the metal-nonmetal transition in percolating composites. *Applied Physics Letters*, 76(5):592–594, 2000.

[37] R. Strumpler and J. Glatz-Reichenbach. Conducting polymer composites. *Journal of Electroceramics*, 3(4):329–346, 1999.

[38] Kirkpatr.S. Percolation and conduction. *Reviews of Modern Physics*, 45(4):574–588, 1973.

[39] E. K. Sichel, J. I. Gittleman, and P. Sheng. Electrical-properties of carbon - polymer composites. *Journal of Electronic Materials*, 11(4):699–747, 1982.

[40] I. Balberg, D. Azulay, D. Toker, and O. Millo. Percolation and tunneling in composite materials. *International Journal of Modern Physics B*, 18(15):2091–2121, 2004.

[41] G. R. Ruschau, S. Yoshikawa, and R. E. Newnham. Resistivities of conductive composites. *Journal of Applied Physics*, 72(3):953–959, 1992.

[42] I. Balberg. Tunneling and nonuniversal conductivity in composite-materials. *Physical Review Letters*, 59(12):1305–1308, 1987.

[43] F. Carmona, F. Barreau, P. Delhaes, and R. Canet. An experimental-model for studying the effect of anisotropy on percolative conduction. *Journal De Physique Lettres*, 41(22):L531–L534, 1980.

[44] K. Miyasaka, K. Watanabe, E. Jojima, H. Aida, M. Sumita, and K. Ishikawa. Electrical-conductivity of carbon polymer composites as a function of carbon content. *Journal of Materials Science*, 17(6):1610–1616, 1982.

[45] I. Balberg. A comprehensive picture of the electrical phenomena in carbon black-polymer composites. *Carbon*, 40(2):139–143, 2002.

[46] J. Ravier, F. Houze, F. Carmona, O. Schneegans, and H. Saadaoui. Mesostructure of polymer/carbon black composites observed by conductive probe atomic force microscopy. *Carbon*, 39(2):314–318, 2001.

[47] F. Carmona and J. Ravier. Electrical properties and mesostructure of carbon black-filled polymers. *Carbon*, 40(2):151–156, 2002.

[48] F. Carmona and J. Ravier. To what extent is the structure of a random composite compatible with a percolation model? *Physica B-Condensed Matter*, 338(1-4):247–251, 2003.

[49] R. Viswanathan and M. B. Heaney. Direct imaging of the percolation network in a 3-dimensional disordered conductor-insulator composite. *Physical Review Letters*, 75(24):4433–4436, 1995.

[50] F. Carmona, R. Canet, and P. Delhaes. Piezoresistivity of heterogeneous solids. *Journal of Applied Physics*, 61(7):2550–2557, 1987.

[51] Private conversation, Ole Hansen, DTU Nanotech, DTU.

[52] http://www.comsol.com/.

[53] J. Richter. Piezo resistivity in silicon and strained silicon germanium. *M.Sc. thesis*, DTU Nanotech, Technical University of Denmark, 2004.

[54] J. Richter, O. Hansen, A. N. Larsen, J. L. Hansen, G. F. Eriksen, and E. V. Thomsen. Piezoresistance of silicon and strained si0.9ge0.1. *Sensors and Actuators a-Physical*, 123-24:388–396, 2005.

[55] M. B. Arnoldus. Determination of the piezoresistive properties of strained silicon. *M.Sc. thesis*, DTU Nanotech, Technical University of Denmark, 2006.

[56] L. Quercia, F. Loffredo, B. Alfano, V. La Ferrara, and G. Di Francia. Fabrication and characterization of carbon nanoparticles for polymer based vapor sensors. *Sensors and Actuators B-Chemical*, 100(1-2):22–28, 2004.

[57] L. Quercia, F. Loffredo, and G. Di Francia. Influence of filler dispersion on thin film composites sensing properties. *Sensors and Actuators B-Chemical*, 109(1):153–158, 2005.

[58] B. C. Sisk and N. S. Lewis. Vapor sensing using polymer/carbon black composites in the percolative conduction regime. *Langmuir*, 22(18):7928–7935, 2006.

[59] K. Y. Lee, N. LaBianca, S. A. Rishton, S. Zolgharnain, J. D. Gelorme, J. Shaw, and T. H. P. Chang. Micromachining applications of a high resolution ultrathick photoresist. *Journal of Vacuum Science & Technology B*, 13(6):3012–3016, 1995.

[60] J. El-Ali, I. R. Perch-Nielsen, C. R. Poulsen, D. D. Bang, P. Telleman, and A. Wolff. Simulation and experimental validation of a su-8 based pcr thermocycler chip with integrated heaters and temperature sensor. *Sensors and Actuators a-Physical*, 110(1-3):3–10, 2004.

[61] S. Balslev, A. Mironov, D. Nilsson, and A. Kristensen. Micro-fabricated single mode polymer dye laser. *Optics Express*, 14(6):2170–2177, 2006.

[62] Z. Wang, J. El-Ali, M. Engelund, T. Gotsaed, I. R. Perch-Nielsen, K. B. Mogensen, D. Snakenborg, J. P. Kutter, and A. Wolff. Measurements of scattered light on a microchip flow cytometer with integrated polymer based optical elements. *Lab on a Chip*, 4(4):372–377, 2004.

[63] M. Nordstrom, D. A. Zauner, A. Boisen, and J. Hubner. Single-mode waveguides with su-8 polymer core and cladding for moems applications. *Journal of Lightwave Technology*, 25(5):1284–1289, 2007.

[64] G. Voskerician, M. S. Shive, R. S. Shawgo, H. von Recum, J. M. Anderson, M. J. Cima, and R. Langer. Biocompatibility and biofouling of mems drug delivery devices. *Biomaterials*, 24(11):1959–1967, 2003.

[65] R. Schueler, J. Petermann, K. Schulte, and H. P. Wentzel. Agglomeration and electrical percolation behavior of carbon black dispersed in epoxy resin. *Journal of Applied Polymer Science*, 63(13):1741–1746, 1997.

[66] F. M. Du, J. E. Fischer, and K. I. Winey. Coagulation method for preparing single-walled carbon nanotube/poly(methyl methacrylate) composites and their modulus, electrical conductivity, and thermal stability. *Journal of Polymer Science Part B-Polymer Physics*, 41(24):3333–3338, 2003.

[67] L. Gammelgaard. Polymer cantilever with integrated readout. *M.Sc. thesis*, DTU Nanotech, Technical University of Denmark, 2004.

[68] http://www.microchem.com/.

[69] A. Katada, Y. F. Buys, Y. Tominaga, S. Asai, and M. Sumita. Resistivity control in the semiconductive region for carbon-black-filled polymer composites. *Colloid and Polymer Science*, 283(4):367–374, 2005.

[70] S. W. Bigger and O. Delatycki. The effects of pigments on the photostability of polyethylene. *Journal of Materials Science*, 24(6):1946–1952, 1989.

[71] M. B. Heaney. Resistance-expansion-temperature behavior of a disordered conductor-insulator composite. *Applied Physics Letters*, 69(17):2602–2604, 1996.

[72] Z. Rubin, S. A. Sunshine, M. B. Heaney, I. Bloom, and I. Balberg. Critical behavior of the electrical transport properties in a tunneling-percolation system. *Physical Review B*, 59(19):12196–12199, 1999.

[73] M. Knite, V. Teteris, B. Polyakov, and D. Erts. Electric and elastic properties of conductive polymeric nanocomposites on macro- and nanoscales. *Materials Science & Engineering C-Biomimetic and Supramolecular Systems*, 19(1-2):15–19, 2002. Sp. Iss. SI.

[74] M. Knite, V. Teteris, A. Kiploka, and I. Klemenoks. Reversible tenso-resistance and piezo-resistance effects in conductive polymer-carbon nanocomposites. *Advanced Engineering Materials*, 6(9):742–746, 2004.

[75] J. N. Aneli, G. E. Zaikov, and L. M. Khananashvili. Effects of mechanical deformations on the structurization and electric conductivity of electric conducting polymer composites. *Journal of Applied Polymer Science*, 74(3):601–621, 1999.

[76] L. Flandin, A. Chang, S. Nazarenko, A. Hiltner, and E. Baer. Effect of strain on the properties of an ethylene-octene elastomer with conductive carbon fillers. *Journal of Applied Polymer Science*, 76(6):894–905, 2000.

[77] L. Flandin, A. Hiltner, and E. Baer. Interrelationships between electrical and mechanical properties of a carbon black-filled ethylene-octene elastomer. *Polymer*, 42(2):827–838, 2001.

[78] E. K. Sichel, J. I. Gittleman, and P. Sheng. Transport properties of the composite-material carbon-poly(vinyl chloride). *Physical Review B*, 18(10):5712–5716, 1978.

[79] L. X. Shen, J. Li, B. M. Liaw, F. Delale, and J. H. Chung. Modeling and analysis of the electrical resistance measurement of carbon fiber polymer-matrix composites. *Composites Science and Technology*, 67(11-12):2513–2520, 2007.

[80] Y. H. Hou, M. Q. Zhang, and M. Z. Rong. Performance stabilization of conductive polymer composites. *Journal of Applied Polymer Science*, 89(9):2438–2445, 2003.

[81] X. W. Zhang, Y. Pan, Q. Zheng, and X. S. Yi. Time dependence of piezoresistance for the conductor-filled polymer composites. *Journal of Polymer Science Part B-Polymer Physics*, 38(21):2739–2749, 2000.

[82] X. W. Zhang, Y. Pan, Q. Zheng, and X. S. Yi. Piezoresistance of conductor filled insulator composites. *Polymer International*, 50(2):229–236, 2001.

[83] http://www.gersteltec.ch/.

[84] S. Jiguet, A. Bertsch, H. Hofmann, and P. Renaud. Su8-silver photosensitive nanocomposite. *Advanced Engineering Materials*, 6(9):719–724, 2004.

[85] S. Jiguet, A. Bertsch, H. Hofmann, and P. Renaud. Conductive su8 photoresist for microfabrication. *Advanced Functional Materials*, 15(9):1511–1516, 2005.

[86] http://www.capres.com.

[87] Stephan Keller. *PhD thesis*, DTU Nanotech, Technical University of Denmark, 2008.

[88] E. Smela. Microfabrication of ppy microactuators and other conjugated polymer devices. *Journal of Micromechanics and Microengineering*, 9(1):1–18, 1999.

[89] Y. S. Lee, K. D. Song, J. S. Huh, W. Y. Chung, and D. D. Lee. Fabrication of clinical gas sensor using mems process. *Sensors and Actuators B-Chemical*, 108(1-2):292–297, 2005.

[90] P. C. Lekha, E. Subramanian, and D. P. Padiyan. Electrodeposition of polyaniline thin films doped with dodeca tungstophosphoric acid: Effect on annealing and vapor sensing. *Sensors and Actuators B-Chemical*, 122(1):274–281, 2007.

[91] T. S. Hansen, K. West, O. Hassager, and N. B. Larsen. An all-polymer micropump based on the conductive polymer poly(3,4-ethylenedioxythiophene) and a polyurethane channel system. *Journal of Micromechanics and Microengineering*, 17:860–866, 2007.

[92] T. Granlund, T. Nyberg, L. S. Roman, M. Svensson, and O. Inganas. Patterning of polymer light-emitting diodes with soft lithography. *Advanced Materials*, 12(4):269–273, 2000.

[93] M. Halik, H. Klauk, U. Zschieschang, T. Kriem, G. Schmid, W. Radlik, and K. Wussow. Fully patterned all-organic thin film transistors. *Applied Physics Letters*, 81(2):289–291, 2002.

[94] A. J. Heeger. Nobel lecture: Semiconducting and metallic polymers: The fourth generation of polymeric materials. *Reviews of Modern Physics*, 73(3):681–700, 2001.

[95] A. G. MacDiarmid. Nobel lecture: "synthetic metals": A novel role for organic polymers. *Reviews of Modern Physics*, 73(3):701–712, 2001.

[96] H. Shirakawa. Nobel lecture: The discovery of polyacetylene film - the dawning of an era of conducting polymers. *Reviews of Modern Physics*, 73(3):713–718, 2001.

[97] http://www.panipol.com/.

[98] R. P. McCall, E. M. Scherr, A. G. Macdiarmid, and A. J. Epstein. Anisotropic optical-properties of an oriented-emeraldine-base polymer and an emeraldine-hydrochloride-salt polymer. *Physical Review B*, 50(8):5094–5100, 1994.

[99] F. J. Touwslager, N. P. Willard, and D. M. de Leeuw. I-line lithography of poly-(3,4-ethylenedioxythiophene) electrodes and application in all-polymer integrated circuits. *Applied Physics Letters*, 81(24):4556–4558, 2002.

[100] F. J. Touwslager, N. P. Willard, and D. M. de Leeuw. Water based i-line projection lithography of pedot. *Synthetic Metals*, 135(1-3):53–54, 2003. Part 1 Sp. Iss. SI.

[101] C. J. Drury, C. M. J. Mutsaers, C. M. Hart, M. Matters, and D. M. de Leeuw. Low-cost all-polymer integrated circuits. *Applied Physics Letters*, 73(1):108–110, 1998.

[102] T. Makela, T. Haatainen, J. Ahopeito, and H. Isotalo. Imprinted electrically conductive patterns from a polyaniline blend. *Journal of Vacuum Science & Technology B*, 19(2):487–489, 2001.

[103] D. Chinn and J. Janata. Spin-cast thin-films of polyaniline. *Thin Solid Films*, 252(2):145–151, 1994.

[104] J. R. Chan, X. Q. Huang, and A. M. Song. Nondestructive photolithography of conducting polymer structures. *Journal of Applied Physics*, 99(2), 2006.

[105] K. S. Lee, G. B. Blanchet, F. Gao, and Y. L. Loo. Direct patterning of conductive water-soluble polyaniline for thin-film organic electronics. *Applied Physics Letters*, 86(7), 2005.

[106] L. J. Zhang and M. X. Wan. Synthesis and characterization of self-assembled polyaniline nanotubes doped with d-10-camphorsulfonic acid. *Nanotechnology*, 13(6):750–755, 2002.

[107] G. A. Rimbu, I. Stamatin, C. L. Jackson, and K. Scott. The morphology control of polyaniline as conducting polymer in fuel cell technology. *Journal of Optoelectronics and Advanced Materials*, 8(2):670–674, 2006.

[108] Private comminication with Paninol Oy, Finland.

[109] Z. H. Wang, E. M. Scherr, A. G. Macdiarmid, and A. J. Epstein. Transport and epr studies of polyaniline - a quasi-one-dimensional conductor with 3-dimensional metallic states. *Physical Review B*, 45(8):4190–4202, 1992.

[110] P. Smilauer. Thin metal-films and percolation theory. *Contemporary Physics*, 32(2):89–102, 1991.

[111] C. A. Neugebauer and M. B. Webb. Electrical conduction mechanism in ultrathin, evaporated metal films. *Journal of Applied Physics*, 33(1):74–, 1962.

[112] M. R. Neuman and W. G. Sutton. Structural dependence of strain gauge effect and surface resistivity for thin gold films. *Journal of Vacuum Science & Technology*, 6(4):710–, 1969.

[113] R. L. Parker and A. Krinsky. Electrical resistance-strain characteristics of thin evaporated metal films. *Journal of Applied Physics*, 34(9):2700–, 1963.

[114] B. Hok, R. Nyholm, O. Groth, and P. A. Tove. Study of discontinuous au films with respect to strain gauge applications. *Thin Solid Films*, 17(1):113–121, 1973.

[115] C. S. Li, P. J. Hesketh, and G. J. Maclay. Thin gold film strain-gauges. *Journal of Vacuum Science & Technology a-Vacuum Surfaces and Films*, 12(3):813–819, 1994.

[116] W. Zhang, S. H. Brongersma, O. Richard, B. Brijs, R. Palmans, L. Froyen, and K. Maex. Influence of the electron mean free path on the resistivity of thin metal films. *Microelectronic Engineering*, 76(1-4):146–152, 2004.

[117] C. T. Campbell. Ultrathin metal films and particles on oxide surfaces: Structural, electronic and chemisorptive properties. *Surface Science Reports*, 27(1-3):1–111, 1997.

[118] T. W. Kenny, W. J. Kaiser, J. A. Podosek, H. K. Rockstad, J. K. Reynolds, and E. C. Vote. Micromachined tunneling displacement transducers for physical sensors. *Journal of Vacuum Science & Technology a-Vacuum Surfaces and Films*, 11(4):797–802, 1993. Part 1.

[119] D. DiLella, L. J. Whitman, R. J. Colton, T. W. Kenny, W. J. Kaiser, E. C. Vote, J. A. Podosek, and L. M. Miller. A micromachined magnetic-field sensor based on an electron tunneling displacement transducer. *Sensors and Actuators a-Physical*, 86(1-2):8–20, 2000.

[120] M. C. Dixon, T. A. Daniel, M. Hieda, D. M. Smilgies, M. H. W. Chan, and D. L. Allara. Preparation, structure, and optical properties of nanoporous gold thin films. *Langmuir*, 23(5):2414–2422, 2007.

[121] http://www.nanoworld.com/.

Appendix A

Carbon chip process recipe

1. Deposition of oxide: 1500 Å SiO_2, bor drive-in, DRY1150, t=70 min.
2. Resist adhesion promoter: HMDS, recipe 4.
3. Spin resist: Track1, PR1_5, AZ5214E.
4. UV-exposure: KS-Aligner, hard contact, t=9 s, mask="gold wiring".
5. Develop: 70 s in NaOH:H_20 (1:5), rinse in DI water.
6. Metal evaporation: Alcatel, Ti/Au 50/3000 Å.
7. Lift-off: Acetone with ultrasound. Rinse with DI water.
8. Spin coat carbon composite: Manual spinner, 4000 rpm, low acceleration, t=40 s.
9. Pre-bake: Hotplate, 1 min. at 60°C, 1 min. at 90°C with 3 min. ramp.
10. UV-exposure: KS-aligner, hard contact, t=170 s, mask="composite".
11. Post exposure bake: Hotplate, 1 min. at 60°C, 1 min. at 90°C with 3 min. ramp.
12. Develop: PGMEA, 3 min. in FIRST and 3 min. in FINAL. Rinse with isopropanol.
13. Cleaning: Dip wafers in ultrasound water bath (2-3 s).
14. Release chips: Automatic dicing saw.

Appendix B

Silver chip process recipe

1. Deposition of oxide: 1500 Å SiO_2, bor drive-in, DRY1150, t=70 min.
2. Resist adhesion promoter: HMDS, recipe 4.
3. Spin resist: Track1, PR1_5, AZ5214E.
4. UV-exposure: KS-Aligner, hard contact, t=9 s, mask="new_4pp_electrodes".
5. Develop: 60 s in NaOH:H_20 (1:5), rinse in DI water.
6. Metal evaporation: Alcatel, Ti/Au 50/2500 Å.
7. Lift-off: Acetone with ultrasound. Rinse with DI water.
8. Cleaning: Plasma asher, O2/N2, 240/40 at 400 W for t= 2 min.
9. Spin coat silever composite: Manual spinner, 6000 rpm, low acceleration, t=40 s.
10. Pre-bake: Hotplate, 5 min. at 65°C, 30 min. at 95°C with 2°C/min ramp.
11. UV-exposure: KS-aligner, hard contact, t=55 s (4, 6 and 8%), t=70 s (12%), mask="new_4pp_resistor".
12. Post exposure bake: Hotplate, 5 min. at 65°C, 30 min. at 95°C with 2°C/min ramp.
13. Develop: PGMEA, 3 min. in FIRST and 3 min. in FINAL. Rinse with isopropanol.
14. Cleaning: Dip wafers in ultrasound water bath (2-3 s).
15. Release chips: Automatic dicing saw.

Appendix C

Silver/SU-8 cantilever process recipe

1. C_4F_8-passivation: ASE, wettef2, 120 sccm, 300 W, 0 W, 60 mTorr, 60 s
2. Spin coat 4% silver composite: Manual spinner, 6000 rpm, 40 s, maximum acceleration.
3. Solvent evaporation: Wait 30 min. before further processing.
4. UV-exposure: KS-aligner, hard contact, 500 mJ/cm^2, mask="IBM_cantilever".
5. Post exposure bake: Hotplate, 1 hour at 50°C with 2°C/min ramp.
6. Develop: PGMEA, 2 min. in FIRST, 2 min. in FINAL. Rinse with IPA. Air dry.
7. UV-exposure: KS-aligner, flood exposure, 2×500 mJ/cm^2.
8. Post exposure bake: Hotplate, 1 hour at 50°C with 2°C/min ramp.
9. Spin coat SU-8 2075: KS-spinner, 300 rpm, 30 s, 100 rpm/s; 600 rpm, 60 s, 100 rpm/s. SU-8 2075, 7 s, 42 psi.
10. Soft bake: Hotplate, 15 min at 60°C with 10°C/min ramp, 105 min. at 90°C with 10°C/min ramp.
11. UV-exposure: KS-aligner, proximity mode, 6×450 mJ/cm^2, mask="IBM_bodychip".
12. Post-exposure bake: Hotplate, 15 min at 60°C with 10°C/min ramp, 45 min. at 90°C with 10°C/min ramp.
13. Develop: PGMEA, 15 min. in FIRST, 15 min. in FINAL. Rinse with IPA. Air dry.
14. Release: Pick cantilevers gently off the silicon wafer with a pair of tweezers.

Appendix D

Polyaniline chip process recipe

Two-probe chips

1. Spin coat SU-8: KS-spinner, ske_thin_SU-8, SU-8 2002.
2. Pre-bake: Hotplate, 1 min. at 60°C, 1 min. at 90°C, with 3 min. ramp.
3. UV-exposure: KS-aligner, flood exposure, t=50 s.
4. Post exposure bake: Hotplate, 1 min. at 60°C, 1 min. at 90°C, with 3 min. ramp.
5. Spin resist: Track1, pr1_5, AZ5214E.
6. UV-exposure: KS-aligner, hard contact, mask="gold wiring", t=9 s.
7. Develop: 70 s in NaOH:H_2O (1:5), rinse with DI water.
8. Metal deposition: Alcatel, Ti/Au, 50/1500 Å.
9. Lift-off: Acetone and ultrasound. Rinse with DI-water.
10. Spin coat polyaniline: Manual spinner, 4000 rpm, max. acceleration, 40 s, Panipol T.
11. Bake: Hotplate, 1 min. at 90°C with 5 min. ramp.
12. Spin coat SU-8: KS-spinner, ske_thin_SU-8, SU-8 2002.
13. Pre-bake: Hotplate, 1 min. at 60°C, 1 min. at 90°C, with 3 min. ramp.
14. UV-exposure: KS-aligner, hard contact, mask="resistor", t=50 s.
15. Post exposure bake: Hotplate, 1 min. at 60°C, 1 min. at 90°C, with 3 min. ramp.
15. Develop: PGMEA, 3 min. in FIRST, 3 min. in FINAL. Rinse with IPA.
16. Remove residual polyaniline: Plasma asher. Batch 1: O2/N2, 250/50 ml/min. t=2×90 s at 400 W. Batch 2:O2/N2, 250/50 ml/min. t=6 min. at 400 W.
17. Release chips: Automatic dicing saw.

Four-probe chips

1. Oxide growth: 1500 Å SiO_2, bor drive-in, DRY1150, t=70 min.
2. **Resist adhesion promoter:** HMDS, recipe 4.
3. Spin resist: Track1, PR1_5, AZ5214E.
4. UV-exposure: KS-Aligner, hard contact, t=10 s, mask="new4pp-electrodes".
5. Develop: 70 s in NaOH:H_20 (1:5), rinse in DI water.
6. Metal deposition: Alcatel, Ti/Au 50/2000 Å.
7. Lift-off: Acetone with ultrasound. Rinse with DI water.
8. Cleaning: Plasma asher, O2N2, 240/40, 400 W, T=2 min.
9. Spin coat polyaniline: Manual spinner, 4000 rpm, max. acceleration, t=40 s, Panipol T.
10. Bake: Hotplate, 5 min. at 90°C, 5 min. ramp.
11. Spin coat SU-8 2002: KS-Spinner, 1500 rpm, 500 rpm/s, t=30 s.
12. Wait 30 min. before further processing.
13. UV-exposure: KS-Aligner, hard contact, t=75 s, mask="new4pp-resistor".
14. Bake: Hotplate, 1 hour at 50°C.
15. Develop: PGMEA, 2 min. FIRST, 2 min. FINAL. Rinse with IPA. Air dry.
16. Release chips: Automatic dicing saw.

Appendix E

Thin gold film process recipe

1. Deposition of oxide: 1500 Å SiO_2, bor drive-in, DRY1150, t=70 min.
2. Resist adhesion promoter: HMDS, recipe 4.
3. Spin resist: Track1, PR1_5, AZ5214E.
4. UV-exposure: KS-Aligner, hard contact, t=9 s, mask="new4pp_resistor".
5. Develop: 70 s in NaOH:H_20 (1:5), rinse in DI water.
6. Thin gold film evaporation: Alcatel, Au, rate 1 Å/s.
7. Lift-off: Acetone. Rinse with DI water.
7. Spin resist: Track1, PR1_5, AZ5214E.
8. UV-exposure: KS-Aligner, hard contact, t=9 s, mask="new4pp_electrodes".
9. Develop: 70 s in NaOH:H_20 (1:5), rinse in DI water.
10. Metal deposition: Alcatel, Ti/Au, 50/2000 Å.
11. Lift-off: Acetone in ultrasound. Rinse with DI water.
12. Release chips: Automatic dicing saw.

Appendix F

List of publications

F.1 Published articles

- **M. Lillemose**, M. Spieser, A. Christensen, N. O. Christiansen and A. Boisen. Intrinsically conductive polymer thin film piezoresistors. *Microelectronic Engineering*, 85:969-971, 2008.

- **M. Lillemose**, L. Gammelgaard, J. Richter, E. V. Thomsen and A. Boisen. Epoxy based photoresist/carbon nanoparticle composite. *Composites Science and Technology*, 68:1831-1836, 2008.

- R. Mateiu, **M. Lillemose**, T. S. Hansen, A. Boisen and O. Geschke. Reliability of poly 3,4-ethylenedioxythiophene strain gauge. *Microelectronic Engineering*, 84:1270-1273, 2007.

- M. Nordström, S. Keller, **M. Lillemose**, A. Johansson, S. Dohn, D. Haefliger, G. Blagoi, M. H. Jakobsen and A. Boisen. SU-8 cantilevers for bio/chemical sensing; fabrication, characterisation and development of novel read-out methods. *Sensors*, 8:1595-1612, 2008.

F.2 Conference abstracts

- **M.Lillemose**, L. Gammelgaard, J. Richter, E. V. Thomsen and A. Boisen. Piezoresistive SU-8/nanoparticle composites. *International Workshop on Nanomechanical Sensors.* Copenhagen, Denmark, May 7-10, 2006.

- **M.Lillemose**, L. Gammelgaard, J. Richter, E. V. Thomsen and A. Boisen. Piezoresistive SU-8/carbon nanoparticle composites. *International Conference on Nanoscience and Technology.* Basel, Switzerland, July 30-August 4, 2006.

- **M. Lillemose**, M. Spieser, A. Christensen, N. O. Christiansen and A. Boisen. Intrinsically conductive polymer thin film piezoresistors. *33rd International Conference on Micro- and Nano-Engineering.* Copenhagen, Denmark, September 23-26, 2007.